INSTABILITY-DRIVEN PATTERN TRANSFORMATIONS IN SOFT ARCHITECTED MATERIALS

by

Nitesh Arora

A dissertation submitted in partial fulfillment of
the requirements for the degree of

Doctor of Philosophy

(Mechanical Engineering)

at the

UNIVERSITY OF WISCONSIN–MADISON

2023

Date of final oral examination: 07/27/2023

The dissertation is approved by the following members of the Final Oral Committee:

Stephan Rudykh, Assistant Professor, Mechanical Engineering (chair)
Shiva Rudraraju, Assistant Professor, Mechanical Engineering
Ramathasan Thevamaran, Assistant Professor, Mechanical Engineering
Melih Eriten, Associate Professor, Mechanical Engineering
AJ Boydston, Professor, Department of Chemistry

Dedicated to my parents

ACKNOWLEDGMENTS

First and foremost, I would like to express my sincere gratitude to my advisor Prof. Stephan Rudykh. His enthusiastic guidance and constant support – academic and personal, especially, during the COVID-19 pandemic, in addition to the financial support, made the journey extremely smooth and enjoyable. I would also like to thank my thesis committee members – Prof. Shiva Rudraraju, Prof. Melih Eriten, Prof. Ramathasan Thevamaran, and Prof. AJ Boydston – for serving on my thesis committee and their constant support as teachers.

I am very grateful to Air Force Research Lab team – Dr. Vincent Chen, Dr. Abigail Juhl, and Dr. Philip Buskohl. The collaboration with them greatly shaped my doctoral research. I am also very grateful to Soft Matter Lab members at UW-Madison for their support as colleagues and friends. I would also like to thank Structural and material testing lab manager Jacob Zeuske.

During my Ph.D., I also got the incredible opportunity to visit University of Galway in Ireland, again thanks to my advisor Prof. Stephan Rudykh. I am grateful to the colleagues and friends in Galway, who made my stay in Galway wonderful.

I am also grateful to all my teachers in India. Particularly, my bachelor's thesis advisor Prof. M. M. Joglekar at IIT Roorkee, for his constant guidance. I got introduced to the exciting research area of instabilities in soft materials while working in his lab, which ultimately motivated me to pursue a Ph.D. I am very grateful to my math teacher, Mr. Shubhash Sharma, for always believing in me.

On a personal note, I thank my parents, Ashok Arora and Deepa Arora, for being very caring and responsible parents, and my sister, Amisha Arora. I would also like to thank my roommate, Mukul, and all the friends in Madison, Bhagyashree, Praveen, Mohan, Tej, Prakarsh, Kunal, Debabrata,

Rahul, Subodh, Aaditya, and many more for their affectionate friendship, which greatly helped me glide through the highs and lows of Ph.D. life.

CONTENTS

LIST OF TABLES

LIST OF FIGURES

ABSTRACT

Soft elastomers provide an excellent material platform for developing compliant devices, including soft robots, sensors, and wearable devices, due to their ability to sustain large elastic deformations. However, by designing structured-soft materials, we can extend their capabilities beyond merely a material platform. The structural design, which can be tailored for desired material properties, can involve features such as microscale patterns, hierarchical arrangements, or inclusions within the soft matrix.

When soft architected materials are subjected to large deformations, they often develop elastic (reversible) instabilities. The phenomenon is associated with sudden and dramatic microstructural transformations. Opposed to the traditional approach of designing to curb the onset of instability, this thesis focuses on harnessing instability-induced structural reconfigurations to design stimuli-responsive materials with switchable functionalities. The post-transformation behavior of such tunable materials is dictated by the admissible buckling configurations; therefore, they play a crucial role in the design of these materials.

This thesis provides a detailed study of the instability phenomenon occurring at different length scales in a variety of soft architected materials. First, we show that in 3D fiber composites, the non-linear stiffening behavior of phases dictates the interplay between the long-wave and microscopic instabilities, and defines the wavelength of the buckling patterns. Then, we experimentally illustrate that the fiber composites switch the orientation of their buckling plane, depending on their in-plane periodicity and material properties.

Next, we investigate a composite system consisting of a magnetoactive layer embedded into an inactive elastomeric matrix. With this material system, we show that instability-induced reconfigurations can be triggered via a remotely applied magnetic field. In addition to elucidating the mechanisms

associated with magneto-mechanical instability, the study also outlines the strategy and benefits of harnessing two-field physics for controlling bifurcations in a material system.

We also introduce a novel design framework for achieving desired structural transformations that are encoded magnetically. The framework utilizes the rich interplay of magnetic interactions and instability phenomenon. We showcase the diversity of the admissible reconfigurations through a series of information embedding demonstrations, including alphabet shape matching and Morse code. Finally, by employing this framework, we design a magneto-mechanical metamaterial in which we can program the deformation field to attain local material densification. Furthermore, we demonstrate its application as a strain-tunable vibration absorber.

1 INTRODUCTION

1.1 Elastic instabilities in soft architected materials

The instability development in solids, historically, has been associated with material failure or structural collapse. It can occur across multiple length scales, and through multiple mechanisms, including but not limited to buckling, plastic necking, shear bands, wrinkling, and fracture (Pence and Song, 1991; Nguyen et al., 2019; Li et al., 2023b; Cohen and Durban, 2013; Abu-Qbeitah et al., 2023, 2022; Ansari et al., 2023; Emery and Fu, 2021; Fu et al., 2021; Russ et al., 2020; Shen et al., 2019; Alijani et al., 2021). With the motivation to avoid the onset of instabilities, the study of instability development in solids and structures dates back to the 18^{th} century when Leonard Euler introduced the calculation of the critical load for the buckling of a slender beam in 1759 (Euler, 1759), followed by Lagrange's analysis for higher modes in 1770 (Lagrange, 1770). Since then, a number of studies have made integral contributions to the development of the theory of material and structure stability (Euler, 1780a,b; Kirchhoff, 1859; Love, 1893; Southwell, 1914; Timoshenko and Gere, 2009; Leipholz, 2013; Thompson and Hunt, 1973; Iooss and Joseph, 2012; Geymonat et al., 1993; Nguyen, 2000; Ziegler, 2013; Budiansky, 1974).

This thesis is concerned with the instability development in soft materials. Since, soft materials such as elastomers, gels, and biological tissues can easily sustain large deformations, the instability-induced transformations (for example, buckling, wrinkling, and creasing (Dortdivanlioglu and Linder, 2019; Lin et al., 2016)) do not lead to a catastrophic failure of the material. Instead, they provide the opportunity to leverage the sudden change in the configuration of material morphology for various functionalities. In

nature, instability development can lead to pecuilar structural features, for example, twisting and wavy-patterns in plant organs during differential growth (Huang et al., 2018) and wrinkling of skin when immersed in water, which can improve handling of wet objects (Kareklas et al., 2013; Wilder-Smith, 2004).

The structural reconfigurations induced via instability development have been reported in various flexible architected materials. For example, periodic lattices exhibit mechanical instability by sequential buckling of inner elements (Kang et al., 2014; Frenzel et al., 2016). Circuferential instabilities are observed in radially incompatible bi-tube structure (Emuna and Cohen, 2020). In soft porous architectures, the voids collapse in a cooperative manner leading to an internal reconfiguration of the microstructure (Mullin et al., 2007; Bertoldi et al., 2008). Moreover, multi-phase architected composites (Cho et al., 2016; He et al., 2023; Ongaro et al., 2016b,a; Dehghani et al., 2020) can develop a rich variety of post-buckling patterns (Triantafyllidis and Maker, 1985; Li et al., 2019a; Jiang et al., 2006). Fiber and layered composites develop wavy (or sinusoidal) buckling patterns (Li et al., 2013, 2018a) that may transform into twinning (Li et al., 2022). Soft particulate composites exhibit the formation of ordered anti-symmetric domains in the post-instability regime, in addition to the wavy buckling patterns (Li et al., 2019a).

Moreover, instability-driven pattern transformations provide us with the unique opportunity to build architected materials that can switch their material behavior and morphology. For example, the materials in post-instability regime can show unusual behaviors like the occurence of new elastic wave band gaps (Bertoldi and Boyce, 2008a; Gao et al., 2018; Li et al., 2019b; Rudykh and Boyce, 2014; Bertoldi and Boyce, 2008b), waveguiding capabilities (Shan et al., 2014), auxetic behavior (Bertoldi et al., 2010; Li et al., 2018b; Shim et al., 2013), tunable dielectric permittivity (Goshkoderia et al., 2020a; O'Neill et al., 2022), and photonic switches (Krishnan and

Johnson, 2009), among many others (Bertoldi et al., 2017). Furthermore, the direction-dependent onset of buckling of fibers in a uniform composite has been employed to develop mechanically non-reciprocal materials (Wang et al., 2023). Apparently, in all these material designs, the post-instability behavior of the material is uniquely determined by its buckling characteristics. Hence, widening the range of admissible instability patterns is crucial for building materials with on-demand switchable functionalities.

The soft architected materials with active phases that are responsive to external stimuli, for example, magnetic field, allow us to remotely control the shape-transformations (Yu et al.; Kim et al., 2018; Moreno-Mateos et al., 2023b, 2022a,b; Yarali et al., 2022; Lucarini et al., 2022; Bastola and Hossain, 2021; Zhang et al., 2023; Zhang and Rudykh, 2022; Sim et al., 2023; Wu et al., 2022; Kuang et al., 2021; Montgomery et al., 2021; Alam et al., 2023; Narayanan et al., 2023; Hu et al., 2022; Ciambella et al., 2017, 2018; Ciambella and Tomassetti, 2020; Stanier et al., 2016; Ciambella and Nardinocchi, 2019). Notably, the instability characteristics of these materials, when subjected to a combined loading from multiple physics, presents a novel opportunity to navigate the bifurcation landscape in ways that are inaccessible with only mechanical loading. Rather than solely relying on the mechanical forcing of material to achieve a metastable state, it can be advantageous to use an external stimulus to change the material properties to remotely trigger the instability. Adaptive materials such as dielectric elastomers or magnetorheological elastomers can harness electromechanical or magneto-mechanical coupling to regulate instability (Saxena et al., 2019; Reddy and Saxena, 2018). For example, dielectric elastomers were included in a soft multilayered dielectric stack to determine how electrically-induced finite deformations affect their stability (Bertoldi and Gei, 2011; Rudykh and deBotton, 2011; Rudykh et al., 2014). Magnetic field interactions with ordered arrays of ferrous cylinders have also been shown to induce buckling periodicities of higher order, which are inaccessible with only

mechanical loads (Goshkoderia et al., 2020b). In another instance, a layer of magnetorheological elastomer was placed over a neat elastomer, and the effects of magnetic and mechanical forces on the buckling of the bilayer structure were measured (Danas and Triantafyllidis, 2014; Psarra et al., 2017, 2019).

1.2 Brief overview of the thesis

This thesis encompasses the investigation of instability-driven structural reconfigurations in various types of soft architected materials, including soft fiber composites, magneto-active layered composites, particulate and multi-phase composites with hard-magnetic inclusions.

Chapter 2 focuses on the buckling in 3D fiber composites (FCs). The first part of the chapter elucidates how the strain-stiffening behavior of the matrix and fiber phases influence the instability parameters. The second part concerns with the buckling of fibers in FCs with varying in-plane microstructure periodicity. Through our experiments and simulations, we find that the out-of-plane buckling orientation of fibers is determined by the constituent material properties, volume fractions, and the in-plane periodicity.

Chapter 3 presents a numerical and experimental study on the buckling behavior of the composite system consisting of a magnetoactive layer embedded into an inactive elastomeric matrix. The composite is subjected to compressive strains in the presence of a high magnetic field. The results demostrates that the instability development can be tailored remotely by the applied magnetic field.

Chapter 4 introduces a new class of transformable materials with magnetic defect-defined switchable configurations. The soft material can be magnetically-programmed to transform into various encoded patterns utilizing the rich interplay of magnetic interactions and instability phenomenon.

The strategy allows us to break the limit of admissible configurations of the instability-induced patterns that dictate the post-transformation behavior. We experimentally realize the phenomenon in a material system consisting of periodically distributed magnetic inclusions in a soft matrix. We also showcase the idea of reconfigurable material design by embedding binary information in magnetic form, which can be read out through the unique repositioning of inclusions via the applied mechanical deformation.

Chapter 5 presents a magneto-mechanical metamaterial that offers tunable frequency filtering. The metamaterial can be programmed with a non-uniform deformation field to locally control the material-densification. The strategy harnesses instability development in a graded architected design and the magnetic interactions between the inclusions. Through our simulations, we show that the metmaterial is bistable and new bandgaps are inducted via applied deformation. Moreover, we uncover the underlying physical mechanisms leading to the transformation in the acoustic behavior of the metamaterial.

Finally, Chapter 6 concludes the thesis with a brief discussion on the new findings and results.

1.3 General theoretical background

Consider the position vector of a material point in the current configuration of body $\mathfrak{B}$ is $\mathbf{x}$, and $\mathbf{X}$ in reference configuration $\mathfrak{B}_0$. The displacement function for every material point in the body is characterized by $\mathbf{x} = \mathbf{x}(\mathbf{X})$. Then, the deformation gradient is defined as $\mathbf{F} = \partial\mathbf{x}/\partial\mathbf{X},\ \mathrm{J} \equiv \det\mathbf{F} > 0$.

The differential operators in the reference configuration are denoted Div($\bullet$) and Curl($\bullet$) and the corresponding operators in the current configuration are div($\bullet$) and curl($\bullet$), respectively. In this thesis, I consider quasi-static deformation (unless stated otherwise) in the absence of an electric field, electric charges, or electrical currents within the material.

Consequently, the magnetic induction $\mathbf{B}$ and magnetic intensity $\mathbf{H}$ (in the current configuration) satisfy the following field equations

$$\mathrm{div}\mathbf{B} = 0 \quad \text{and} \quad \mathrm{curl}\mathbf{H} = \mathbf{0}. \tag{1.1}$$

In the Lagrangian form, (1.1) can be written as (Dorfmann and Ogden, 2004)

$$\mathrm{Div}\mathbf{B}^0 = 0 \quad \text{and} \quad \mathrm{Curl}\mathbf{H}^0 = \mathbf{0}, \tag{1.2}$$

where the Div and Curl operators are defined with respect to $\mathbf{X}$, $\mathbf{B}^0 = J\mathbf{F}^{-1}\mathbf{B}$ and $\mathbf{H}^0 = \mathbf{F}^T\mathbf{H}$ are the Lagrangian counterparts of the magnetic fields. Moreover, in a heterogeneous body, magnetic fields satisfy the jump conditions across the interface

$$[\![\mathbf{B}]\!] \cdot \mathbf{N} = 0 \quad \text{and} \quad [\![\mathbf{H}]\!] \times \mathbf{N} = \mathbf{0}, \tag{1.3}$$

or alternatively,

$$\left[\left[\mathbf{B}^0\right]\right] \cdot \mathbf{N}^0 = 0 \quad \text{and} \quad \left[\left[\mathbf{H}^0\right]\right] \times \mathbf{N}^0 = \mathbf{0}, \tag{1.4}$$

where $\mathbf{N}$ and $\mathbf{N}^0$ denote the normal to the interface in the deformed and reference configurations, respectively. The jump operator $[\![\bullet]\!] \equiv (\bullet)^+ - (\bullet)^-$ is defined such that $\mathbf{N}$ and $\mathbf{N}^0$ are pointing towards phase $(\bullet)^-$. The magnetization is customarily defined as

$$\mathbf{M} = \frac{\mathbf{B}}{\mu_0} - \mathbf{H}, \tag{1.5}$$

where μ_0 is the vacuum magnetic permeability.

Following the works of Brown (1966); Coleman and Noll (1974); Kovetz (2000), the magnetization is constitutively defined in terms of free-energy function $\psi(\mathbf{F}, \mathbf{B})$ as

$$\mathbf{M} = -\rho\frac{\partial\psi}{\partial\mathbf{B}}, \tag{1.6}$$

where ρ is the material density in the current configuration. The *total* Cauchy stress $\boldsymbol{\sigma}$ is given by

$$\boldsymbol{\sigma} = \rho \frac{\partial \psi}{\partial \mathbf{F}} \mathbf{F}^T - \frac{1}{2\mu_0}(\mathbf{B} \cdot \mathbf{B})\mathbf{I} + \mathbf{H} \otimes \mathbf{B} + (\mathbf{M} \cdot \mathbf{B})\mathbf{I}. \tag{1.7}$$

In terms of these relations, the energy-density function ψ fully characterizes the behavior of magneto-active elastomers. Note that in the absence of material (or vacuum), the stress tensor (1.7) is still non-zero and depends on the magnetic field. The corresponding stress tensor is also referred to as Maxwell stress. The free energy in Lagrangian form is defined as $\Psi(\mathbf{F}, \mathbf{B}^0) = \psi(\mathbf{F}, J^{-1}\mathbf{F}\mathbf{B}^0)$. In terms of Ψ, a Lagrangian *amended* energy function can be constructed as (Dorfmann and Ogden, 2004)

$$W(\mathbf{F}, \mathbf{B}^0) = \rho_0 \Psi(\mathbf{F}, \mathbf{B}^0) + \frac{\mathbf{F}\mathbf{B}^0 \cdot \mathbf{F}\mathbf{B}^0}{2\mu_0 J}, \tag{1.8}$$

where $\rho_0 = \rho J$ is the material density in the reference configuration. Then, the corresponding Lagrangian variables are given by

$$\mathbf{H}^0 = \frac{\partial W}{\partial \mathbf{B}^0} \quad \text{and} \quad \mathbf{P} = \frac{\partial W}{\partial \mathbf{F}} \tag{1.9}$$

where $\mathbf{P}$ is the 1^{st} Piola Kirchhoff stress tensor. Eqs. (1.7)–(1.9) hold true for compressible hyperelastic materials. For incompressible materials ($J = 1$), however, the total Cauchy stress tensor is

$$\boldsymbol{\sigma} = \frac{\partial W}{\partial \mathbf{F}} \mathbf{F}^T - p\mathbf{I}, \tag{1.10}$$

where p is the Lagrange multiplier associated with the incompressibility constraint.

In the absence of body forces, the total Cauchy and 1^{st} Piola-Kirchhoff

stress tensors satisfy the equilibrium conditions

$$\mathrm{div}\boldsymbol{\sigma} = \mathbf{0} \quad \text{and} \quad \mathrm{Div}\mathbf{P} = \mathbf{0}. \tag{1.11}$$

The corresponding jump conditions at the interface are

$$[\![\boldsymbol{\sigma}]\!] \cdot \mathbf{N} = 0 \quad \text{and} \quad [\![\mathbf{P}]\!] \cdot \mathbf{N}^0 = 0. \tag{1.12}$$

Note that for magnetically-inactive hyperelastic materials, Eq. (1.8) reduces to

$$W(\mathbf{F}) = \rho_0 \Psi(\mathbf{F}). \tag{1.13}$$

2 BUCKLING IN SOFT FIBER COMPOSITES

2.1 Introduction

Soft fiber composites (FCs) simultaneously possess many desirable mechanical properties including flexibility, strength, toughness, rigidity, and fatigue resistance (Zhang et al., 2021a; Wang et al., 2019; Xiang et al., 2020a; Li et al., 2020), therefore, are ubiquitously present in natural and bio-materials (Saheb and Jog, 1999; Humphrey, 2002). Their mechanical behavior can be significantly tailored by modifying the microstructure comprising of soft and stiff phases. The performance of soft FCs can be further enhanced by leveraging the pattern transformations associated with the buckling instability. Historically, the buckling of fibers was considered as a failure mode and, therefore, was to be predicted and avoided (Rosen, 1965; Christensen, 1979). Recently, however, elastic instability phenomenon has been embraced to design tunable materials that can undergo sudden and dramatic microstructural transformations (Mullin et al., 2007; Florijn et al., 2016; Kochmann and Bertoldi, 2017; Babaee et al., 2016; Li et al., 2022). Furthermore, the recent advancements in the multi-material 3D printing (Zhou et al., 2020; Schwartz and Boydston, 2019; Xiang et al., 2020b; Kuang et al., 2019) have allowed to experimentally realize instability phenomenon in soft composites (Slesarenko and Rudykh, 2016; Li et al., 2019a).

In FCs, the instabilities can be classified into macroscopic (or long-wave) and microscopic based on the wavelength of the buckling pattern. Macroscopic instability is characterized by the critical wavelength significantly larger than the characteristic microstructure, whereas microscopic instability leads to the formation of a new periodicity of the order of the initial microstructure. To predict the onset of instabilities, the linearized incremental analysis for small displacement superimposed on finite deformations is widely used (Ogden, 1997). The macroscopic instability can be

estimated by performing the loss of ellipticity analysis on the effective tensor of elastic moduli (Volokh, 2017), which can be calculated by employing micromechanics (Agoras et al., 2009; Rudykh and deBotton, 2012; Slesarenko et al., 2017b; Fontenele et al., 2022; Aboudi and Volokh, 2020; Aboudi and Gilat, 2023), phenomenological (Merodio and Ogden, 2002; Merodio and Pence, 2001), or numerical-based approaches (Bruno et al., 2010; Greco and Luciano, 2011; Greco et al., 2020). The microscopic instability can be predicted by employing the Bloch-Floquet analysis superimposed on finite deformations (Triantafyllidis and Maker, 1985; Nestorovic and Triantafyllidis, 2004; Triantafyllidis et al., 2006). Moreover, the loss of ellipticity analysis is equivalent to the microscopic instability analysis in the long-wave limit (Geymonat et al., 1993).

The instability development in FCs, primarily, is dictated by the stiffness contrast between the phases and their volume fractions (Agoras et al., 2009; Rudykh and deBotton, 2012; Merodio and Ogden, 2002; Merodio and Pence, 2001; Qiu and Pence, 1997; Bruno et al., 2010; Greco and Luciano, 2011; Greco et al., 2020; Michel et al., 2010; Triantafyllidis and Maker, 1985; Nestorovic and Triantafyllidis, 2004; Triantafyllidis et al., 2006; Slesarenko and Rudykh, 2017). However, in the majority of previous studies, a weakly non-linear hyperelastic neo-Hookean material model is used to define the constitutive behavior of phases. This relatively simple model corresponds to the class of the models with Gaussian statistics of the polymer molecular chain, and it cannot fully capture the rich and complex behavior of soft materials (Xiang et al., 2020d,b; Flory and Rehner Jr, 1943; Wang and Guth, 1952; Treloar, 1943).

To address this issue, in the first part of the chapter, Sec. 2.2, we focus on the influence of the stiffening effects – stemming from the non-Gaussian statistics of the polymer chains – on the microscopic and long-wave instabilities in 3D FCs. In particular, we examine the hyperelastic 3D fiber composites with the phases characterized by the Gent model (Gent, 1996)

and study the interplay between the microscopic and long-wave instabilities. To this end, we derive the analytical expression for the onset of long-wave instabilities, and employ the Bloch-Floquet analysis superimposed on finite deformations to detect microscopic instabilities and associated buckling modes in the 3D FCs.

In the second part of the chapter, Sec. 2.3, we focus on the influence of in-plane periodic microstructure on the instability development in 3D soft FCs. In this regard, Slesarenko and Rudykh (2017) employed the Bloch-Floquet analysis to examine the instabilities and associated buckling patterns in periodic 3D FCs with the square arrangement of fibers. Recently, Galich et al. (2018) numerically studied the instabilities and propagation of waves in FCs with the rectangular arrangement of fibers. By analyzing the polarization of eigenmodes in the vicinity of microscopic instability, they predicted that the orientation of the buckling plane in these composites can be switched by tuning the periodic unit cell's aspect ratio. Followed by this, Li et al. (2018a) experimentally realized the buckling behavior, however, only identifying a single buckling direction. In particular, they observed that the fibers always buckle in the direction they are closer to each other. Here, we find the configurations of FCs exhibiting change in the orientation of buckling plane, and also identify the factors influencing the behavior. As we shall show, in addition to the aspect ratio, the fiber volume fraction and the shear modulus contrast between the phases also significantly affect the direction of fiber buckling. Guided by the simulation results, we realize the instability-induced pattern formations and the rotation of buckling plane in the experiments.

2.2 Fiber composites with stiffening phases*

Consider the 3D fiber composite made of aligned fibers embedded in the soft matrix (as shown in Fig. 2.1) with fiber volume fraction $c^{(f)}$ and matrix volume fraction $c^{(m)} = 1 - c^{(f)}$. Here and thereafter, in this section, the parameters and fields corresponding to fibers and matrix are denoted by the superscripts $(\bullet)^{(f)}$ and $(\bullet)^{(m)}$, respectively. To capture the non-linear stiffening effects, here we consider the 3D-fiber composites with the fiber and matrix phases characterized by the Gent material model. The corresponding SEDF is

$$\psi_G = -\frac{1}{2}\mu J_m \ln\left(1 - \frac{I_1 - 3}{J_m}\right), \tag{2.1}$$

where μ is the initial shear modulus, J_m is the locking parameter. $I_1 = \mathrm{Tr}(\mathbf{C})$ is the first invariant of the right Cauchy-Green deformation tensor, $\mathbf{C} = \mathbf{F}^\top\mathbf{F}$. The lock-up occurs as the deformation approaches the certain level defined as $(I_1 - 3) \to J_m$. In the limit $J_m \to \infty$, Gent model (2.1) reduces to the neo-Hookean model.

For further use, we define the average properties as $\bar{(\bullet)}$, which are defined as

$$\bar{(\bullet)} = \frac{1}{V}\int_{\mathfrak{B}_0} (\bullet(\mathbf{X}))dV \tag{2.2}$$

In this work, we examine the instabilities in 3D-fiber composites, in which the 3D buckling mode is dictated by the amount of deformation in the fiber direction. Therefore, we consider the uniaxial deformation along the fiber direction; the corresponding macroscopic deformation gradient is

$$\bar{\mathbf{F}} = \lambda^{-1/2}(\mathbf{e_1} \otimes \mathbf{e_1} + \mathbf{e}_2 \otimes \mathbf{e}_2) + \lambda \mathbf{e}_3 \otimes \mathbf{e}_3. \tag{2.3}$$

*This section is adapted from the article N. Arora, J. Li, V. Slesarenko, and S. Rudykh, Microscopic and long-wave instabilities in 3D fiber composites with non-Gaussian hyperelastic phases. International Journal of Engineering Science 157, 103408 (2020).

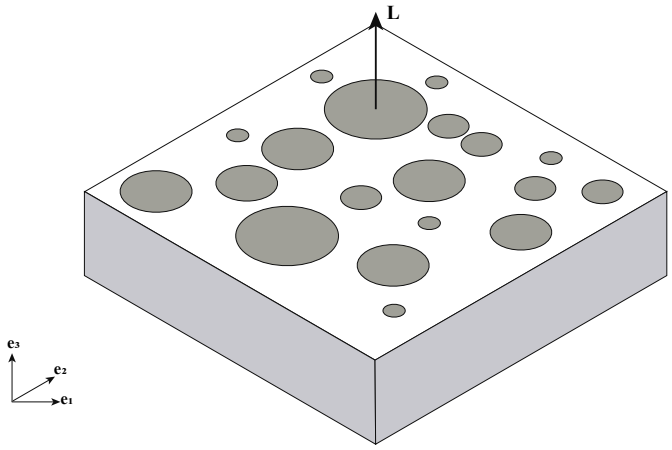

Figure 2.1: Schematic of FC with random distribution of fibers, aligned along the direction **L**.

2.2.1 Macroscopic instability analysis

2.2.1.1 Background

To perform the instability analysis, we consider incremental deformations superimposed on a finitely deformed state. Following Ogden (1997), we define the incremental deformation gradient as $\dot{\mathbf{F}} = \partial \mathbf{u}/\partial \mathbf{X}$, where $\mathbf{u}$ is the incremental displacement. Accordingly, the increment in the 1^{st} Piola-Kirchhoff stress tensor $\dot{\mathbf{P}}$ can be expressed as

$$\dot{\mathbf{P}} = \mathbb{A}\dot{\mathbf{F}}, \tag{2.4}$$

where

$$\mathbb{A} = \frac{\partial^2 \psi}{\partial \mathbf{F} \partial \mathbf{F}}. \tag{2.5}$$

is the tensor of elastic moduli. The incremental equilibrium equation can be written as

$$A_{i\alpha j\beta} \frac{\partial^2 u_j}{\partial X_\alpha \partial X_\beta} = 0. \tag{2.6}$$

In the case of incompressible materials, Eq. (2.6) modifies to

$$A_{i\alpha j\beta}\frac{\partial^2 u_j}{\partial X_\alpha \partial X_\beta} + \frac{\partial \dot{p}}{\partial X_i} = 0, \tag{2.7}$$

where $\dot{p}$ is the variation in p. The incompressibility condition implies

$$\nabla \cdot \mathbf{u} = 0. \tag{2.8}$$

The incremental equilibrium Eq. (2.7) in the current configuration can be written as

$$A^0_{ipjq}\frac{\partial^2 u_j}{\partial x_p \partial x_q} + \frac{\partial \dot{p}}{\partial x_i} = 0, \tag{2.9}$$

where

$$A^0_{ipjq} = J^{-1}F_{p\alpha}F_{q\beta}A_{i\alpha j\beta}. \tag{2.10}$$

The macroscopic instability can be estimated by performing the loss of ellipticity analysis on the effective tensor of elastic moduli. In particular, we seek a solution for Eq. (2.9) in the form

$$\mathbf{u} = \hat{\mathbf{m}}e^{ik\mathbf{x}\cdot\hat{\mathbf{n}}}, \qquad \dot{p} = qe^{ik\mathbf{x}\cdot\hat{\mathbf{n}}}, \tag{2.11}$$

where $\hat{\mathbf{m}}$ and $\hat{\mathbf{n}}$ are unit vectors and k denotes a wave number. The incompressibility constraint (2.8) results in the requirement

$$\hat{\mathbf{m}} \cdot \hat{\mathbf{n}} = 0. \tag{2.12}$$

Substitution of (2.11) in (2.9) yields

$$\mathbf{Q}\hat{\mathbf{m}} + iq\hat{\mathbf{n}} = \mathbf{0}, \tag{2.13}$$

where $\mathbf{Q}$ is the so-called acoustic tensor defined as

$$Q_{ij} \equiv A^0_{ipjq}\hat{n}_p\hat{n}_q. \tag{2.14}$$

The associated strong ellipticity condition is

$$Q_{ij}\hat{m}_i\hat{m}_j \equiv A^0_{ipjq}\hat{n}_p\hat{n}_q\hat{m}_i\hat{m}_j > 0. \tag{2.15}$$

2.2.1.2 Effective tensor of elastic moduli

We propose the following effective SEDF for the uniaxially loaded TI 3D-FCs with incompressible Gent phases

$$\tilde{\psi}^{(TI)} = -\frac{1}{2}\left[c^{(m)}\mu^{(m)}J_m^{(m)}\ln\left(1-\frac{\tilde{I}_1^{(m)}-3}{J_m^{(m)}}\right) + c^{(f)}\mu^{(f)}J_m^{(f)}\ln\left(1-\frac{\tilde{I}_1^{(f)}-3}{J_m^{(f)}}\right)\right], \tag{2.16}$$

where,

$$\tilde{I}_1^{(f)} = \bar{I}_4 + 2\bar{I}_4^{-1/2} + \left(1-c^{(m)}\omega\right)^2\left(\bar{I}_1 - \bar{I}_4 - 2\bar{I}_4^{-1/2}\right), \tag{2.17}$$

and

$$\tilde{I}_1^{(m)} = \bar{I}_4 + 2\bar{I}_4^{-1/2} + \left[\left(1+c^{(f)}\omega\right)^2 + c^{(f)}\omega^2\right]\left(\bar{I}_1 - \bar{I}_4 - 2\bar{I}_4^{-1/2}\right), \tag{2.18}$$

with $\bar{I}_4 = \mathbf{L}\cdot\bar{\mathbf{C}}\mathbf{L}$ and $\bar{\mathbf{C}} = \bar{\mathbf{F}}^T\bar{\mathbf{F}}$; $\mathbf{L}$ is a unit vector along the direction of fibers (see Fig. 2.1). The scalar parameter ω is

$$\omega = \frac{G^{(f)} - G^{(m)}}{G^{(f)}\left(1-c^{(f)}\right) + G^{(m)}\left(1+c^{(f)}\right)}, \tag{2.19}$$

where $G^{(r)}$ denotes the (r)-phase tangent shear modulus, defined as

$$G^{(r)} = J_m^{(r)}\mu^{(r)}/\theta^{(r)}, \tag{2.20}$$

with $\theta^{(r)} = J_m^{(r)} - (\lambda^2 + 2\lambda^{-1} - 3)$. The tangent shear modulus $G^{(r)}$ reduces to the initial shear modulus $\mu^{(r)}$ in the case of the neo-Hookean phase ($J_m^{(r)} \to \infty$). Note that the proposed SEDF has a remarkably compact form,

and it is applicable for the relevant fully 3D uniaxial deformation, and it is not limited to the plane-strain constraint (Rudykh and deBotton, 2012), which leads to a bulky expression for ω.

The non-zero components of the tensor of elastic moduli corresponding to the SEDF (2.16) are

$$\begin{aligned}
&\hat{A}^0_{1111} = \hat{A}^0_{2222} = \tilde{G}\lambda^{-1} + 2\beta\lambda^{-2},\\
&\hat{A}^0_{3333} = \lambda^2\left[\bar{G}(1+2\lambda^{-3}) - 2\tilde{G}\lambda^{-3} + 2\lambda^2\left(\beta + 2\zeta(1-\lambda^{-3}) + \eta(1-\lambda^{-3})^2\right)\right],\\
&\hat{A}^0_{1122} = \hat{A}^0_{2211} = 2\beta\lambda^{-2},\\
&\hat{A}^0_{1133} = \hat{A}^0_{2233} = \hat{A}^0_{3311} = \hat{A}^0_{3322} = 2\lambda\left[\beta + \zeta(1-\lambda^{-3})\right],\\
&\hat{A}^0_{1212} = \hat{A}^0_{2121} = \hat{A}^0_{3131} = \hat{A}^0_{3232} = \tilde{G}\lambda^{-1},\\
&\hat{A}^0_{1313} = \hat{A}^0_{2323} = \lambda^2\left(\tilde{G} + \left(\bar{G} - \tilde{G}\right)(1-\lambda^{-3})\right),
\end{aligned} \tag{2.21}$$

where

$$\begin{aligned}
\beta &= c^{(m)}G^{(m)}(\tilde{\alpha}^{(m)})^2/\theta^{(m)} + c^{(f)}G^{(f)}(\tilde{\alpha}^{(f)})^2/\theta^{(f)},\\
\zeta &= c^{(m)}G^{(m)}\tilde{\alpha}^{(m)}(1-\tilde{\alpha}^{(m)})/\theta^{(m)} + c^{(f)}G^{(f)}\tilde{\alpha}^{(f)}(1-\tilde{\alpha}^{(f)})/\theta^{(f)},\\
\eta &= c^{(m)}G^{(m)}(1-\tilde{\alpha}^{(m)})^2/\theta^{(m)} + c^{(f)}G^{(f)}(1-\tilde{\alpha}^{(f)})^2/\theta^{(f)},
\end{aligned} \tag{2.22}$$

with

$$\tilde{\alpha}^{(f)} = \left(1 - c^{(m)}\omega\right)^2 \quad \text{and} \quad \tilde{\alpha}^{(m)} = \left(1 + c^{(f)}\omega\right)^2 + c^{(f)}\omega^2. \tag{2.23}$$

The effective moduli $\tilde{G}$ and $\bar{G}$ are

$$\tilde{G} = G^{(m)}\frac{\left(1+c^{(f)}\right)G^{(f)} + \left(1-c^{(f)}\right)G^{(m)}}{\left(1-c^{(f)}\right)G^{(f)} + \left(1+c^{(f)}\right)G^{(m)}} \quad \text{and} \quad \bar{G} = c^{(f)}G^{(f)} + c^{(m)}G^{(m)}. \tag{2.24}$$

2.2.1.3 Analytical estimate

By using the strong ellipcticity condition (2.15) on the effective elastic modulus $\hat{A}^0_{ijkl}$, the onset of macroscopic instability occurs when the stretch

in the fiber directions exceeds the critical level given by

$$\lambda_{cr} = \left(1 - \frac{\tilde{G}}{\bar{\bar{G}}}\right)^{1/3}. \tag{2.25}$$

Consider a special case of the FCs with fibers and matrix phases characterized by identical locking parameters, namely, $J_m^{(f)} = J_m^{(f)} = J_m$. Remarkably, for this case, Eq. (2.25) reduces to

$$\lambda_{cr} = \left(1 - \frac{\tilde{\mu}}{\bar{\mu}}\right)^{1/3}, \tag{2.26}$$

where the effective initial shear moduli are

$$\tilde{\mu} = \mu^{(m)} \frac{\left(1 + c^{(f)}\right)\mu^{(f)} + \left(1 - c^{(f)}\right)\mu^{(m)}}{\left(1 - c^{(f)}\right)\mu^{(f)} + \left(1 + c^{(f)}\right)\mu^{(m)}}, \tag{2.27}$$

and

$$\bar{\mu} = c^{(f)}\mu^{(f)} + c^{(m)}\mu^{(m)}. \tag{2.28}$$

Thus, the onset of macroscopic instability and the corresponding critical stretch are independent of the locking parameters J_m for TI composites with identical stiffening characteristics of the Gent phases. Note that the expression for the critical stretch (2.26) coincides with the one corresponding to neo-Hookean TI composites (Rudykh and deBotton, 2012).

2.2.2 Microscopic instability analysis

To study microscopic instability, we employ the Bloch-Floquet technique, superimposed on finite deformations (Bertoldi et al., 2008; Geymonat et al., 1993; Triantafyllidis et al., 2006; Slesarenko and Rudykh, 2017). Here, we consider FCs with fiber aligned in the direction $\mathbf{L} = \mathbf{e}_3$, and in-plane periodicity ($\mathbf{e}_1$, $\mathbf{e}_2$). The instability analysis is performed on the representative volume element (RVE) of the square periodic unit cell (shown in Fig. 2.2).

The initial dimensions of the RVE are $L = W = a$ and $h = 0.05a$. In the undeformed configuration, d is the initial diameter of the fiber and a is the distance between two adjacent fibers in either of $\mathbf{e}_1$ or $\mathbf{e}_2$ direction (see Fig. 2.2) and $c^{(f)} = \pi d^2/4a^2$.

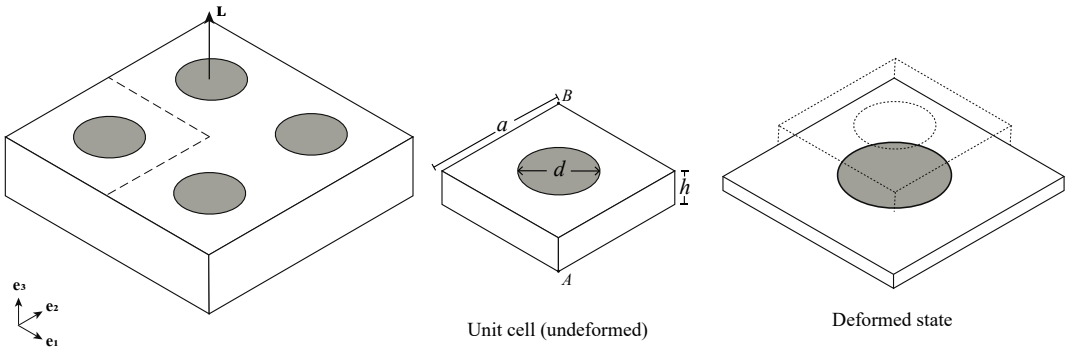

Figure 2.2: 3D periodic fiber composite with $\mathbf{L}$ in the direction of fiber.

Numerical simulations are conducted by the means of finite element code COMSOL Multiphysics 5.4. The instability analysis is performed in two steps: First, we finitely deformation by imposing periodic boundary conditions on the faces of the unit cell. Second, Bloch-Floquet conditions are imposed on the unit cell as $\mathbf{u}(\mathbf{X} + \mathbf{R}) = \mathbf{u}(\mathbf{X}) \exp(-i\mathbf{K} \cdot \mathbf{R})$, where $\mathbf{K}$ is the Bloch wave vector, and $\mathbf{R}$ defines the spatial periodicity in the reference configuration. The eigenvalue problem is solved until a non-trivial zero eigenvalue is detected. The corresponding deformation level and the wavenumber are identified as the critical deformation level and critical wavenumber k_{cr}.

2.2.3 Results

Figure 2.3 illustrates the dependence of critical stretch and the associated wavelengths (inverse of critical wavenumber) on the fiber locking parameter ($J_m^{(f)}$) (a) and matrix locking parameter ($J_m^{(m)}$) (b). The results are shown

for the fiber composites with fiber volume fraction = 0.048, shear modulus contrast, $\kappa = \mu^{(f)}/\mu^{(m)} = 100$, and $J_m^{(m)} = 0.1$ for subfigure (a) and $J_m^{(f)} = 1$ for subfigure (b). The filled and hollow symbols correspond to macroscopic and microscopic instabilities, respectively. The half-filled symbol marks the point corresponding to the transition of instability mode. We observe that the stability of the composites increases (critical stretch decreases) with an increase in the fiber locking parameter and/or decrease in the matrix locking parameter. Moreover, the critical wavelength corresponding to the microscopic instabilities increases with a decrease in the fiber locking parameter and/or with an increase in the matrix locking parameter. As a consequence, the composites with stiffening fibers tend to develop long-wave instabilities, whereas the composites with stiffening matrix phase are more prone to microscopic instabilities.

Figure 2.4 represent the buckling mode of fibers, which develop as a result of microscopic instabilities in the composites with various phase locking parameters. In particular, the locking parameters are: $J_m^{(f)} = 0.4$ and $J_m^{(m)} = 0.1$ (a); $J_m^{(f)} = 2$ and $J_m^{(m)} = 0.1$ (b); $J_m^{(f)} = 1$ and $J_m^{(m)} = 0.1$ (c); and $J_m^{(f)} = 100$ and $J_m^{(m)} = 0.1$ (d). The height of all the buckling modes is identical. It is evident from these buckling modes, that even a small variation in the locking parameters of phases results in significant changes in the shape of these patterns.

Finally, we summarize the results for Gent-Gent composites in Fig. 2.5 showing the critical stretch ratio (a) and normalized critical wavenumber (b) as surface-functions of fiber and matrix locking parameters. The results are given for FCs with $\kappa = 100$ and $c^{(f)} = 0.048$. The dashed curve separates the white region where either of the phases locks-up before the onset of instabilities (no instabilities are detected). In particular, the composites with significantly smaller matrix locking parameters $J_m^{(m)}$ get stable beyond the corresponding lock-up stretch ratio λ_{lock}. The dash-dotted curve divides the remaining region into two domains corresponding to microscopic and

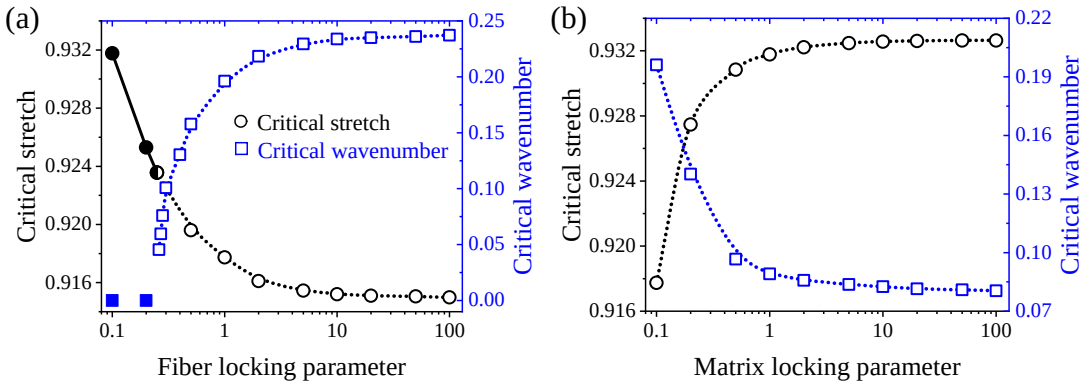

Figure 2.3: Dependence of critical stretch and normalized critical wavenumber on the fiber (a) and matrix (b) locking parameters.

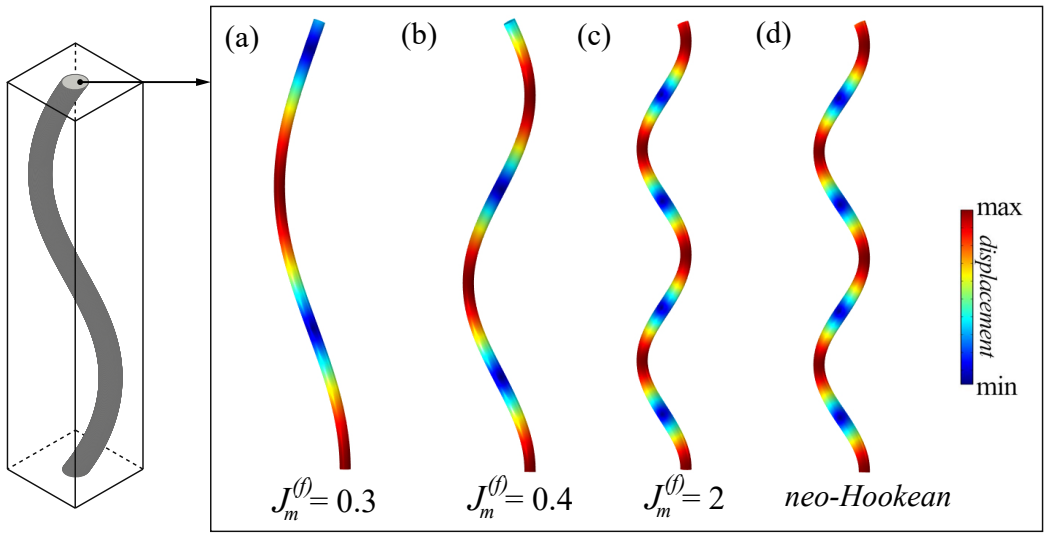

Figure 2.4: Buckling modes of fibers for composites with various phase locking parameters. The color shows the magnitude of in-plane displacement.

long-wave instabilities. In agreement with our previous observations, the results show that the critical stretch and wavenumber vary significantly in the regions of small locking parameters (either of fiber or matrix phases). The

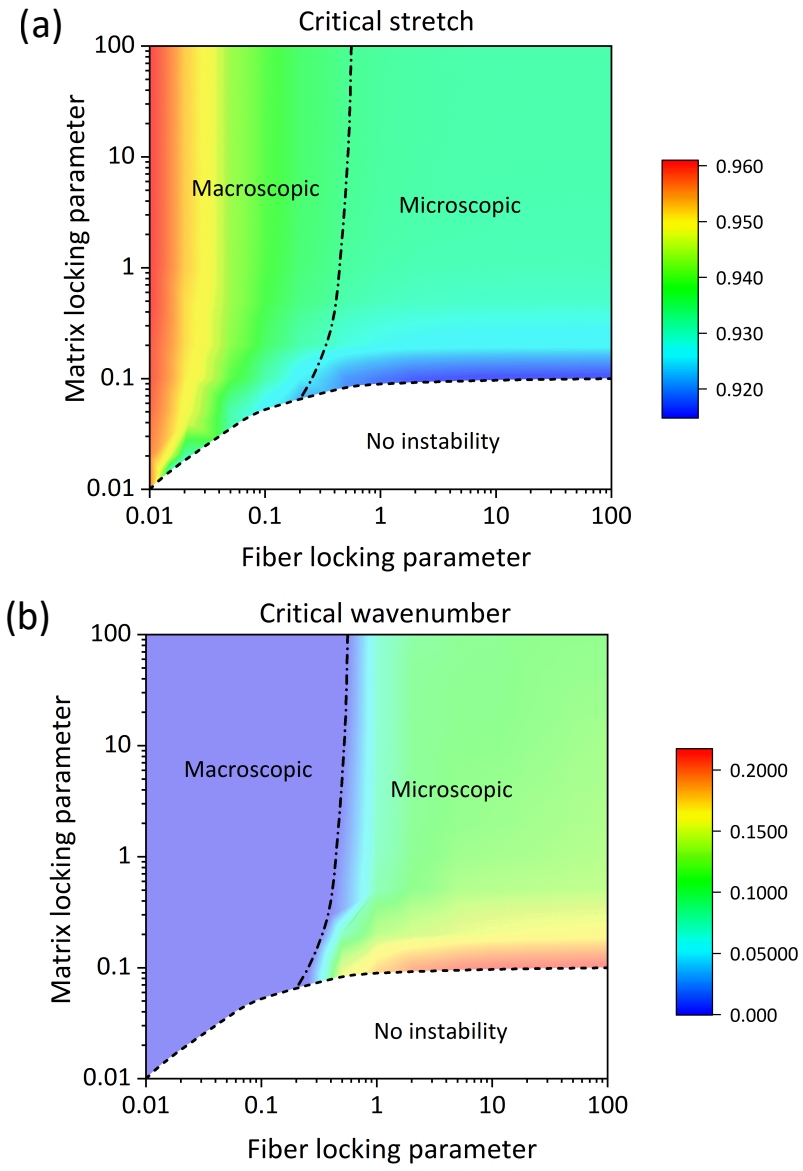

Figure 2.5: Critical stretch λ_{cr} (top) and normalized critical wavenumber, $k_3^{cr}a$ (bottom), with various fiber locking parameters $J_m^{(f)}$ and matrix locking parameters $J_m^{(m)}$. FCs with fiber volume fraction $c^{(f)} = 0.048$ and shear modulus contrast $\kappa = 100$ are considered.

wavenumber, however, also shows a significant tunability in the transition zone from long-wave to microscopic instabilities. Clearly, the stability of FCs increases (critical stretch decreases) as the fiber locking parameter $J_m^{(f)}$ increases and/or the matrix locking parameter $J_m^{(m)}$ decreases. Moreover, the critical wavelength corresponding to the microscopic instabilities increases with a decrease in the fiber locking parameter and/or with an increase in the matrix locking parameter. The FCs with lower $J_m^{(f)}$ tend to develop long-wave instabilities, whereas smaller values of $J_m^{(m)}$ favor the development of microscopic instabilities. However, in the region where both locking parameters are small, composites exhibit macroscopic instabilities.

2.3 Fiber composites with rectangular in-plane periodicity[†]

In this section, we study the buckling of soft 3D-fiber composites (FCs) with varying in-plane microstructure periodicity. In particular, FCs with rectangular in-plane arrangement of fibers are considered, i.e., the fibers are periodically situated at distance a from each other in one principal direction and distance b along the other principal direction ($b > a$), as shown in Fig. 2.6.

2.3.1 Material fabrication and experiments

First, we provide the details of specimen fabrication, experimental device and setup. The 3D fiber composites are printed using the Stratasys Objet260 Connex 3D printer. Circular fibers are vertically aligned along the direction $\mathbf{e}_2$ and are periodically distributed in transparent soft matrix with the separation of distance a along the $\mathbf{e}_1$ direction, and b along the $\mathbf{e}_3$ direction,

[†]This section is adapted from the article N. Arora, J. Li, and S. Rudykh, Tunable buckling configurations via in-plane periodicity in soft 3D-fiber composites: Simulations and experiments. International Journal of Solids and Structures 250, 111711 (2022).

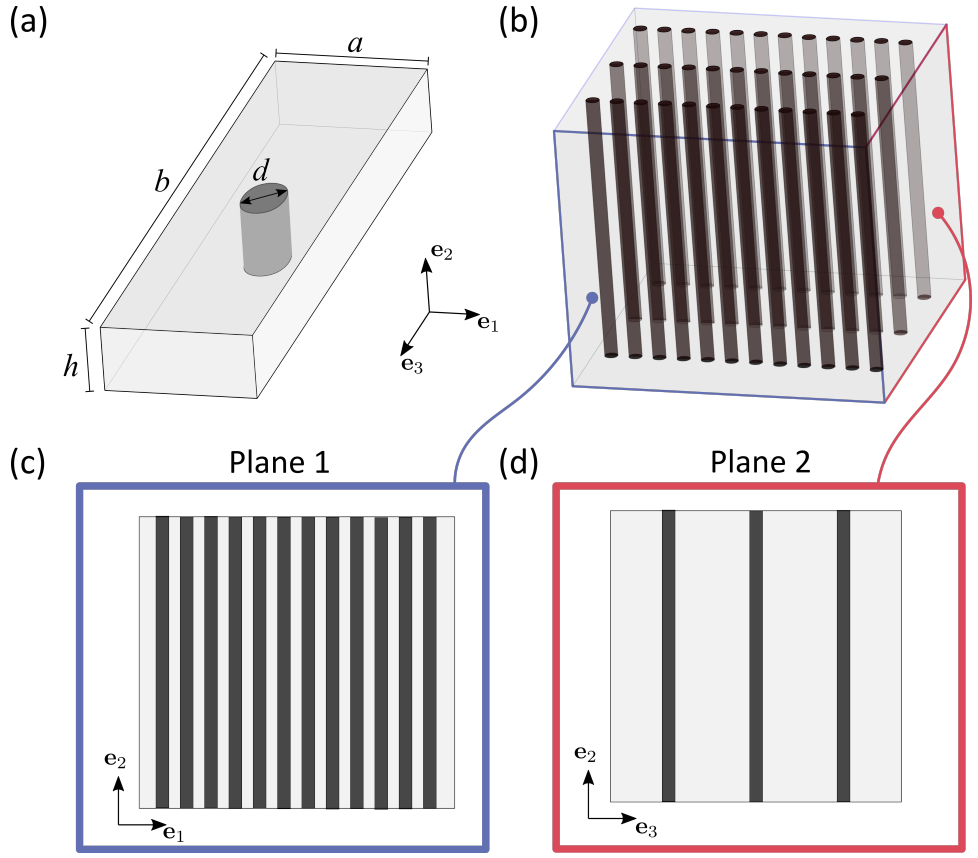

Figure 2.6: (a) Unit cell of fiber composite with rectangular arrangement of circular fibers. (b) 3D schematic of the fiber composite highlighting the distinct fiber arrangement in two principal planes – (c) $\langle \mathbf{e}_1, \mathbf{e}_2 \rangle$ plane referred to as *Plane 1* and (d) $\langle \mathbf{e}_3, \mathbf{e}_2 \rangle$ plane referred to as *Plane 2*.

Table 2.1: Geometric parameters, number of fibers along the principal directions, and dimensions of the printed fiber composites.

v_f	b/a	a (mm)	Number of fibers in $\mathbf{e}_1$-direction	Number of fibers in $\mathbf{e}_3$-direction	Specimen height (mm)
0.05	4	4	20	6	74
0.05	7	2.5	20	3	60
0.05	10	2.5	24	3	60
0.06	10	2.5	12	2	40

as per the dimensions of unit cell (Fig. 2.6a); note that $b > a$. The schematic of an example specimen is shown in Fig. 2.6b. The stiff fibers are printed using the digital material (mixture of TangoPlus and VeroBlack) DM-95 (shear modulus, $\mu_f \approx 4.9$ MPa (Meng et al., 2020)), while transparent soft matrix is printed using TangoPlus ($\mu_m \approx 0.21$ MPa (Slesarenko et al., 2017a; Slesarenko and Rudykh, 2018)). Here, and thereafter, the fields and parameters corresponding to fibers and matrix are denoted as $(\bullet)_f$ and $(\bullet)_m$, respectively. Geometrically, the FCs are defined by the aspect ratio of unit cell, b/a, and the volume fraction of fiber phase, $v_f = \pi d^2/(4ab)$, where d is the diameter of each fiber (Fig. 2.6a). We print four different FCs with the geometric parameters, number of fibers, and dimensions provided in Table 2.1. To reduce the influence of boundary effects on the periodic FCs, the specimens are printed with an additional TangoPlus material layer of thickness 5 mm on the boundary. Uniaxial compression tests are performed using MTS Sintech 10/GL testing machine (maximum load 50 kN). The specimens are compressed quasi-statically along the direction of fibers, $\mathbf{e}_2$, at the strain rate of 10^{-3} s^{-1}. Since the soft matrix's materials is transparent, the embedded fibers and their buckling patterns are visible from the outside. The deformation of FCs is recorded using two high resolution cameras: The first camera is facing towards the $\langle \mathbf{e}_1, \mathbf{e}_2 \rangle$ plane referred to as *Plane 1* (Fig. 2.6c) and the second camera captures the deformation in plane $\langle \mathbf{e}_3, \mathbf{e}_2 \rangle$ or *Plane 2* (Fig. 2.6d).

2.3.2 Numerical modeling

In this section, we discuss the numerical analysis performed to predict the onset of instability and the associated buckling modes in FCs with rectangular arrangement of fibers. We employ Bloch-Floquet analysis superimposed on finite deformations to investigate the microscopic instability, similar to the study for fiber composites with stiffening phases (subsection 2.2.2). We performed the analysis on the representative volume element (RVE) of the periodic FC with dimensions as shown in Fig. 2.6a; the height of the RVE is $h = 0.05a$. The FC is subjected to the uniaxial deformation along the fibers defined by the following macroscopic deformation gradient:

$$\bar{\mathbf{F}} = \lambda \mathbf{e}_2 \otimes \mathbf{e}_2 + \lambda^{-1/2} \left(\mathbf{e}_1 \otimes \mathbf{e}_1 + \mathbf{e}_3 \otimes \mathbf{e}_3 \right), \tag{2.29}$$

where λ is the applied macroscopic stretch along the direction of fibers and $\mathbf{e}_i$ are basis vectors as shown in Fig. 2.6.

Fibers and matrix are defined by the neo-Hookean strain energy density function, which is integrated in COMSOL as

$$\Psi = \frac{1}{2}\mu \left(I_1 - 3 \right) - \mu \ln J + \frac{1}{2}\Lambda \left(\ln J \right)^2, \tag{2.30}$$

where μ is the shear modulus and Λ is the first Lame's parameter. To model the nearly-incompressible behavior of both phases, we set a very high ratio between the first Lame's parameter and shear modulus, $\Lambda/\mu = 1000$. The microscopic instability analysis is performed in two steps, as described in subsection 2.2.2.

2.3.3 Results and discussion

We start by investigating the effect of the in-plane periodicity aspect ratio, b/a, on the instability parameters and the orientation of buckling plane in the FCs. Figures 2.7a and b show the critical stretch λ_{cr} and normalized

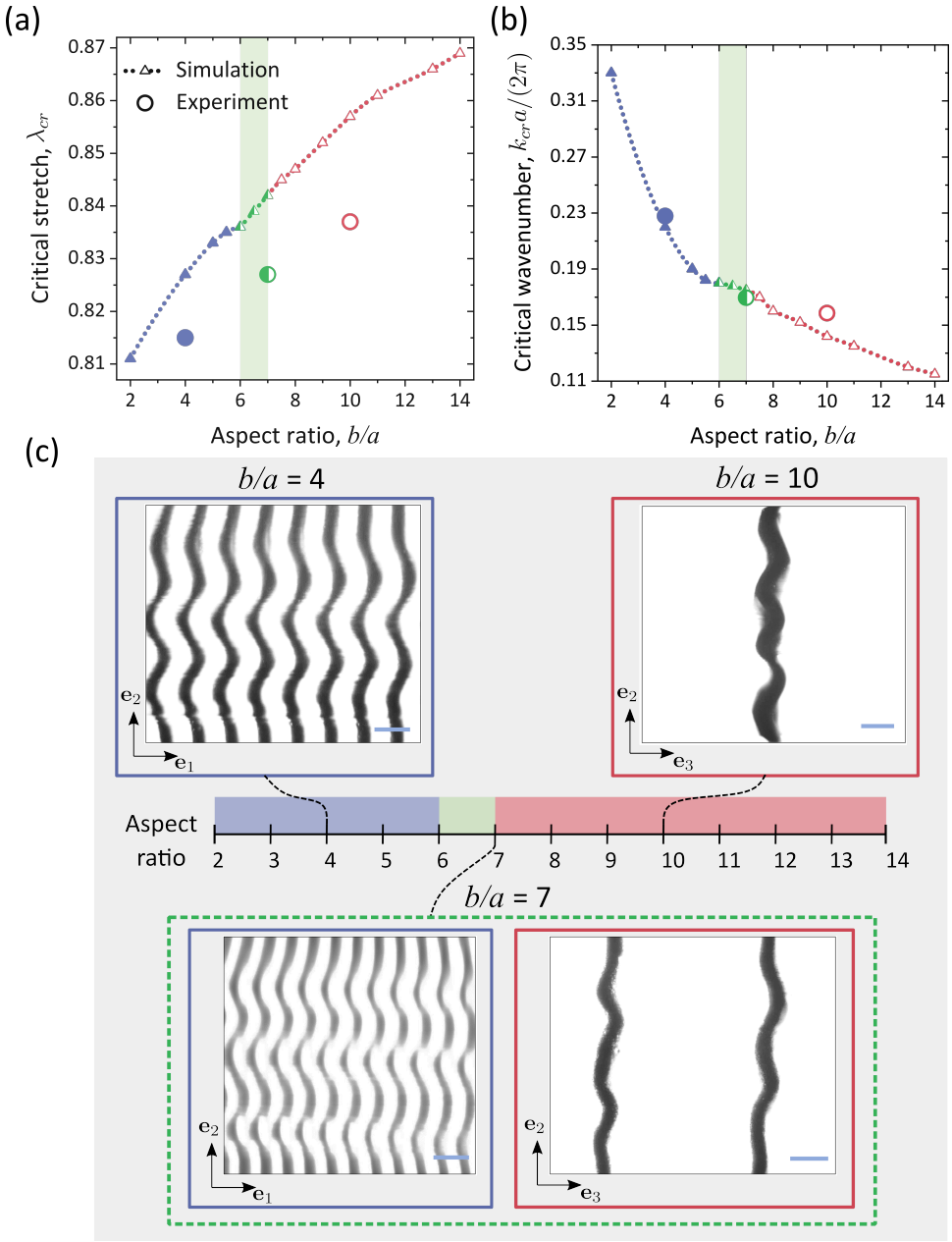

Figure 2.7: (a) Critical stretch λ_{cr} and (b) normalized critical wavenumber $k_{cr}a/(2\pi)$ versus the aspect ratio of fiber composite, b/a. Fiber composites with fiber volume fraction $v_f = 0.05$ and shear modulus contrast $\mu_f/\mu_m = 23$ are considered. (c) Experimental images of instability induced pattern formations in fiber composites with aspect ratios, $b/a = 4$, $b/a = 7$, and $b/a = 10$ at $\lambda = 0.654$, $\lambda = 0.687$, and $\lambda = 0.615$, respectively. The color coded horizontal line shows the orientation of buckling plane: blue and red correspond to principal planes *Plane 1* and *Plane 2*, respectively, and green represents the non-principal plane. Scale bar: 5 mm.

critical wavenumber $k_{cr}a/(2\pi)$ as the functions of b/a, respectively. The results are presented for the composites with fiber volume fraction $v_f = 0.05$, $\mu_f \approx 4.9$ MPa, and $\mu_m \approx 0.21$ MPa, such that the shear modulus contrast is $\mu_f/\mu_m \approx 23$. The triangles with dotted curves represent the simulation results, and the circular symbols denote the experimental findings. The experimental value of critical wavenumber in the reference configuration is evaluated using the buckling wavelength l in the current configuration. The relation between them is $k_{cr} = 2\pi\lambda/l$, where stretch ratio λ corresponds to the deformation level at which the wavelength is measured. Blue filled symbols mark the composites in which the fibers buckle in the principal *Plane 1*, whereas red hollow symbols show buckling in principal *Plane 2*. The green half-filled symbols and the estimated region marked in the green color denote the buckling of fibers in a non-principal plane. Figure 2.7c shows the images of instability patterns observed experimentally: $b/a = 4$ (top left), $b/a = 10$ (top right), and $b/a = 7$ (bottom). The horizontal bar is shaded in color to show the orientation of buckling at a given b/a value: blue for *Plane 1*, red represents *Plane 2*, and the green region denotes buckling in a non-principal plane.

We observe that the FCs develop instability at smaller deformation levels (λ_{cr} increases) with an increase in the periodicity aspect ratio, b/a. Moreover, the wavelength of instability patterns (inverse of k_{cr}) increases as the periodicity aspect ratio increases. The values of the numerically predicted critical wavenumber values are in a good agreement with the experimental results. In experiments, however, the instability develops at higher deformation levels than predicted by simulations. The discrepancy observed here can be attributed to multiple factors, such as, for example, boundary effects or the stabilization effect due to the interphasial zone between the fibers and matrix (Arora et al., 2019). Nevertheless, the variation of critical parameters with aspect ratio follow the same trend in simulations and experiments.

Interestingly, the buckling plane of the FC rotates with a change in its aspect ratio. In particular, we observe that at smaller values of b/a, the fibers buckle in the direction in which they are closer to each other, i.e., in *Plane 1*. For instance, at $b/a = 4$, we find in our simulations and experiments, that the fibers undergo cooperative buckling in $\langle \mathbf{e}_1, \mathbf{e}_2 \rangle$ principal plane (Fig. 2.7c–top left). On the other hand, at higher values of b/a, *Plane 2* is preferred over the first one for buckling. For example, in the FCs with $b/a = 10$, the buckling is observed in the principal plane $\langle \mathbf{e}_3, \mathbf{e}_2 \rangle$ (Fig. 2.7c–top right).

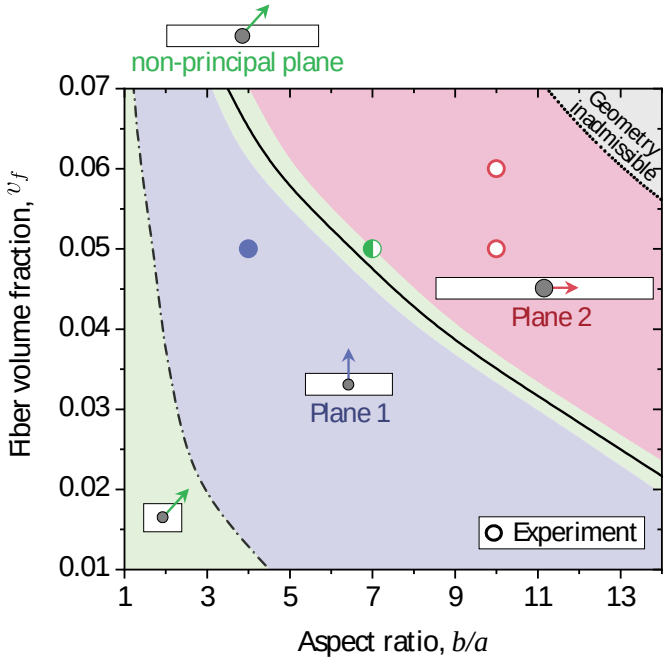

Figure 2.8: Buckling plane map as the function of fiber volume fraction v_f and aspect ratio b/a. Fiber composites with shear modulus contrast $\mu_f/\mu_m = 23$ are considered. The circular symbols denote the experimental findings.

Note that the orientation of the buckling plane does not discretely switch from *Plane 1* to *Plane 2*. Instead, there exists a transition region (shaded in green color) where the fibers buckle in a non-principal plane. In simulations,

this region can be identified by observing the polarization of the associated eigenmode(s) in the following two ways: (i) if the eigenmode for which the zero non-trivial eigenfrequency is obtained has a polarization along the non-principal direction, or (ii) for the eigenmodes with polarization in the principal directions ($\mathbf{e}_1$ and $\mathbf{e}_3$), if the eigenvalues become (non-trivially) zero at almost same deformation levels. For the FCs considered here, the transition region approximately lies in the range $6 \lesssim b/a \lesssim 7$. In experiments, for the composite with aspect ratio $b/a = 7$, the instability patterns are observed in both *Plane 1* and *Plane 2* (Fig. 2.7c–bottom), which indicates that the buckling occurs in a non-principal plane. This is in contrast to experimental results for the FCs with $b/a = 4$ and $b/a = 10$: for these composites the buckling is only observed in a single principal plane.

Next, we investigate the role of fiber composite microstructure geometry on the buckling plane orientation. To this end, Fig. 2.8 shows the buckling plane map as the function of geometric parameters: fiber volume fraction v_f and aspect ratio b/a, for the composites with $\mu_f/\mu_m = 23$. The regions are color shaded according to the buckling plane orientations, similar to Fig. 2.7. The arrows in the schematic of respective regions show the direction of fiber buckling. The dotted curve separates the gray region that is geometrically inadmissible, given by the equation, $v_f \geq \pi a/(4b)$. The circular symbols represent the experimental results.

It is evident from Fig. 2.8 that the FCs can be classified into four geometric parameter groups, based on their buckling plane orientations. First, in the composites with small aspect ratios, i.e. with nearly square arrangement of fibers, the buckling plane orientates towards the non-principal direction (denoted by the green shaded region). These composites are not influenced by the unequal distribution of fibers along the two principal directions and their instability behavior is close to that of the square periodic FCs. With increase in the aspect ratio, however, the buckling plane switches to *Plane 1*. This transition, approximately marked by the dash-dotted

curve, occurs at comparatively higher values of b/a for the composites with smaller fiber volume fractions. For instance, in the FC with $b/a = 2$, the fibers buckle along the non-principal direction when $v_f = 0.03$, and along $\mathbf{e}_1$-direction for $v_f = 0.05$.

In the composites that show the effects of unequal in-plane distribution of fibers, we observe that the volume fraction of fibers has a similar influence as that of periodicity aspect ratio on the buckling plane orientation. Specifically, in the FCs with smaller fiber volume fractions and smaller aspect ratios, the fibers are more likely to buckle along the direction in which they are closer to each other (or *Plane 1*). In contrast, the buckling along the second principal plane is preferred at higher values of v_f and b/a. The switch in buckling plane orientation may be attributed to the decrease in the the distance between the periphery of fibers with an increase in v_f and/or b/a: This leads to a significantly higher reinforcement along the $\mathbf{e}_1$-direction in comparison to the $\mathbf{e}_3$-direction and the FCs tend to behave as laminates with layers periodically distributed along $\mathbf{e}_3$-direction. Hence, $\langle \mathbf{e}_3, \mathbf{e}_2 \rangle$ plane (or *Plane 2*) becomes energetically favorable for the instability development. These two regions (shaded in red and blue) are separated by a transition region in the middle (shaded in green color). In this region, similar to the nearly square periodic FCs, the fibers buckle in neither *Plane 1* nor *Plane 2*, instead buckle in a non-principal plane. The black solid curve in Fig. 2.8 is approximately drawn at the centre of the transition region; it is termed as the *transition curve*.

The experimental results for FCs with $v_f = 0.05$ having aspect ratios $b/a = 4$, $b/a = 7$, and $b/a = 10$ are in good agreement with the simulations (as was also previously shown in Fig. 2.7). Moreover, the fibers in FC with $v_f = 0.06$ and $b/a = 10$ are experimentally observed to buckle in *Plane 2* (hollow red symbol), further validating the numerical predictions.

Finally, we examine the dependence of fiber buckling orientation on the shear modulus contrast between the phases. In Fig. 2.9, we plot the transition

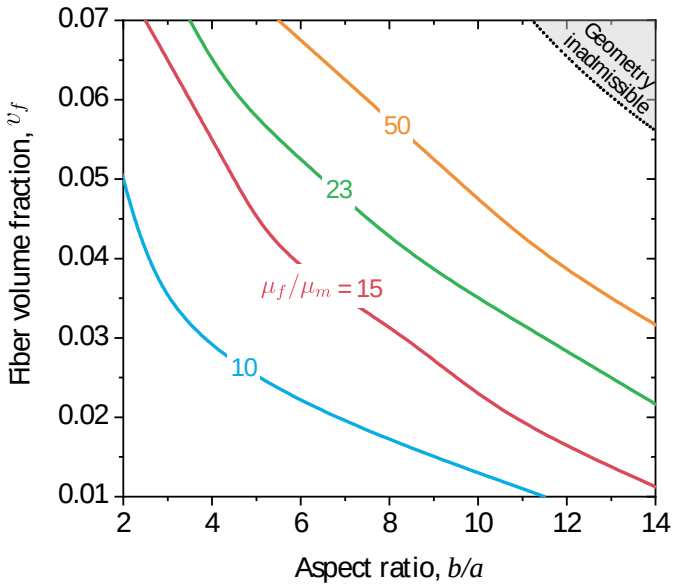

Figure 2.9: Shift in transition curve with the variation in shear modulus contrast μ_f/μ_m of fiber composite.

curves, which correspond to the transition region between *Plane 1* and *Plane 2* on the buckling plane map (see the black solid curve in Fig. 2.8). We consider the FCs with shear modulus contrast: $\mu_f/\mu_m = 10$ (blue), $\mu_f/\mu_m = 15$ (red), $\mu_f/\mu_m = 23$ (green), and $\mu_f/\mu_m = 50$ (orange). We observe that with an increase in the shear modulus contrast (μ_f/μ_m), the transition curve shifts towards the higher periodicity aspect ratios and higher fiber volume fractions. For instance, consider the FCs with geometric parameters $v_f = 0.03$ and $b/a = 8$, they develop buckling in *Plane 2* for $\mu_f/\mu_m = 10$, whereas fibers buckle in *Plane 1* when the shear modulus contrast is increased to $\mu_f/\mu_m = 50$. Recall that the area between the transition curve and the dotted curve (separating the geometrical inadmissible region) correspond to the FCs that develop buckling in *Plane 2*. Therefore, as the transition curve shifts with an increase in the shear modulus contrast, FCs are more likely to develop buckling in the first principal plane for a wide range of geometric

parameters. Hence, higher values of μ_f/μ_m favors the buckling of fibers in *Plane 1*.

The results presented here can be utilized in designing systems that exploits the targeted buckling plane; for instance, an acoustic metamaterial that can filter waves based on their polarization. Moreover, these controlled microstructure transformations in FCs can be merged with other material systems at different length scales to build hierarchical elastic metamaterials (Hussein, 2019; Bacquet et al., 2018; Arora et al., 2022; Ostoja-Starzewski et al., 2016). The dynamic properties of such systems can be studied by applying the recently developed adaptive isogeometric methods (Yu et al., 2022; Jansari et al., 2022; Chen et al., 2022, 2020). Furthermore, we note that the onset of instabilities can be affected by the uncertainties or imperfections in the material or geometry of the composite. The effect of such uncertainties can be quantified and integrated into the numerical framework through stochastic analysis (Ding et al., 2020, 2021; Hauseux et al., 2017, 2018).

3 TUNING INSTABILITY DEVELOPMENT IN MAGNETORHEOLOGICAL ELASTOMER LAMINATES*

3.1 Introduction

Instability tuning with combined loading from multiple physics presents a novel opportunity to navigate the bifurcation landscape in ways that are inaccessible with only mechanical loading. Rather than solely relying on the mechanical forcing of material to achieve a metastable state, it can be advantageous to use an external stimulus to change the material properties to remotely trigger the instability. Adaptive materials such as dielectric elastomers or magnetorheological elastomers can harness electromechanical (Xia et al., 2021) or magneto-mechanical coupling to regulate instability. For example, dielectric elastomers were included in a soft multilayered dielectric stack to determine how electrically-induced finite deformations affect their stability (Bertoldi and Gei, 2011; Rudykh and deBotton, 2011; Rudykh et al., 2014). Magnetic field interactions with ordered arrays of ferrous cylinders have also been shown to induce buckling periodicities of higher order, which are inaccessible with only mechanical loads (Goshkoderia et al., 2020b). In another instance, a layer of magnetorheological elastomer was placed over a neat elastomer, and the effects of magnetic and mechanical forces on the buckling of the bilayer structure were measured (Danas and Triantafyllidis, 2014). This work strives to determine if buckling instability can be induced in a laminated magnetorheological elastomer via an applied magnetic field to provide a quick remotely-triggered geometric reconfiguration.

Magnetorheological elastomers (MREs) are fabricated by crosslinking

*This chapter is adapted from the article V. Chen, N. Arora et al., Mechanical instability tuning of a magnetorheological elastomer composite laminate. Composites Part B 251, 110472 (2023). NA developed the computational model for the instability analysis and analyzed the data. VC performed the experiments. All contributed to the writing of the manuscript.

micron-scale magnetic particles within an elastomeric matrix. The magnetic particles can be isotropically dispersed throughout the matrix, or a magnetic field can be applied to the sample (during polymerization) so that aligned columns of magnetic particles are formed. In either system, it has been consistently shown that the shear stiffness of an MRE increases fast and reversibly with an applied magnetic field, as reported in the double lap shear tests (Nam et al., 2020), magnetorheology (Walter et al., 2017), and dynamic mechanical analysis (Chen et al., 2007). In addition, anisotropically loaded MREs show a stronger stiffening effect over isotropic MREs in the aligned direction (Khanouki et al., 2019). In general, the storage and loss modulus of an MRE depend on the: (i) magnetic field-induced particle interactions (ii) the viscoelasticity of the matrix, and (iii) the adhesion of the particles to the matrix (Morillas and de Vicente, 2020). However, the experimental literature lacks a consensus on the effect of magnetic field on the MRE damping behavior as described by Li and Sun (2014), with some articles claiming an increase, decrease, or unclear change in loss factor with an applied magnetic field. A recent comprehensive review of magneto-mechanical characterization of MREs by Bastola and Hossain (2020) provides additional context on these challenges.

The complexity of the MRE response to combined mechanical and magnetic fields is exacerbated in mechanical instability studies, where small changes in stiffness, geometric, and perturbation forces influence a critical buckling event. Coupled magneto-mechanical material modeling has provided a useful lens to interpret MRE behavior (Garcia-Gonzalez and Hossain, 2020; Saxena et al., 2013; Tiersten, 1964; Gorodkin et al., 2009; Keip and Rambausek, 2017; Javili et al., 2013; Castañeda and Galipeau, 2011; Kadapa and Hossain, 2022; Ivaneyko et al., 2014; Itskov and Khiêm, 2016; Ciambella et al., 2018; Ortigosa and Gil, 2016; Moreno-Mateos et al., 2023a), with a particular focus on instability effects in the literature. In 1968, Moon and Pao (1968) pioneered a model to determine the critical buckling point of a

magnetoelastic thin plate constrained in a transversely- applied magnetic field, and their results were compared to experiments. Later, Kankanala and Triantafyllidis (2008) developed a continuum mechanics formulation that described the instability formation of an MRE rectangular block subjected to plane-strain deformation and a transversely applied magnetic field. Otténio et al. (2008) derived the coupled linearized (or incremental) equations superimposed on large deformations (building on the formulation by Dorfmann and Ogden (2004)) to analyze the surface instabilities in a magnetoactive half-space. Psarra et al. (2017, 2019) determined the effect of a magnetic field on a surface layer of MRE adhered to a soft elastomer layer, and validated their work with experimental studies. Rudykh and Bertoldi (2013) analyzed the effect of anisotropic magnetic particle formation within MREs and derived the long-wave estimates for the magneto-mechanical instabilities in magnetorheological laminates. Recently, Pathak et al. (2022) analytically predicted the existence of unusual microscopic modes in layered MREs under the action of a magnetic field. These studies help build a foundation to understand magnetoelastic coupling in MRE materials; however, more experimental research is needed to identify magnetic tuning features for magneto-mechanical applications.

Thanks to their simple, remote, and reversible principle of operation, MREs can provide the material platform for various applications, such as variable-stiffness devices (Erb et al., 2012; Ginder et al., 2002), tunable vibration absorbers (Ginder et al., 2001; Wang et al., 2018), damping devices (Gong et al., 2012; Yang et al., 2012), sensors (Lanotte et al., 2003; Tian et al., 2011), noise barriers (Farshad and Le Roux, 2004; Karami Mohammadi et al., 2019), remotely controlled actuators (Ciambella et al., 2017; Kim et al., 2018; Stanier et al., 2016; Tang et al., 2018), biomedicine (Makarova et al., 2016), and soft robotics (Hu et al., 2018; Yim and Sitti, 2011) among many others. In this study, we investigate the capacity of a magnetic field to tune the wrinkling instability in the MRE stiff/soft composite laminate, with

an eye toward how this can impact practical applications. We perform the experimental investigation of the buckling development in the MRE laminate under mechanical and magnetic loading sweeps. Further, a large deformation nonlinear magneto-mechanical computational model is implemented using the experimentally derived constitutive parameters and magnetization profile. The study concludes with a tuning diagram of how to exploit the levers of mechanical loading and magnetic field to control the wrinkling response of an MRE architecture.

3.2 Experiments

3.2.1 Fabrication of MRE Specimens

To generate the neat soft elastomeric matrix, Sylgard 184 (Ellsworth Adhesives, Germantown, WI) base and catalyst were mixed rigorously with a handheld mixer for 5 minutes, followed by vacuum degassing for 1 hour at room temperature. The base-to-catalyst ratio was varied from 10:1 to 30:1 to tune the crosslink density and stiffness of the elastomer. The degassed mixture was poured into 3D printed molds (Flashforge Creator Pro, ABS filament) with dimensions of 20 mm $\times$ 7 mm $\times$ 7 mm and cured at 60°C for 2 hours.

To fabricate the magnetoelastomer composite, iron powder with a 3 µm average diameter (US Research Nanomaterials Inc., Houston, TX, US) was mixed into the Sylgard 184 at volume fractions from 0-0.52. Iron particles were dispersed in the Sylgard 184 base prior to the addition of the catalyst. A planetary mixer (Thinky, ARE-310) rotating at 1000 RPM for 2 minutes produced a homogeneous mixture without causing a significant rise in temperature (¡ 5°C), which may lead to premature curing. The mixture was placed under a vacuum for 1 hour to remove air pockets introduced by the mixing. The iron-loaded composite was molded by casting between two

acrylic sheets (McMaster Carr, Aurora, OH) with acrylic spacers (Astra Products, Copiague, NY) ranging from 0.2-0.5 mm thick cut by a CO2 laser (Full Spectrum Laser, PS48-150W). The layer was cured at 60°C for 2 hours. After curing, the specimen was laser cut to rectangles of 28 $\times$ 7 mm^2 using a 1064 nm laser cutter (Keyence, MD-X1520).

The laminate specimen was formed by layering rectangles of neat elastomer (30:1 base-to-catalyst ratio, 20 mm $\times$ 7 mm) followed by magnetoelastomer (28 mm $\times$ 7 mm), and then another layer of neat elastomer (20 mm $\times$ 7 mm). A thin layer (¡100 μm) of the pre-polymerized 30:1 Sylgard 184 was applied between the layers as a chemically compatible adhesive. The assembly was secured in a 3D printed mold during 2 hours of curing at 60°C, followed by 2 hours of curing at 100°C. A representative laminate sample can be seen in Fig. 3.1c.

3.2.2 MRE Laminate Test Setup

Figure 3.1a shows the experimental setup that allows simultaneous axial compression and a transverse magnetic field to be applied to an MRE laminate. The electromagnet coils can generate a uniform 2T magnetic field in the volume occupied by the laminate MRE sample. A non-magnetic compression stage was 3D printed (Fig. 3.1b), allowing for a plunger (activated by a servo-motor) to compress the laminate architecture while under an applied magnetic field. The laminate sample is constrained within the compression stage by an acrylic plate with silicone oil applied between the sample and the acrylic plate to allow for a slip at the interface. The MRE laminate long axis is oriented along the vertical mechanical loading direction (z-axis), and the magnetic field is applied horizontally (y-axis) across the laminated layers. A representative image of the MRE laminate specimen, with dimensions annotated, is shown in Fig 3.1c. All specimens had a nominal initial height (h_0) of 20 mm, a depth (d) of 7 mm, and a width (w) of 7 mm. The MRE layer consisted of an iron particle loading of 0.29 and

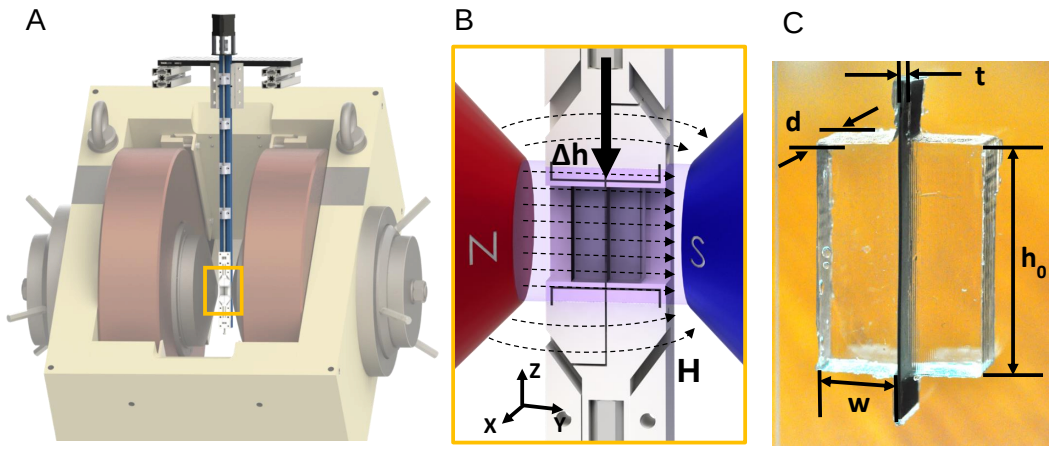

Figure 3.1: Experimental setup of combined axial compression under transverse magnetic field. A) Image of MRE laminate buckling setup and the GWM 3474-140 electromagnet coils with a custom servo-driven mechanical compression stage. B) Image of MRE specimen in the compression stage with applied displacement (z axis) and magnetic field (y axis) orientations annotated. Highlighted region indicates the uniform magnetic field zone. C) Representative image of MRE laminate specimen with annotated dimensions. The MRE layer extends outside of the specimen to provide a tab for clamping in the compression grips. h_0 = 20 mm, d= 7 mm, w = 7 mm, t = 0.2-0.5 mm.

included 10 distinct MRE layer thicknesses, ranging from t = 250 – 618 μm. The MRE layer extends beyond the non-active layers (28 mm vs. 20 mm) to enable clamping by the compression stage, which reduces the twisting of the MRE layer under an applied magnetic field. The shared siloxane base chemistry between the neat and MRE-loaded layers resulted in a strong bonding. Attempts to pull the layers apart resulted in tearing in the soft/ neat layer only. No delamination was observed upon repeated loading and unloading of the sample (¿ 10 cycles) in the compression jig.

Compression and image capture with a digital camera (Nikon, D750) were synchronized with an Arduino UNO. Systematic compression of 50 μm/step was applied to the specimen from the resting state. The camera was set at

a safe distance from the electromagnet, and a 100 mm macro lens (Tokina, AT-X PRO Macro 100) in conjunction with a 2× teleconverter (Nikon, TC-201) were used to capture digital images. The onset of wrinkling is difficult to visually detect in experimental systems. To mitigate inconsistency in visual detection, an image processing workflow was developed to improve and standardize the detection of wrinkling across specimens. Image captures of the MRE laminate under varying degrees of compression were collected (24.3 microns/pixel). Thresholding was applied to convert the colorized images into binary data tables, where positive pixels correspond to the MRE layer, and negative pixels correspond to the neat/soft matrix. The effective width of the MRE layer was determined by the number of columns exhibiting positive pixels. Registration marks embedded in the plungers were used to measure the height of the specimen under compression to determine the compressive strain. A critical buckling point (λ_c) was defined as the intersection between two linear fits of the data prior to buckling (low slope) and after buckling (rapid rise in width). A built-in fitting function (Piecewise PWL2) in OriginPro was used to process the data.

3.2.3 Characterization of MRE Magnetic and Mechanical Properties

The MRE formulation and mixing protocol in this study was selected to produce an isotropic magneto-responsive material with a homogeneously dispersed mixture of spherical iron particles. The amount of iron particle loading controls the magnetization capacity of the MRE, as well as the overall stiffness, as the rigid fillers increase the mechanical properties of the MRE. To characterize this dependence, the magnetization (M [A/m]), magnetic susceptibility (χ), and Young's Modulus (E [MPa]) of the MRE composite were measured as a function of increasing iron volume fraction loadings (see Fig. 3.2). The volume fraction, ϕ , of the iron particles in the

MRE is defined as,

$$\phi = \frac{m_{Fe}/\rho_{Fe}}{m_{Fe}/\rho_{Fe} + m_{PDMS}/\rho_{PDMS}}, \tag{3.1}$$

where m_x and ρ_x correspond to the mass and density, respectively of the iron carbonyl particles (Fe) and the neat 10:1 base:catalyst Sylgard 184 (PDMS). The densities for the iron carbonyl particles and the neat silicone were taken as 7.87 g/cm^3 and 1.05 g/cm^3, respectively.

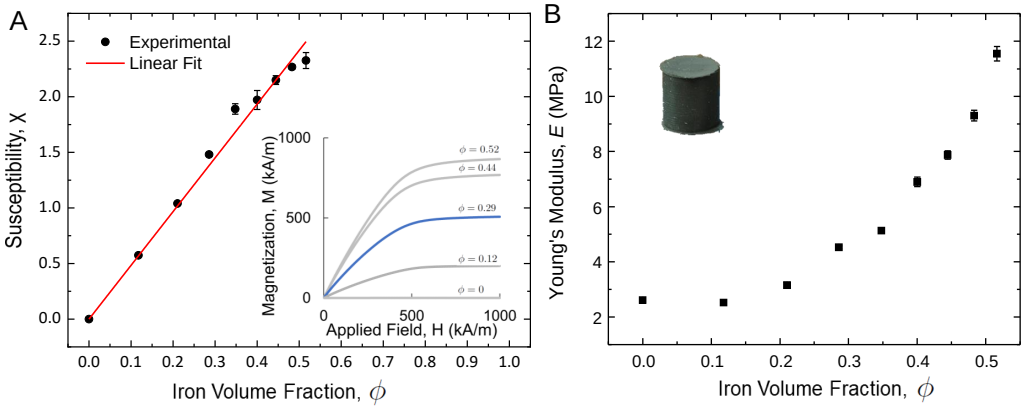

Figure 3.2: A) Increase in magnetic susceptibility with Fe loading. Vibrating magnetometer susceptibility data as a function of Fe particle volume fraction. mean +/- stdev, n = 3. Inset: Magnetization vs applied field curves highlight saturation at 550 kA/m (B = 0.7 T). B) Young's modulus of homogenous MRE specimens under uniaxial compression (λ_{max}= 0.75), mean +/- stdev for number of specimens, n=3. Base-to-catalyst ratio is 10:1. Inset: Example specimen with the cylindrical shape (diameter, d = 6.36 and height, h = 6.35 mm) used for dynamic mechanical analysis.

Using magneto-vibrometry, the magnetization and susceptibility of the MRE composite were collected at various iron volume fractions and are presented in Fig. 3.2a. Magnetization, defined as the density of induced magnetic dipoles, is plotted vs. the applied magnetic field, H, in the inset. No magnetization is detected when the iron particles are not added to the

matrix ($\phi = 0$), demonstrating that the neat elastomer is insensitive to the magnetic field. Magnetization increases significantly with increasing volume fraction of iron, reaching a maximum magnetization strength of 837 kA/m for the highest iron loading of $\phi = 0.52$. The magnetization curves consistently saturate at an applied magnetic field of approximately 550 kA/m (B = 0.7 T) across all loadings. The magnetic susceptibility, χ , in this study is taken as the maximum slope of the magnetization vs applied magnetic field curve. The magnetic susceptibility increased linearly within the range of volume fractions investigated with a slope of 4.8 (R-square = 0.997), which is in line with values reported in the literature (χ =2.5-5.0 for 3–6-micron particles (Gorodkin et al., 2009)). Negligible remnant magnetization was observed in the MRE specimens, which is consistent with the soft magnet nature of the iron particles.

The effect of iron particle loading and base: catalyst ratio on the mechanical properties of the MRE composite was also characterized. Compression-based estimates of Young's modulus, E, for the MRE composite as a function of the iron volume fraction is depicted in Fig. 3.2b. Based on quasi-static compression testing a DMA, the 10:1 base to catalyst ratio for the PDMS matrix resulted in Young's modulus of $E = 2.61$ MPa without iron fillers ($\phi = 0$). With increasing iron filler volume fraction, the stiffness of the MRE composite increased to $E = 11.5$ MPa at $\phi = 0.52$, a 4.4 times increase in stiffness from the matrix alone. The base: catalyst ratios of 20:1 and 30:1 were also tested, yielding Young's Moduli of 882 $\pm$ 50 kPa and 267 $\pm$ 43 kPa (mean $\pm$ stdev, n = 10), respectively. The compression stiffness of the 10:1 ratio is approximately 8.75x greater than the 30:1 ratio. Silicone oil was also added as a plasticizer to further reduce the stiffness of the matrix, reaching Young's Moduli as low as 27 $\pm$ 4 kPa (mean $\pm$ stdev, n = 10). However, the silicone oil infiltrated and swelled the pre-formed MRE composite layerand was not used for the laminate buckling tests.

3.3 Numerical modeling

3.3.1 Constitutive behavior

We employ an amended energy potential to define the constitutive behavior of the phases, as defined in Eq. (1.8). In the current configuration, the equation can be rewritten as

$$w_r(\mathbf{F}, \mathbf{B}) = \rho_r \psi_r(\mathbf{F}, \mathbf{B}) + \frac{1}{2\mu_0}\mathbf{B} \cdot \mathbf{B}, \tag{3.2}$$

where ρ_r is the material density of matrix and layer phase $r \in \{m, l\}$. In this work, we consider the free-energy that can be written as the sum of elastic and magnetic part

$$\rho_r \psi_r = \rho_r \psi_r^{el} + \rho_r \psi_r^{mag}. \tag{3.3}$$

We consider the elastic part to be defined by the neo-Hookean material model. The corresponding energy function is

$$\rho_r = \frac{1}{2} G_r (\mathbf{F} : \mathbf{F} - 3) - G_r \ln(\det \mathbf{F}) + \frac{1}{2}(\ln(\det \mathbf{F}))^2, \tag{3.4}$$

where G_r is the shear modulus, Λ_r is the first Lame's parameter, and ':' denotes the double contraction operator . To model the nearly incompressible behavior of phases, we set a very high ratio between the first Lame's parameter and shear modulus, $\Lambda_r/G_r = 1000$. Following the experiments, the shear modulus of matrix is $G^{(m)} = 100$ kPa and the shear modulus ratio $G^{(l)}/G^{(m)}$ is decided according to stiffness ratio between the two layers in the specimen.

Assuming that the magnetic part of the free-energy (3.3) is only a function of magnetic field $\mathbf{B}$, the *total* Cauchy stress defined in Eq. (1.7)

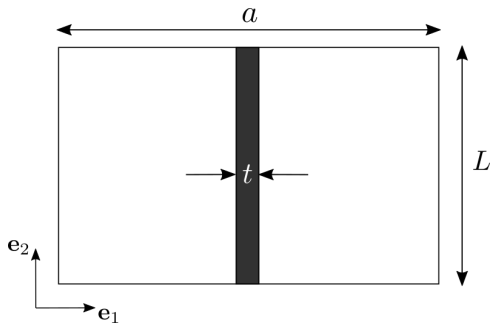

Figure 3.3: Schematic of the specimen considered in simulations.

can be written as

$$\boldsymbol{\sigma} = \rho_r \frac{\partial \psi_r^{el}}{\partial \mathbf{F}} \mathbf{F}^T + (\mathbf{M} \cdot \mathbf{B})\mathbf{I} - \mathbf{M} \otimes \mathbf{B} + \boldsymbol{\sigma}^M, \tag{3.5}$$

where

$$\boldsymbol{\sigma}^M = \frac{1}{\mu_0} \mathbf{B} \otimes \mathbf{B} - \frac{1}{2\mu_0} (\mathbf{B} \cdot \mathbf{B})\mathbf{I} \tag{3.6}$$

is the Maxwell stress tensor. In Eq. (3.5), $\mathbf{M} = -\rho_r \partial \psi_r^{mag} / \partial \mathbf{B}$ is the local magnetization field. The matrix is modeled as a magnetically inactive material. On the other hand, the magnetorheological layer is modeled to have an isotropic magnetic behavior with the same relation between the magnetization and the applied magnetic field as observed in experiments (see inset in Fig. 3.2a).

The composite is subjected to in-plane compression along the $\mathbf{e}_2$ direction and the magnetic flux is applied horizontally, $\mathbf{B} = B\mathbf{e}_1$. This loading is imposed by applying the periodic boundary conditions in terms of the displacement and magnetic potential on the boundaries of the RVE (Goshkoderia and Rudykh, 2017). The RVE is considered with height L and width a, and the thickness of the active layer is t (as shown in Fig. 3.3). To emulate the single-layer setup (as in experiments), in simulations, we consider the laminate with a very small volume fraction of active layer, i.e., $c_l = 0.01$; hence, $t = 0.01a$. We consider a range of values for the height of

RVE, L, the reasoning of which is discussed below in the instability analysis subsection.

The governing equations Eq. (1.1) and (1.11) are evaluated by means of finite element code COMSOL Multiphysics 6.0.

3.3.2 Instability analysis

To trigger the onset of instability in MRE laminates, small geometrical imperfections are imposed on the layer in terms of the function $f(y) = A\cos(2\pi y/L)$. We ensure that the geometrical perturbations do not affect the predicted critical strains by choosing the perturbation amplitude to be sufficiently small, $A/t = 10^{-3}$. We determine the onset of instability by monitoring the rate of horizontal displacement of the active layer's center point. To illustrate this method, as an example, we show the instability prediction in the MRE layer under zero magnetic field. Figure 3.4a shows the dependence of normalized horizontal displacement $\tilde{u} = u/t$ on the stretch for the RVE with L/t =11.11 . The displacement curve has a nearly-linear variation with stretch and exhibits a change in the slope upon the onset of instability. This change in slope is clearly visible through the $d\tilde{u}/d\lambda$ (red) curve. In particular, during the transition in slope, $d\tilde{u}/d\lambda$ attains a local minimum value marked by the red circle. We identify this change in behavior as the onset of instability and the corresponding stretch value as the critical stretch λ_c at that particular RVE's height L.

The critical buckling wavelength, L_c, is identified by the corresponding value of critical stretch values. In particular, when the height of RVE is the same as the wrinkling wavelength ($L = L_c$), the composite develops instability at a comparatively smaller deformation level (or higher stretch values). To this end, in Fig. 3.4b, we show the dependence of λ_c on the wavelength L or RVE's height. We observe that the critical stretch attains a local maximum at the value of L/t= 11.11 (red circle), which is the buckling wavelength for the considered example, and the corresponding stretch value

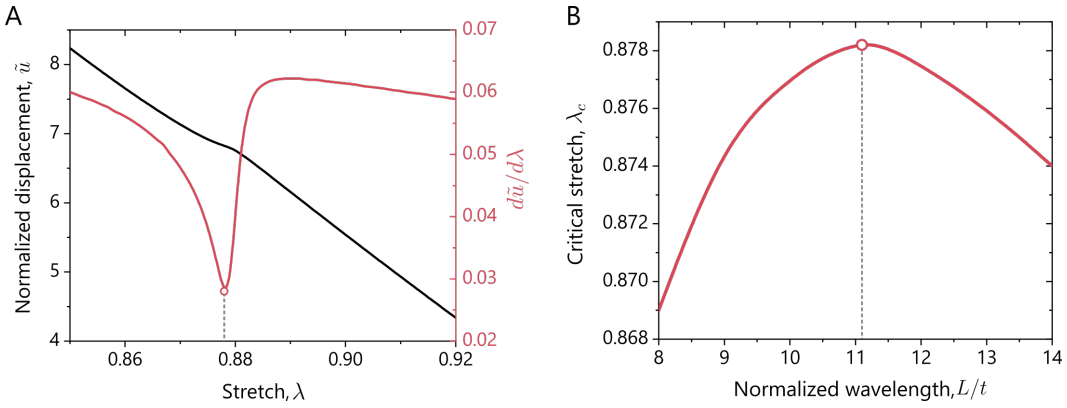

Figure 3.4: A) A representative example of critical stretch detection by analyzing the rate of change in horizontal displacement. B) The dependence of critical stretch on RVE's height.

is the critical stretch of the composite. The procedure is repeated for different values of the magnetic field to identify the change in critical stretch.

3.4 Results

3.4.1 Variation of critical stretch

Figure 3.5a displays images of this experimental wrinkling behavior of a single MRE laminate specimen (MRE layer, $\phi = 0.29$, t $= 306 \pm 2.4$ μm) under various states of pre-compression (λ_0) at continually increasing applied magnetic fields. The stiffness ratio of the laminate with $\phi = 0.29$ particle loading, and no applied field, was $E_l/E_m = 15.97$ (E_l – Young's modulus of the MRE layer 4.76 $\pm$ 0.35 MPa vs – E_m Young's modulus of the elastomeric matrix 298 $\pm$ 16 kPa) based on the compression measurements. Without any applied magnetic field, Fig. 3.5a shows that the laminate geometry has not wrinkled at a pre-compression of $\lambda_0 = 1.00$ or $\lambda_0 = 0.93$. However, at a pre-compression of $\lambda_0 = 0.89$, the onset of wrinkling in the laminate has already begun, and it is detectably wrinkled at $\lambda_0 = 0.86$. While $\lambda_0 = 0.93$

showed no wrinkling when the field was off, the onset of wrinkling was observed when the field was raised to 0.6 T. The amplitude of wrinkling appears to quickly plateau as the field exceeds the saturation strength of 0.7 T. Higher compression ($\lambda_0 = 0.89$) resulted in wrinkling without the aid of magnetic stiffening, as indicated by $\lambda_c > 0.92$ in Fig. 3.5c but applied magnetic field did increase the amplitude of the wrinkled MRE layer.

Strain-sweep experiments were performed with fixed applied magnetic fields of 0.2, 0.4, 0.6, 0.8, 1.0, 1.4, and 1.8 T. The critical stretch ratio of each strain-sweep experiment is plotted against the applied magnetic field in Fig. 3.5c, and it indicates that without any magnetic field, the sample will begin to wrinkle around $\lambda_0 = 0.92$. Low applied fields (¡0.2 T) resulted in minimal change to λ_c. A modest level of the applied field (0.6 T) reduced the compression necessary to achieve wrinkling from $\lambda_c = 0.92$ to 0.97. Past 0.7 T, the critical wrinkling point appears to plateau at $\lambda_c = 0.97$, which correlates with the saturation field strength of the magnetization curves in Fig. 3.2a. Saturation may also be a factor in the applied field sweep of Fig. 3.5b, as indicated by the plateau in wrinkling amplitude above 0.6-0.7 T for the pre-compression states of $\lambda_0 = 0.89$ and $\lambda_0 = 0.93$.

Combining the critical stretch ratio results, two dominant features of magnetic tuning are observed. First, the MRE laminate consistently wrinkles at lower strains when the magnetic field is applied (1.8T) compared to only mechanical loading (0T). An applied magnetic field produced a marked increase in the critical stretch ratio. The average change in stretch critical ratio was $\Delta\lambda_c = 0.045 \pm 0.012$ between 0 and 1.8 T, which is effectively a 5% change in the critical stretch ratio. While a seemingly small value, this 5% shift is more than sufficient to reversibly trigger the wrinkling instability by cycling on and off the magnetic field at modest pre-compressions. Shifts in the critical stretch ratio in the range of 0.04-0.05 were observed at the lower, post-saturation applied field of 0.8 T, indicating that reversible buckling could be leveraged at more modest magnetic fields.

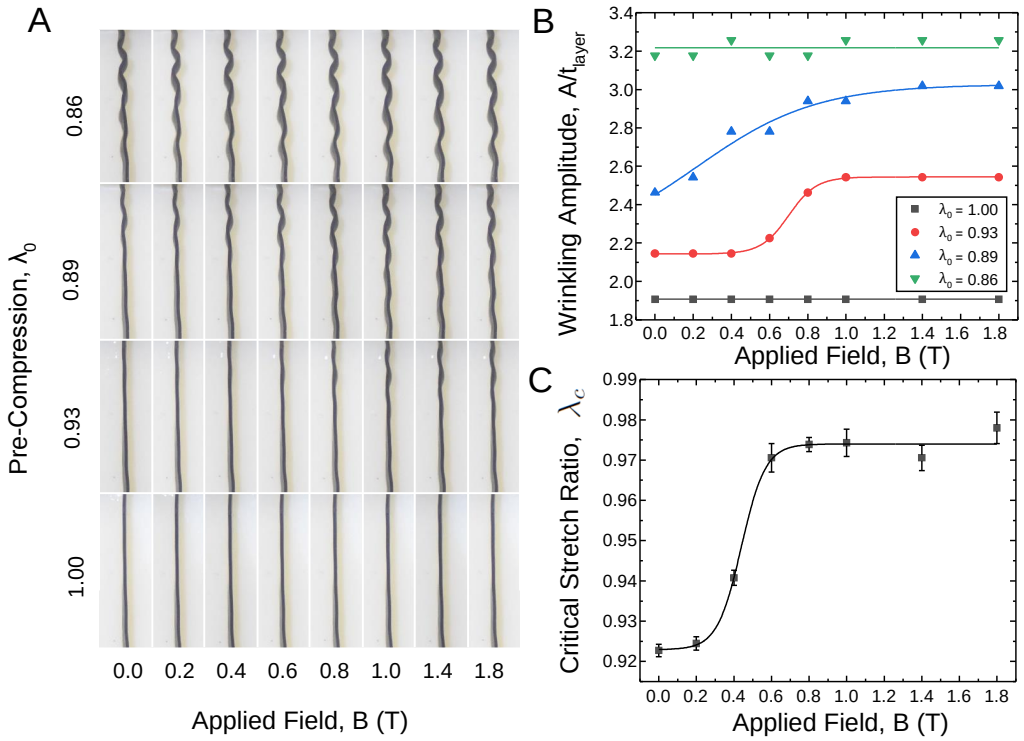

Figure 3.5: Magnetic field triggers wrinkling instability. Experimental results of specimen under combined axial compression and transverse magnetic field. A) Image array of single layer MRE under fixed pre-compression and increasing applied field. Width of each image is 4.8 mm (ϕ =0.29, t= 306 $\pm$ 2.4 μm). B) Plot of average amplitude of wrinkled MRE layer as function of pre-compression and applied magnetic field. Note: no significant change in amplitude observed in $\lambda_0 = 1.00$ (pre-buckled) and $\lambda_0 = 0.86$ cases (post-buckled). C) Critical stretch ratio determined from strain sweep experiments at fixed B-fields.

Next, we studied the tuning of critical stretch ratio in MREs numerically. Following the experiments, the soft matrix is modeled with an initial shear modulus G_m =100 kPa ($E_m \approx 300$ kPa and poisson's ratio, ν_m =0.5), and the stiffness ratio between the MRE layer and matrix is $G_l/G_m = 16$. The experimental data (n = 10) and the computationally predicted critical stretch ratio vs magnetic field curves are plotted in Fig. 3.6. The computational model captures the qualitative trend of the experimental data, exhibiting the initial reduction and then plateau in the critical stretch with increasing field strength. However, the model predicted quantitatively higher critical deformation levels for all values of the applied field. This is largely due to the experiment fabrication and testing variability issues, which lead to the premature triggering of the wrinkling instability. The thinner MRE layer specimens exhibit earlier wrinkling initiations than the thicker MRE layers. The trend in thinner MRE layers wrinkling at lower stretch ratio is clearly seen in the color coding (red – thinner, blue – thicker) of the data in Fig. 3.6. We found that the trend observed here in the experiments can be attributed to the geometric imperfections. In particular, we observed that the wrinkling detection method used on the experimental data has higher sensitivity to the imperfections in thinner MRE layers. Interestingly in the mechanical-only case (0T), the hyperelastic material model predicted a slightly higher critical stretch ratio (λ_c =0.878) than the linear elastic model (λ_c =0.87 (Li et al., 2013)). Although small, this difference highlights the influence of the choice of a constitutive model for the wrinkling mechanics simulation. Furthermore, we note that although the MRE layer is modeled as a homogenized continuum material, it is a composite with iron particles embedded in a soft matrix. Therefore, it may exhibit highly non-linear mechanical behavior (for example, strain stiffening), which are not accounted for in the present study. These material behavior uncertainties can induce additional discrepancies and require full multiscale modeling to be resolved.

The computational model was next utilized to investigate the local

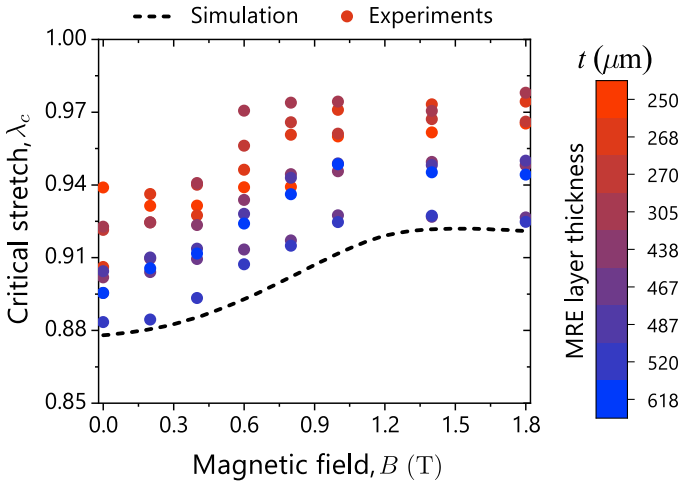

Figure 3.6: Computational model captures trend in magnetic tuning of critical stretch ratio. Plot of critical stretch ratio vs magnetic field strength with experimental data (dots) and simulation prediction (dashed line). Experimental data is color coded by the nominal MRE layer thickness of each specimen (n = 10). In the simulations, a periodic RVE of the composite with 1% volume fraction of MRE layer is considered. Note: thicker MRE specimens (blue) most closely match the predicted instability curve, while thinner MRE layers (red) wrinkle earlier.

magnetic field distribution within the MRE laminate composite as a function of mechanical compression. Color plots of the magnetic field intensity, $|\mathbf{B}| = \sqrt{B_x^2 + B_y^2}$, are shown in Fig. 3.7a under an applied magnetic field of $B = 1.8$ T for mechanically-applied stretch ratios of λ =1, 0.9, and 0.8. In the reference configuration, the magnetic field intensity is uniform and equal to the applied field of 1.8 T. However, as wrinkling initiates in the MRE layer, the magnetic field starts to vary along the length of the MRE layer due to the perturbed wrinkling geometry. The magnitude of this field variation increases as more mechanical compression is applied, reaching approximately a 10% deviation from the applied field intensity of 1.8T at λ =0.8. Further focusing on this variation, Fig. 3.7b-c show the local magnetic field along the interface between the MRE layer and soft matrix,

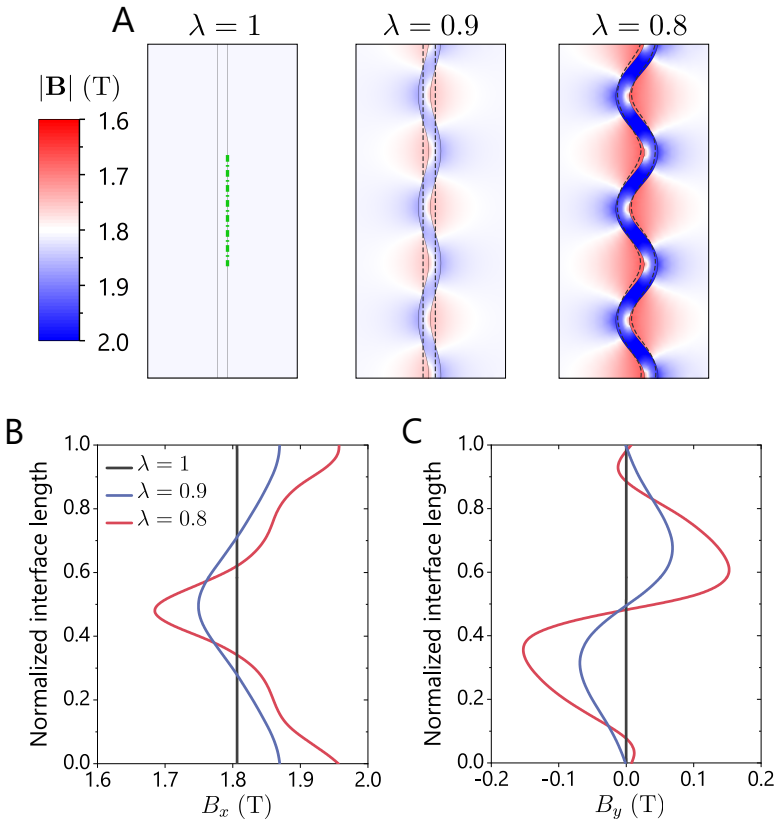

Figure 3.7: Magnetic field amplifies wrinkling amplitude with geometry-induced local field distribution. A) Color plot of magnetic field intensity at an applied field of 1.8T with applied stretch ratios of λ =1, 0.9 and 0.8. Black dashed line denotes the deformation configuration of the MRE layer without magnetic field applied (0T). Plots of the local magnetic field, separated into B) aligned (B_x) and C) orthogonal (B_y) directions to the applied field, evaluated along the MRE layer/soft matrix interface at the undeformed, pre-wrinkling and post-wrinkling stretch ratios. The dotted green line in panel A denotes the single wavelength of the interface length plotted in panels B and C.

separated into directions aligned (B_x) and orthogonal (B_y) to the applied field. Figures 3.7b-c zoom in on a single wavelength of the MRE layer, where the wavelength location is denoted by the green dash-dotted line in Fig. 3.7a. The magnetic field intensity increases at the peaks of the wrinkled MRE interface, but it decreases at the troughs in the wrinkled MRE interface. At small wrinkling amplitudes (modest applied stretch ratios), the magnetic field at the MRE layer interface nearly follows the profile of the wrinkling displacement. However, at larger wrinkling amplitudes, the magnetic field in the x-direction becomes even more intensely localized to the crest and peak points along the MRE interface, and the profile does not follow a single frequency sine wave. For B_y, the magnetic intensity is zero at the crest and peaks of the wrinkled MRE interface, as the surface normal of the MRE layer is aligned with the field at these points. Away from these points, the vertical component, B_y, of the magnetic field cycles between positive and negative values according to the orientation of the surface relative to the applied magnetic field. This component is relatively small compared to the magnitude of the applied field (0.2 T vs. 1.8 T). However, the introduction of these attractive field variations in the vertical direction likely promotes increased wrinkling amplitudes in the post-wrinkling regime. To highlight the amplitude increase caused by the magnetic field, the deformed configuration of the MRE layer under mechanical loading only (0T) has been included as a dashed outline in the color plots of Fig. 3.7a. Psarra et al. (2017) made a similar observation in their MRE surface layer study, suggesting that alternating attractive fields develop across the wrinkled MRE surface due to the wavy geometry. At a minimum, the localized magnetic field correlates with the early initiation of wrinkling instability and the increase in wrinkling amplitude. While other mechanisms could also be contributing to this tuning capability, such as magnetostriction and induced stiffening effects, these seem less dominant than the interaction of wrinkle geometry and the magnetic field.

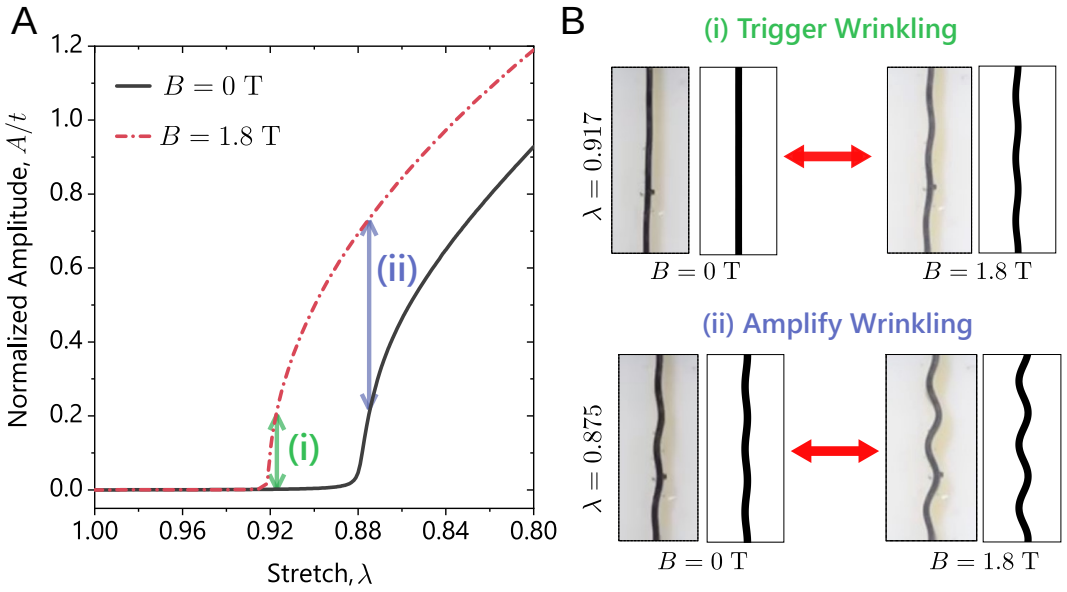

Figure 3.8: Leveraging Magnetic Field to Control Wrinkling Behavior. A) Plot of modeling predictions of normalized wrinkling amplitude, A/t, vs stretch ratio, λ, with and without applied magnetic field. Magnetic tuning features include (1) triggering wrinkling at lower compressions, (2) amplifying the amplitude of the wrinkling pattern in post-buckling, and (3) maintaining the wrinkling amplitude under varying compression by simultaneous adjusting the magnetic field. B) Representative example of (1) triggering wrinkling with magnetic field (1.8T) at a pre-buckling stretch ratio ($\lambda_0 = 0.917$) and (2) amplifying wrinkling amplitude at post-buckling stretch ratio (λ_0 =0.875). MRE layer thickness, $t = 466 \pm 27$ μm.

A key contribution of this work was the experimental validation of two magnetic field tuning mechanism in the MRE laminate, specifically the ability to trigger wrinkling and the ability to amplify the amplitude of wrinkling in the post-wrinkling regime. We highlight these two tuning features in Fig. 3.8a, using a plot of normalized wrinkling amplitude (A/t) vs. stretch ratio for an "active" (1.8T) and "inactive" (0T) magnetic field scenario. This diagram serves as a practical design guide on how much to pre-compress the laminate in order to maximize the amplitude increase

induced by the magnetic field. A representative example of (i) triggering wrinkling and (ii) amplifying the wrinkle amplitude are shown in Fig. 3.8b, with side-by-side experimental and simulation comparisons. The speed of triggering the wrinkling is dependent on the activation speed of the magnet. In this study, the magnet field strength was slowly incremented in order to access the effects of a quasistatic field. However, for a dynamic tuning operation, the magnet could be programmed to step more rapidly and in fewer increments between target field strengths.

3.4.2 Influence of magnetic field direction on instability development

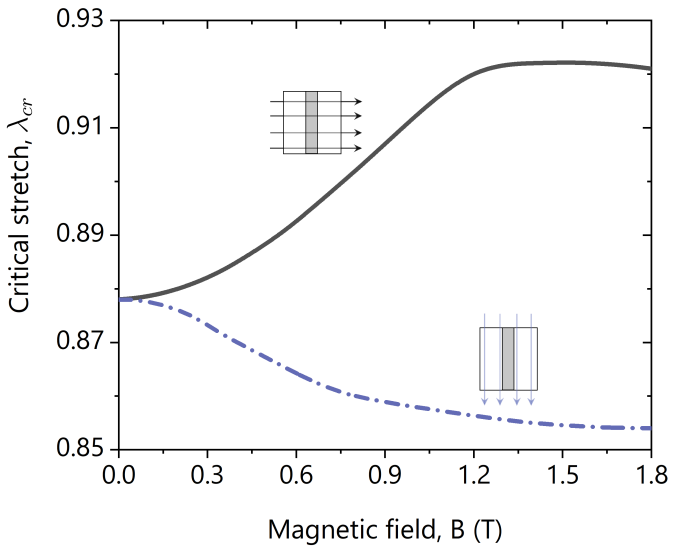

Figure 3.9: Critical stretch vs the magnitude of magnetic field with field directions perpendicular (solid black) and parallel (dash-dotted blue) to the MRE layer.

Thus far, we have presented an experimental and numerical study on the instability development in MRE laminates subjected to magnetic field

applied perpendicular to the MRE layer. In this subsection, we study the onset of wrinkling when the magnetic field is applied parallel to the MRE layer. To this end, in Fig. 3.9, we plot the critical stretch as the function of the magnetic field magnitude (blue dash-dotted curve). For comparison, we have also added the results for magnetic field applied perpendicular to the MRE layer (black solid curve). We observe that when the magnetic field is applied parallelly, higher deformation levels are required to trigger the onset of instability. This is in contrast to the case when the field is applied in the perpendicular direction (compare the solid and dash-dotted curves in Fig. 3.9). In both the cases, however, the value of critical stretch saturates at higher magnitudes of magnetic field. These results further highlight the tunability of instability-induced pattern transformations offered by the variations in the magnitude and the direction of magnetic field.

4 MAGNETICALLY-PROGRAMMED INSTABILITY-DRIVEN STRUCTUCTURAL TRANSFORMATIONS*

4.1 Introduction

The ability to reconfigure the microstructure of architected materials forms the basis for designing material-based systems with switchable functionalities (Frey et al., 2019; Kamperman and Synytska, 2012; Zhang et al., 2021b; Zhu et al., 2017; Wang et al., 2017). Moreover, microstructural transformations equip the materials with shape-shifting and morphing capabilities (Erb et al., 2013; Zhang et al., 2021e; Frenzel et al., 2017), which are critical for various applications, including soft robotics (Chen et al., 2018) and deployable devices (Bobbert et al., 2018). *Soft* deformable architectures represent an ideal platform for the design of such tunable materials, thanks to their morphing capability in response to external stimuli (Kim and Zhao, 2022; Palagi et al., 2016; Geryak and Tsukruk, 2014; Behl and Lendlein, 2007; Pal and Sitti, 2023; Xia et al., 2022). Moreover, elastic instability phenomenon observed in these materials has been identified as a powerful tool to trigger sudden but controlled and reversible microstructural transformations (Mullin et al., 2007; Kochmann and Bertoldi, 2017; Jiang et al., 2019).

Instability-driven microstructural transformations are studied in various architected materials. For example, periodic lattices exhibit mechanical instability by sequential buckling of inner elements (Kang et al., 2014; Frenzel et al., 2016). In soft porous architectures, the voids collapse in a cooperative manner leading to an internal reconfiguration of the microstructure (Mullin

*This chapter is adapted from the manuscript submitted as N. Arora, V. Chen, Y. Xiang, A. Juhl, P. Buskohl, and S. Rudykh, Magnetically-programmed instability-driven pattern transformations in soft materials.

et al., 2007). Moreover, multi-phase architected composites (Cho et al., 2016) can develop a rich variety of post-buckling patterns (Triantafyllidis and Maker, 1985; Li et al., 2019a; Jiang et al., 2006). Fiber and layered composites develop wavy (or sinusoidal) buckling patterns (Li et al., 2013, 2018a) that may transform into twinning (Li et al., 2022). Soft particulate composites exhibit the formation of ordered anti-symmetric domains in the post-instability regime, in addition to the wavy buckling patterns (Li et al., 2019a). In all these architectures, the characteristics of the buckling patterns – periodicity and amplitude – are defined by the initial microstructure patterning and mechanical properties of constituent materials. However, the geometry of admissible patterns is highly limited in this mechanics-centric design approach and, in general, the patterns are spatially homogeneous and periodic. This also restricts their employability in challenging applications such as soft robotics and actuation (Hu et al., 2018; Shepherd et al., 2011; Ze et al., 2022), prosthetics (Chortos et al., 2016), wearable technologies (Zeng et al., 2014; Ho et al., 2022; Fu et al., 2018; Amjadi et al., 2016), and mechanical computers (Yasuda et al., 2021; El Helou et al., 2021), which demand local control on the reconfigurability of the architected materials.

Here, we present how the magneto-mechanical coupling in soft architected materials can be exploited to break the limit of admissible instability-induced patterns. We consider soft particulate composites with periodically distributed stiff magnetic inclusions in a soft matrix (Fig. 4.1a). An individual magnetic inclusion has one of either magnetic polarization: towards the positive or negative $x-$direction (Fig. 4.1b). We first compare the distinct microstructure evolution in composites with magnetically active and inactive inclusions, via applied deformation. We then investigate the different classes of buckling patterns, based on the competition between the mechanical and magnetic interactions among the inclusions. Through our experiments and simulations, we show that in the magnetically-dominated regime, the reconfiguration of inclusions is solely guided by the local mag-

netic forces, which can be pre-programmed. Finally, we show that the soft composites can develop arbitrary binary (two-level) instability patterns, based on the encoded magnetic polarity-arrangement. We showcase the diversity of the admissible structural transformations through a series of information embedding demonstrations, including alphabet shape matching and Morse code.

4.2 Experiments

4.2.1 Specimen preparation

The magnet array specimens are fabricated by setting ($N = 18$) neodymium magnets (B422, 6.35 $\times$ 3.175 $\times$ 3.175 mm^3, K&J Magnetics) in a silicone matrix (Mold Max 10T, Smooth-On). To achieve the spatial arrangement of magnets, we insert them into an alignment holder (blue part in Fig. 4.2) printed using Objet260, Stratasys. The magnets are arranged with a distance 6.35 mm between their centers, and are transferred into a two-part mold for silicone casting with inner dimensions of 114.3$\times$51.2$\times$5.15 mm^3. Square wells of 0.6 mm depth are introduced to the inner surfaces of the mold pieces (transparent and yellow parts in Fig. 4.2) to maintain magnet orientation after the alignment holders are removed (blue and green parts in Fig. 4.2). Silicone is mixed and degassed prior to pouring into the mold. The open ends of the mold are capped and allowed to cure for 24 hours. For fabricating the purely mechanical particulate composite, we demagnatized the magnets by heating at 250°C for more than 20 hours.

To ensure a strong bonding between the magnets and the surrounding silicone, the magnet surfaces are chemically treated with a silane adhesion promoter (A-306, Factor II). The mold pieces are treated with a release agent (Ease Release 2831, Smooth-On) to prevent unwanted adhesion to the silicone.

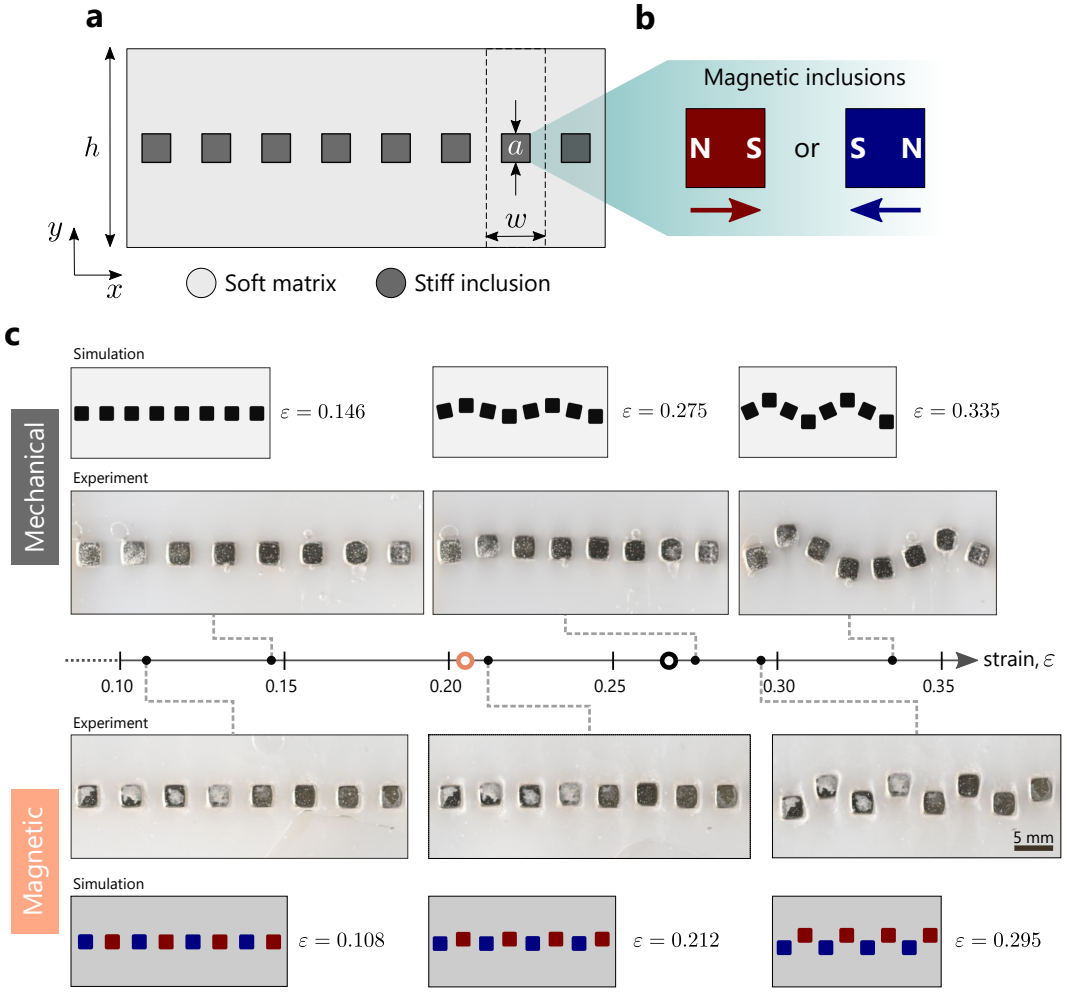

Figure 4.1: **Schematics and comparison of microstructure evolution in mechanical and magnetic composite with deformation. a**, Schematic of a periodic particulate composite with square rigid inclusions. The primitive unit cell is bounded by dashed lines. **b**, The square inclusion has either of the two orientations of magnetic polarity: either parallel or anti-parallel to the x-axis. **c**, Experimental and simulation images of mechanical (top) and magnetic composite (bottom) at different levels of compressive strain, ε. The orange hollow circle on the strain scale marks the experimental critical strain value for the magnetic composite, whereas the black hollow circle marks it for the mechanical composite. The results are shown for the composites with spacing ratio $\xi = a/w = 0.5$.

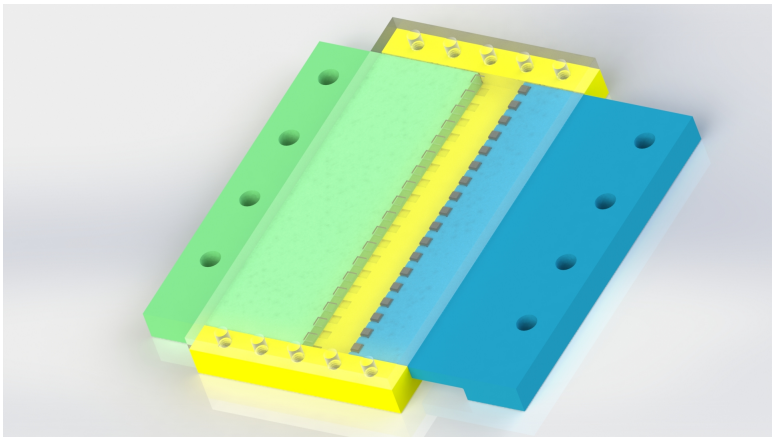

Figure 4.2: **Mold and alignment jigs for setting magnets.** The transparent and yellow parts define the top and bottom of the final specimen with recessed wells to hold magnets in place. The blue and green parts are used to transfer and align magnets into the mold.

4.2.2 Experimental set-up and testing

The specimens are mounted between the two transparent parallel plates made of acrylic to prevent out-of-plane deformation (Fig. 4.3). A 3D printed spacer is used to maintain the distance between the acrylic plates. The interior surfaces are lubricated with silicone oil (1000 cPs, Brookfield) to reduce friction during compression. The specimens are uniaxially compressed using a plunger, which is attached to the gantry plate of a stepper motor-based linear actuator (C-Beam, Openbuilds). The deformation images of the specimen are collected with a digital camera (Nikon Z7) coupled with a 60 mm macro lens. Compression and image acquisition are synchronized using a prototyping board (Arduino UNO R3).

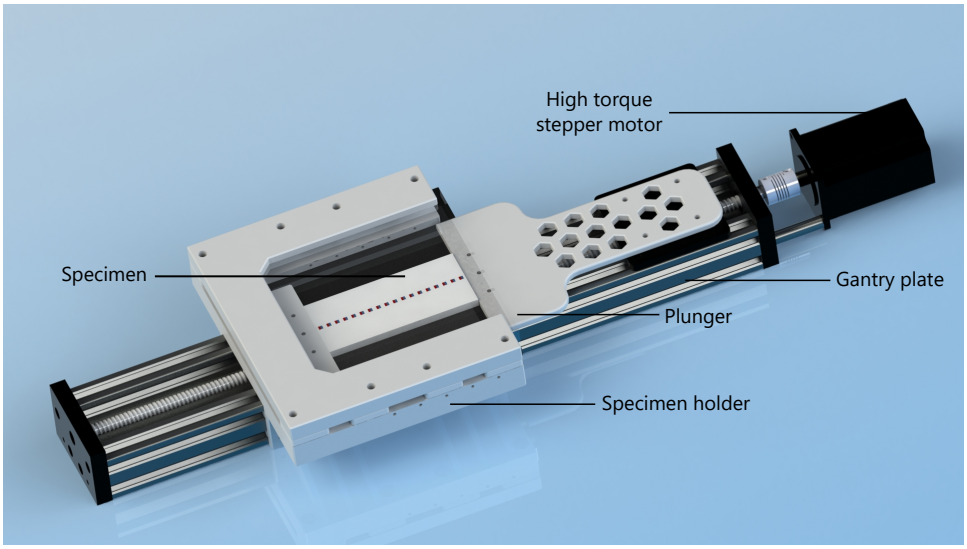

Figure 4.3: Schematic of compression test setup.

4.3 Numerical modeling

The soft matrix is modeled as nearly incompressible neo-Hookean hyperelastic material (3.4). We set a high ratio between the first Lame's parameter and shear modulus, $\Lambda/G = 10^2$, to model the nearly-incompressible behavior of the soft matrix. The matrix material characterized by the initial shear modulus $G_m = 0.1$ MPa. The stiff inclusions are modeled as a rigid material.

The soft matrix is considered to be magnetically inactive and does not have any remnant magnetization. The magnetic inclusions are modeled as hard-magnetic materials with residual magnetic flux density defined in terms of the magnetization $\mathbf{M}$. The magnetic force and torque experienced by each inclusion, due to the presence of other inclusions, are evaluated by integrating the electromagnetic stress tensor over its boundary. The *total* stress tensor is then calculated by incorporating these magnetic forces and torques, thereby, establishing the magneto-mechanical coupling.

The specimen is subjected to in-plane deformation, with compression

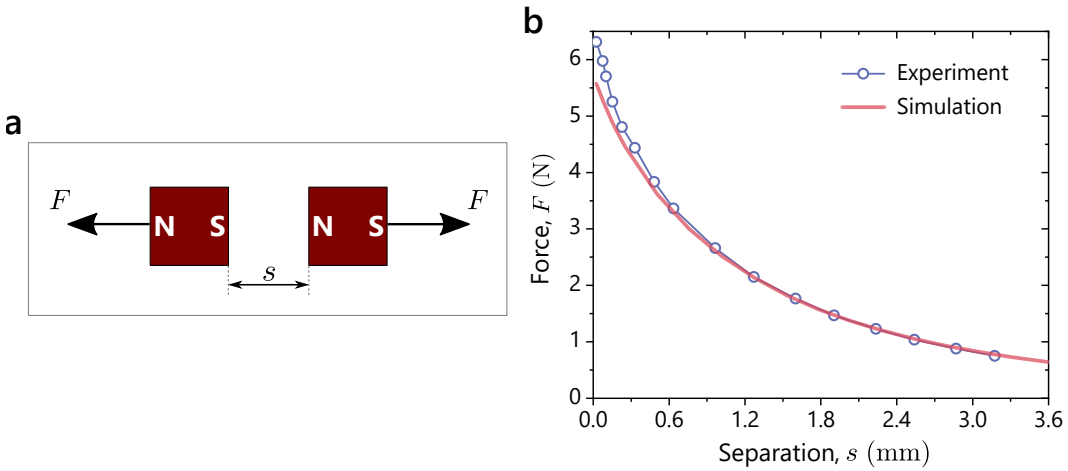

Figure 4.4: **Characterization of magnets.** **a**, Schematic of setup modeled in simulations to evaluate the attraction force between the magnets. **b**, Experimental and simulation data for attraction force versus the separation distance (experimental data is taken from K&J Magnetics website.

along the vertical direction. In the simulations, the macroscopic mechanical loading is implemented by applying periodic boundary conditions. The applied macroscopic deformation gradient is

$$\bar{\mathbf{F}} = \bar{F}_{11}\mathbf{e}_1 \otimes \mathbf{e}_1 + (1-\varepsilon)\mathbf{e}_2 \otimes \mathbf{e}_2 + \mathbf{e}_3 \otimes \mathbf{e}_3 \tag{4.1}$$

where ε is the compressive strain and $\bar{F}_{11}$ is evaluated using the traction-free left and right boundaries. To avoid rigid body motions, the displacement of the bottom-left point is constrained. We assume that there are no surface and free currents within our system and the specimen is subjected to quasi-static mechanical compression. The resulting governing equations Eq. (1.1) and (1.11) are evaluated by means of finite element code COMSOL Multiphysics 6.0.

4.3.1 Magnet characterization

To evaluate the magnitude of magnetization M, we use the experimental magnetic force data for the B422 magnets provided by K&J Magnetics website. We model the same setup in our simulations, as shown in Fig. 4.4a. In particular, two magnets with identical polarity are placed horizontally with a separation s between them. The experimental attraction force versus separation data is plotted as blue circles in Fig. 4.4b. In simulations, by performing iterations over the value of magnetization's magnitude M to closely match the experimental data, we obtain $M = 900$ kA/m. The corresponding attraction force data is shown using red curve in the plot.

4.3.2 Instability analysis

In simulations, we consider a sufficiently large RVE with $N = 24$ primitive unit cells. As examples, undeformed RVEs of the purely mechanical composite and magnetic composite with repulsion arrangement are shown in Fig. 4.5. Each RVE is compressed uniaxially along the $x-$direction with periodic boundary conditions applied on its edges. To trigger the post-buckling patterns in the particulate composites, the initial geometry is perturbed with small and random imperfections in the form of the inclusions' vertical position. We ensure that the geometrical perturbations do not affect the predicted critical strains or the instability-induced patterns by choosing the perturbation amplitude to be sufficiently small, $r/a = 10^{-4}$. Here, a is the side length of square inclusion and r is the perturbation amplitude, as shown in Fig. 4.6.

We determine the onset of instability in our simulations by monitoring the rate of vertical displacement of the inclusions. To illustrate the method, as an example, we show the instability prediction in a magnetic composite with the repulsion arrangement. Figure 4.7 shows the dependence of an inclusion's center point vertical displacement v (gray curve) and its rate

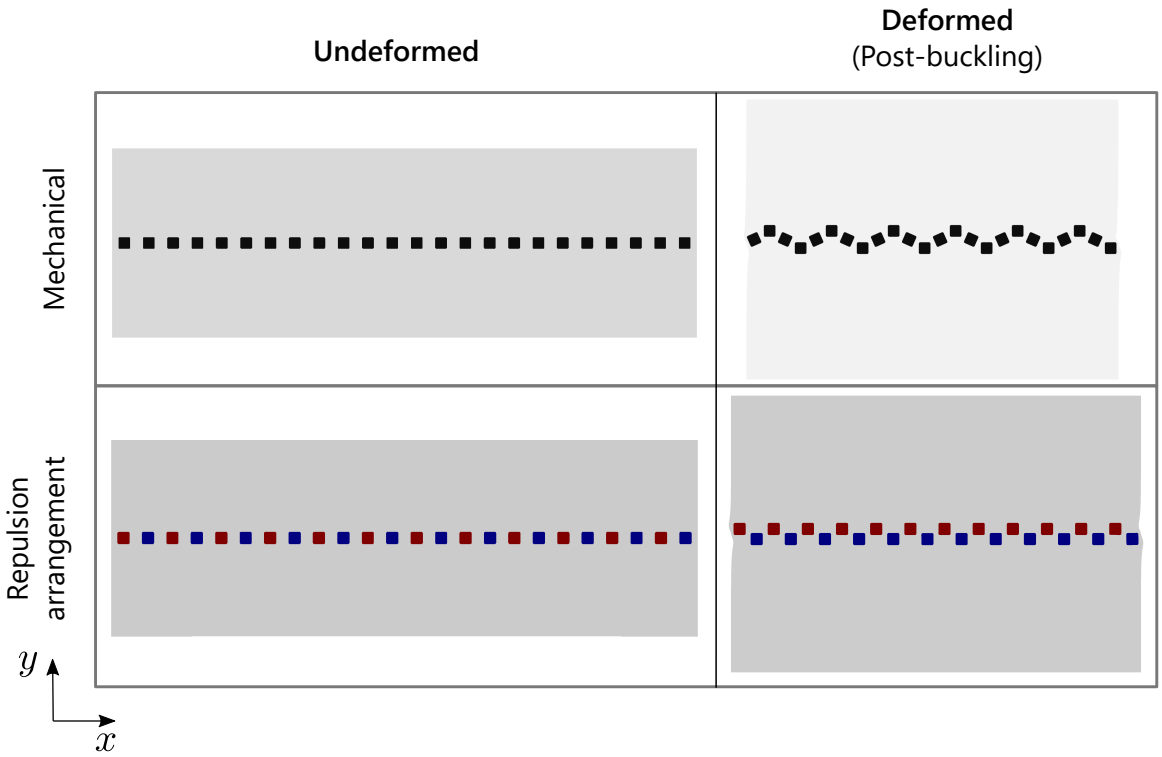

Figure 4.5: **Representative volume elements of composites considered in simulations.** Left panel: Mechanical composite (top), magnetic composite with repulsion arrangement (bottom). Right panel: The corresponding deformed (post-instability) configuration of the composites at strain levels $\varepsilon = 0.335$ and $\varepsilon = 0.295$, respectively. In magnetic particulate composite, blue and red colors are used to indicate inclusions with negative and positive magnetic polarity, respectively.

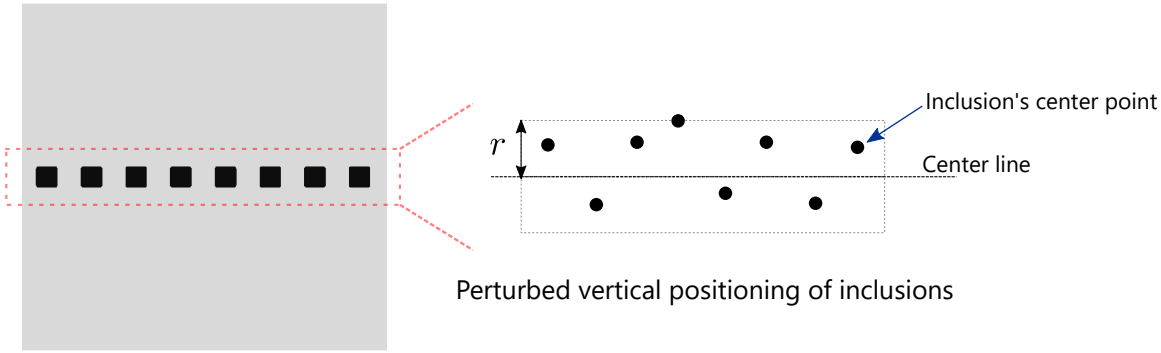

Figure 4.6: A representative example of an RVE showing the geometrical perturbations in the inclusion's center point location.

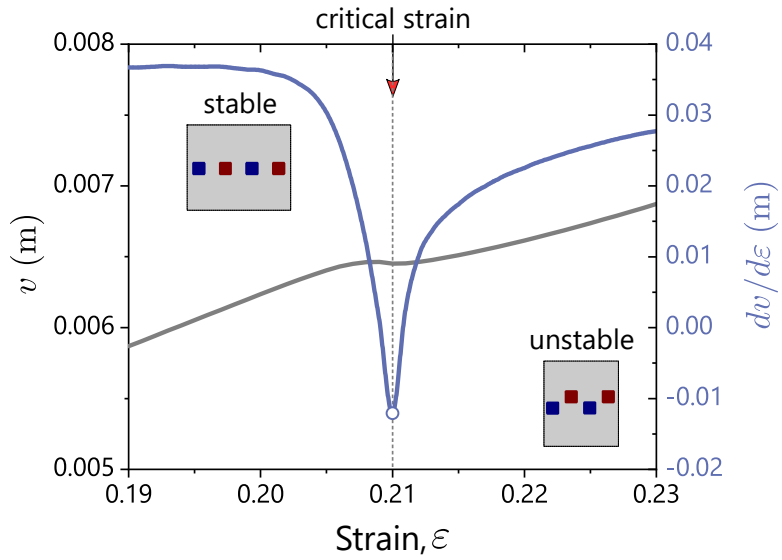

Figure 4.7: A representative example of critical strain detection by analyzing the rate of change in vertical displacement $dv/d\varepsilon$.

of change $dv/d\varepsilon$ (blue curve) as the function of compressive strain ε. The displacement curve has a nearly-linear variation with applied strain, and exhibits a change in the slope upon the onset of instability. This change in slope is clearly visible through the $dv/d\varepsilon$ curve. In particular, during the transition in slope, $dv/d\varepsilon$ attains a minimum value marked by blue circle. We identify this change in behavior as onset of instability and the corresponding strain value as critical strain ε_{cr}. The magnetic composite with repulsion arrangement considered here develops instability at $\varepsilon_{cr} = 0.210$.

4.4 Results

4.4.1 Mechanical and magnetic instability patterns

To understand the influence of using magnetically active inclusions in the particulate composite, we start with comparing its response to that of the *purely mechanical* counterpart (with magnetically inactive inclusions). Geometrically, the composite is described using the spacing ratio $\xi = a/w$; w is the width of the primitive unit cell (bounded by dashed lines in Fig. 4.1a) and a is the side of the rigid square inclusion. The magnets have a square cross-section with side $a = 3.175$ mm and out-of-plane thickness $d = 6.35$ mm. As an illustrative example, we consider the magnetic composite in which the adjacent inclusions have opposite polarities. Physically, the magnets are placed in a fashion such that the adjacent magnets repel each other. Note that for a fair comparison, the mechanical particulate composite is prepared using demagnetized magnets. The inclusions are periodically placed with a distance $w = 6.35$ mm between their centers, such that the spacing ratio is $\xi = 0.5$. In the simulation images of particulate composite, the magnetically inactive inclusions are shown in black color, whereas the magnets are shown in red and blue colors to represent positive and negative polarization, respectively.

Figure 4.1c shows the direct comparison between the evolution of microstructure in the mechanical and magnetic composites as the function of applied compressive strain ε. Both composites are subjected to large deformations, up to the compressive strain level of $\varepsilon = 0.35$. The mechanical composite maintains its initial periodicity of one unit cell up to the critical deformation level $\varepsilon_{cr} = 0.267$ (marked by a hollow black circle on the strain-scale in Fig. 4.1c). With the onset of instability, the soft composite breaks its initial periodicity ($N = 1$) and the rigid inclusions rearrange into the wavy pattern with a new periodicity of $N \approx 4$. On further deformation, the amplitude of the buckling pattern further accentuates, as can be seen in the deformation images at strains $\varepsilon = 0.275$ and $\varepsilon = 0.335$.

In the magnetic particulate composite, instability-induced microstructure reconfiguration takes place at a comparatively smaller deformation level, i.e. at $\varepsilon_{cr} = 0.205$ (marked by an orange hollow circle on the strain-scale). The decrease in critical strain can be attributed to the magnetic interaction between the inclusions. In particular, with the compression of the composite, the inclusion moves closer to each other leading to a significant increase in the magnitude of repulsive forces among the oppositely polarized adjacent inclusions. As a result, in the post-instability regime, the inclusions arrange into two rows. The alternately-positioned inclusions, having positive magnetic polarity, shift cooperatively to constitute one of the rows. The remaining inclusions with negative polarity arrange together to form the other row of the buckling pattern (see deformation image of magnetic particulate composite at $\varepsilon = 0.295$). Clearly, this two-level pattern generated in the magnetic particulate composite is strikingly distinct from the wavy-pattern observed in its mechanical counterpart.

We note that our numerical predictions agree with the experimental results. In particular, for the mechanical composite (shown in Fig. 4.1c), the simulation predicts $\varepsilon_{cr} = 0.256$ and post-buckling periodicity $N = 4$; these parameters are fairly close to the experimental ones: $\varepsilon_{cr} = 0.267$

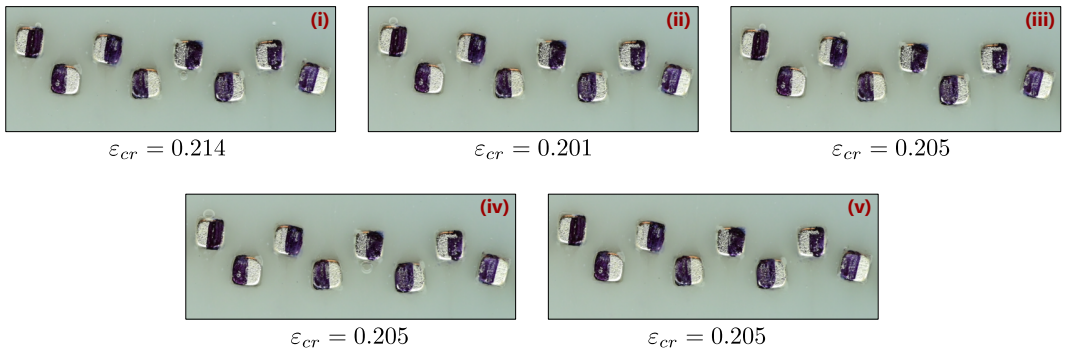

Figure 4.8: Experimental images of magnetic composite with repulsion arrangement under compressive strain of $\varepsilon = 0.35$. Roman numeral (i) to (v) on top-right of each image shows the loading cycle and the corresponding critical strains ε_{cr} are provided under the images.

and $N \approx 4.5$. For the magnetic composite, the simulation estimates $\varepsilon_{cr} = 0.210$ in comparison to $\varepsilon_{cr} = 0.205$ observed in experiments. Notably, the two-level pattern is accurately predicted in simulation as realized in experiments. Moreover, the reproducibility of this discrete pattern is verified experimentally in an additional specimen subjected to multiple loading cycles and we find that the pattern develops consistently (more details in the subsection below).

Response under multiple loading cycles

To verify the repeatability of post-buckling reconfiguration of inclusions, we prepared an additional specimen for the magnetic composite with repulsion arrangement and tested it for five loading cycles. For the first specimen, we found that in the post-instability regime, the inclusions arrange into two rows. Moreover, the critical strain for the first specimen is $\varepsilon_{cr} = 0.205$. Figure 4.8 shows the experimental images of the second specimen subjected to the compressive strain of $\varepsilon = 0.35$. We observe that in the first cycle, the composite develops instability at $\varepsilon_{cr} \approx 0.214$. In the second cycle, however, the critical strain decreases to $\varepsilon_{cr} \approx 0.201$. In the remaining

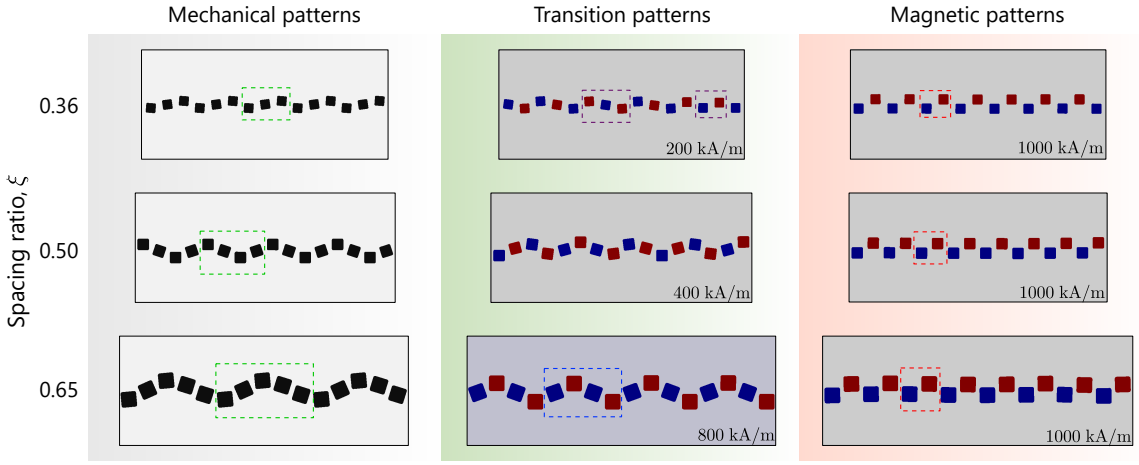

Figure 4.9: **Mechanical, transition, and magnetic instability patterns.** Simulation images of post-buckling patterns in the particulate composites with spacing ratio $\xi = 0.36$ (top row), $\xi = 0.50$ (center row), and $\xi = 0.65$ (bottom row). The results are shown for mechanical composites (left column), magnetic composites (middle and right column) with their magnetization values written at the bottom-right of each image.

cycles, the composite buckles at approximately $\varepsilon_{cr} \approx 0.205$. The average critical strain for the second specimen is $\varepsilon_{cr}^{avg} \approx 0.206$, which is fairly close to $\varepsilon_{cr} = 0.205$ of the first specimen. Notably the instability patterns developed in the composite are almost identical for all the five loading cycles, and they resemble the two-level arrangement of inclusions observed in the first specimen. This shows that the buckling patterns in the magnetic composites are reproducible across specimens and do not change when subjected to multiple loading cycles.

4.4.2 Transition from mechanical to magnetic patterns

The results thus far illustrate that the magnetic interactions between the inclusions lead to a *distinct* instability pattern from the purely mechanical

case. Next, to investigate the transition from mechanical to magnetic buckling pattern, we study how the instability characteristics change with the magnetic strength of the inclusions. We consider the composites with various spacing ratios, namely, $\xi = 0.36$, $\xi = 0.50$, and $\xi = 0.65$; the corresponding simulation results are shown in Fig. 4.9 at the compressive strains of $\varepsilon = 0.4$, $\varepsilon = 0.3$, and $\varepsilon = 0.2$, respectively.

We observe that the mechanical composites develop wavy buckling patterns and their periodicity changes with the spacing ratio (left column in Fig. 4.9). In particular, the composite with $\xi = 0.36$, $\xi = 0.50$, and $\xi = 0.65$ rearrange into the patterns with increasing periodicity of $N = 3$, $N = 4$, and $N = 5$, respectively. The elements of periodic patterns in mechanical composites are marked by green-dashed rectangles.

Next, consider the magnetic composites with a large magnetization value of $M = 1000$ kA/m (right column in Fig. 4.9). The magnets are placed such that they repel the adjacent ones (as also considered in Fig. 4.1c). In these composites, the inclusions rearrange to form the two-level buckling patterns with a periodicity of $N = 2$. This holds true regardless of the initial spacing ratio of the composites, which highlights that the formation of these patterns is dictated by the magnetic forces. The repeating elements are marked by the red-dashed rectangles in the right column.

Interestingly, for a certain range of magnetization values, the instability patterns neither resemble the mechanical patterns nor the two-level magnetic pattern. We classify these patterns as 'Transition patterns' (middle column in Fig. 4.9). For example, in the soft composite with $\xi = 0.36$ and $M = 200$ kA/m, we observe an irregular repetition of the base elements of size $N = 3$ and $N = 2$ (marked by the violet-dashed rectangles). Moreover, in the composite with $\xi = 0.50$ and $M = 400$ kA/m, the inclusions rearrange aperiodically. It is worth noting that although the design parameters – geometric placement of the inclusions and their magnetic polarity arrangement – of these composites are *periodic*, they generate these *quasi-periodic* and

aperiodic instability patterns. Exceptionally, the magnetic composite with $\xi = 0.65$ and $M = 800$ kA/m develops a strictly periodic wavy-pattern. In particular, the inclusions rearrange to give rise to a new a periodicity of $N = 4$, which lies in between of the corresponding mechanical ($N = 5$) and magnetic ($N = 2$) patterns. The repeating base element is marked by the blue-dashed rectangle. Note that the composites shown in Fig. 4.9 are a few of the representative examples. In Fig. 4.11, we present the formation of buckling patterns at various magnetization values in composites with $\xi = 0.50$.

We note that the instability development in these composites is led by two mechanisms: (i) the chain of inclusions behaves similar to a reinforced layer in a soft matrix (or a laminate) and drives the formation of periodic wavy-patterns; and (ii) the inclusions rearrange vertically to 'relax' the increasing magnetic forces as they are frustrated horizontally with an increasing strain. Controlled by the particle magnetization (for a given initial geometric configuration), the composites can develop mechanical, magnetic, or transition patterns governed by the complex interplay of the mechanical and magnetic mechanisms.

4.4.2.1 Pattern matching coefficients

We quantify the contribution of these mechanisms at different magnetization values by probing into the corresponding buckling patterns. In particular, we define pattern matching coefficients ϕ_{mech} and ϕ_{mag}; they gauge the similarity of an instability pattern with the *ideal* mechanical and magnetic patterns. Here, for the composites with a particular spacing ratio, the buckling pattern obtained using magnetically inactive inclusions is considered to be the standard mechanical pattern (left column in Fig. 4.9), whereas the pattern at $M = 1000$ kA/m represents the ideal magnetic pattern (right column in Fig. 4.9). First, we present the method employed to evaluate the pattern matching coefficients ϕ_{mech} and ϕ_{mag}. The method is illustrated

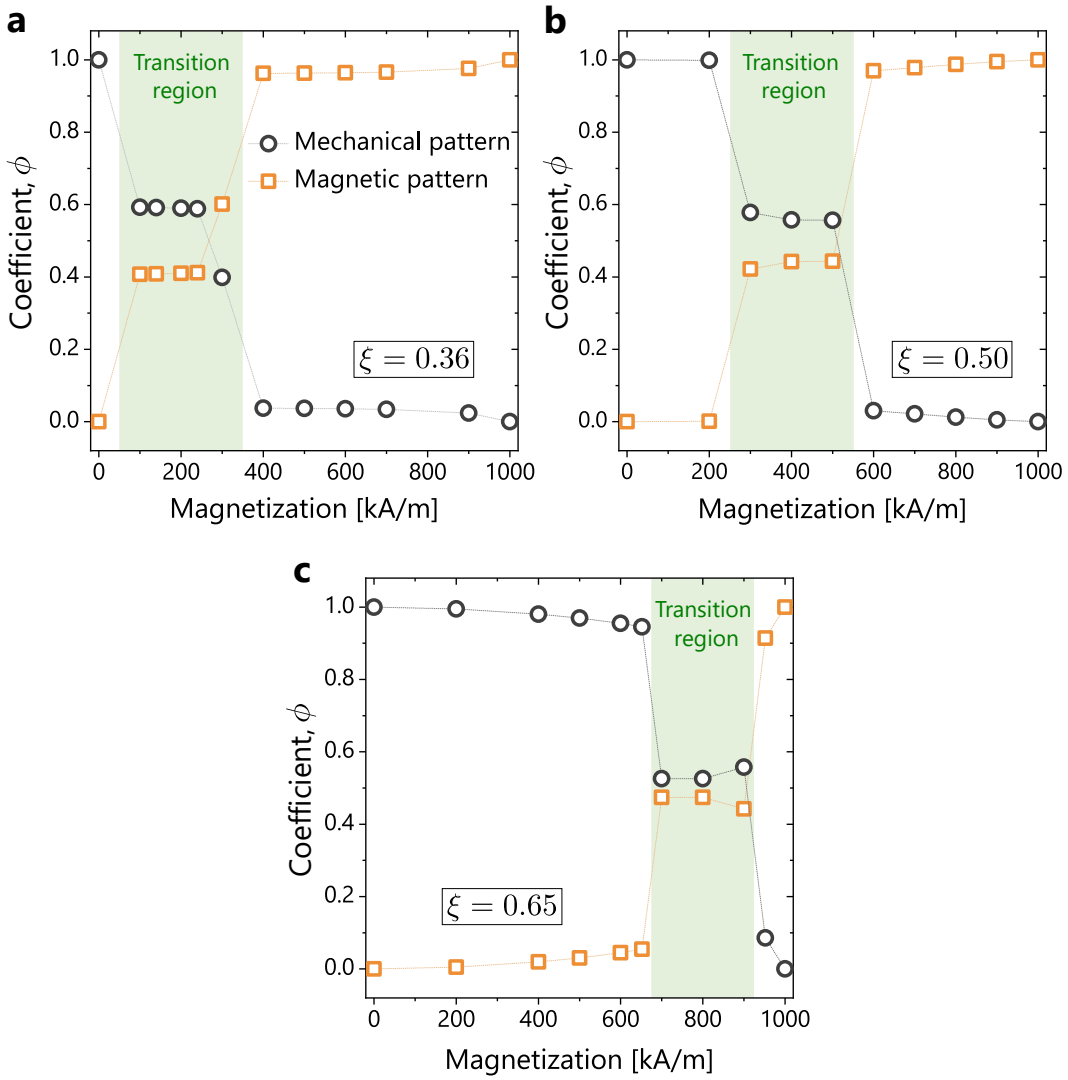

Figure 4.10: Pattern matching coefficients ϕ_{mech} and ϕ_{mag} versus the magnetization strength for the composites with spacing ratios: **a**, $\xi = 0.36$, **b**, $\xi = 0.50$, and **c**, $\xi = 0.65$.

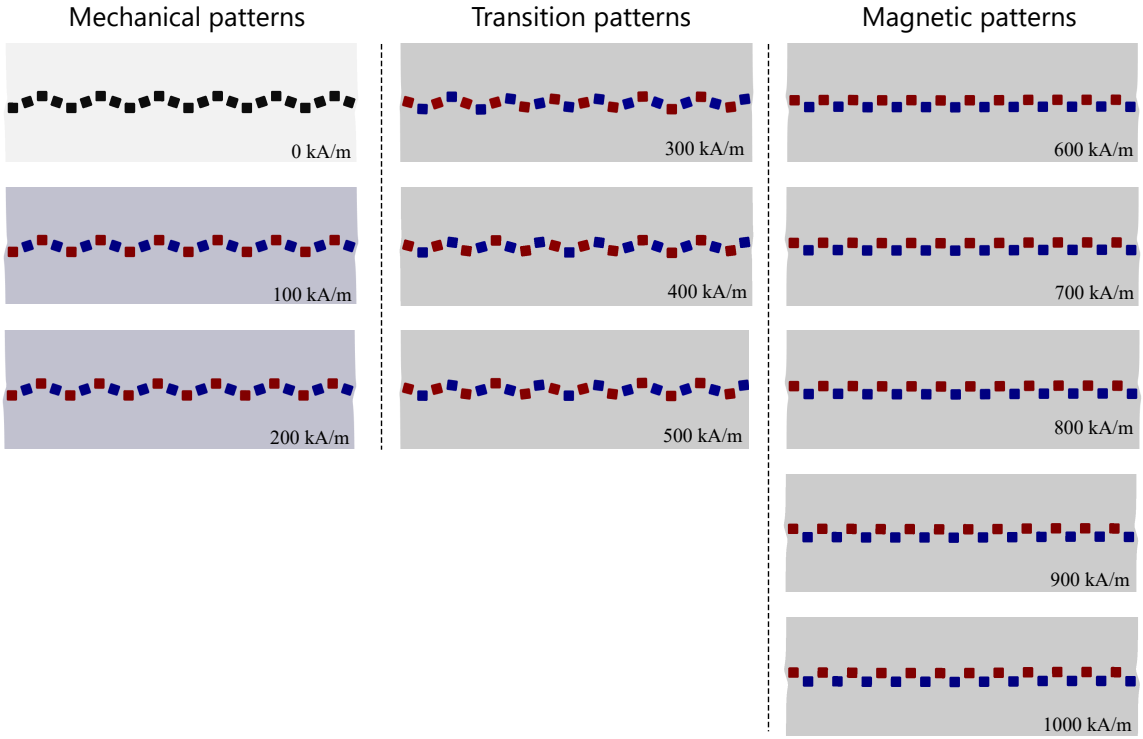

Figure 4.11: Buckling patterns at various magnetization values in composites with $\xi = 0.5$. The magnetization values are written at the bottom-right of each image.

using the example of composites with $\xi = 0.5$. The corresponding buckling patterns at different magnetic strengths, as shown in Fig. 4.11, are classified into mechanical, transition, and magnetic patterns.

The coefficients are evaluated as follows. First, the vertical position of inclusions is recorded and normalized such that the bottom-most inclusion is situated at zero and the top-most at one (see Fig. 4.12a). For the composites with $\xi = 0.5$, the position of inclusions is noted at the compressive strain of $\varepsilon = 0.30$. The normalization of data allows us to eliminate the effect of amplitude. Consider, for example, the pattern at $M = 400$ kA/m (shown in green color in Fig. 4.12a). To evaluate the pattern matching coefficients at $M = 400$ kA/m, we compute the difference between the vertical positions

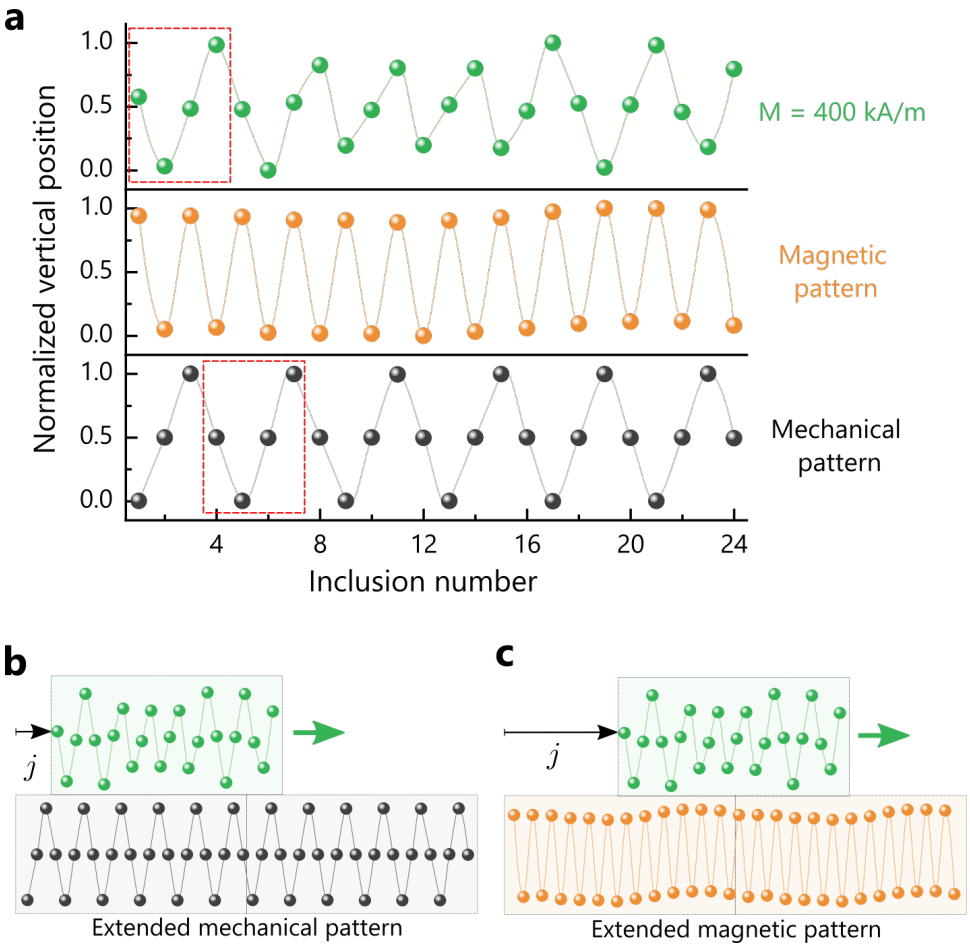

Figure 4.12: **a**, Normalized vertical positions of the inclusions corresponding to the $M = 400$ kA/m, ideal magnetic, and ideal mechanical buckling patterns. Shifting of $M = 400$ kA/m pattern over the extended (**b**) mechanical and (**c**) magnetic patterns to compute the differences.

of inclusions in the corresponding buckling pattern and the ideal patterns. Let us denote the vertical position of inclusions in this pattern using $\mathbf{v}_{400}$, and those of ideal patterns as $\mathbf{v}_{mech}$ and $\mathbf{v}_{mag}$. These vectors are of the size 24×1 with each element containing the vertical position of the inclusions (there are 24 inclusions). The difference with the ideal mechanical pattern is defined as $\delta_{mech} = \sum_{i=1}^{24} \left(v_{400}(i) - v_{mech}(i)\right)^2$. Similarly, the difference with ideal magnetic pattern is $\delta_{mag} = \sum_{i=1}^{24} \left(v_{400}(i) - v_{mag}(i)\right)^2$. From these differences, we can quantify the similarity between two patterns – lower the difference, higher the similarity.

We note that the features of the patterns can be present at different inclusion locations in two different composites. For example, consider the first four inclusions in the $M = 400$ kA/m buckling pattern. They resemble the periodic arrangement in the mechanical pattern (highlighted by red-dashed rectangle). In the ideal mechanical pattern, however, the similar arrangement is formed by the inclusion placed at positions four to eight (highlighted by red-dashed rectangle). Therefore, computing the δ_{mech} directly will result in a higher difference, indicating a very low similarity between the two patterns, which otherwise are comparatively more alike.

To avoid such miscalculations, we compute the minimum of the differences between the patterns by shifting the buckling pattern over the extended ideal patterns. In particular, we extend the ideal patterns by repeating them, i.e., $\mathbf{V}_{mech} = [\mathbf{v}_{mech}, \mathbf{v}_{mech}]$ and $\mathbf{V}_{mag} = [\mathbf{v}_{mag}, \mathbf{v}_{mag}]$. Then, we iteratively compute the differences by shifting the buckling pattern. The shifting of $M = 400$ kA/m buckling pattern over the extended ideal patterns is shown in Fig. 4.12b and c. The number of inclusions by which the pattern is shifted towards right from the zeroth position is represented using integer j (see Fig. 4.12b and c). At a position j of the pattern $\mathbf{v}_{400}$, difference with the mechanical pattern is defined as

$$\delta_{mech}(j) = \sum_{i=1}^{24} \left(v_{400}(i) - V_{mech}(i+j)\right)^2, \tag{4.2}$$

where $j \in [0, 23]$. Similarly, the difference with the magnetic pattern is computed using $\mathbf{V}_{mag}$. From the differences thus computed, we calculate the minimum differences as $\Delta_{mech} = \min_j(\delta_{mech}(j))$ and $\Delta_{mag} = \min_j(\delta_{mag}(j))$. Finally, we calculate the pattern matching coefficients using Δ_{mech} and Δ_{mag} as

$$\phi_{mech} = \frac{\Delta_{mag}}{\Delta_{mech} + \Delta_{mag}} \quad \text{and} \quad \phi_{mag} = \frac{\Delta_{mech}}{\Delta_{mech} + \Delta_{mag}}. \tag{4.3}$$

Note that the coefficients ϕ_{mech} and ϕ_{mag} varies between zero and one and also sum up to one.

Figure 4.10 shows the variations of mechanical, ϕ_{mech} (black circular symbols) and magnetic, ϕ_{mag} (orange square symbols) coefficients as functions of the magnetization level in the composites with spacing ratios $\xi = 0.36$ (a), $\xi = 0.50$ (b), and $\xi = 0.65$ (c). The plots explicitly show that the magnetic strength of inclusions can be partitioned into three groups, based on the values of ϕ_{mech} and ϕ_{mag}. First, in the composites with low magnetization strength, the buckling patterns have a large mechanical pattern coefficient, $\phi_{mech} > 0.9$ (or $\phi_{mag} < 0.1$). At higher magnetization levels, however, $\phi_{mag} > 0.9$ (or $\phi_{mech} < 0.1$). For example, consider the composites with $\xi = 0.50$ (Fig. 4.10b): the first region is observed for magnetization $M \lesssim 250$ kA/m, where they develop mechanical patterns (as shown in the center row of right column in Fig. 4.9). For $M \gtrsim 550$ kA/m, the inclusions rearrange to develop the two-level magnetic buckling pattern (right column in Fig. 4.9).

The buckling pattern does not switch from mechanical to magnetic with an increase in the magnetic strength. Instead, there exists a range of magnetization values where the buckling patterns are distinctly different from both the mechanical and magnetic ones; we refer to this range as *transition region* (shaded in green color). In this region, the mechanical and magnetic pattern coefficient values are close to each other, ranging within $0.4 \lesssim (\phi_{mech} \text{ and } \phi_{mag}) \gtrsim 0.6$. This highlights a competition between the two mechanisms leading to the cooperative mechano-magnetic patterns. Note

that the coefficients ϕ_{mag} do not increase monotonically and gradually with an increase in magnetization. In the considered examples (Fig. 4.10), the coefficients change abruptly from the $\phi_{mag} < 0.1$ to $0.4 \lesssim \phi_{mag} \gtrsim 0.6$ range as we enter the transition region; and it again drastically jumps to $\phi_{mag} > 0.9$ in the magnetically-dominated region. Moreover, in the transition region, the coefficients either form a plateau or change abruptly. For example, in the composite with $\xi = 0.36$, $\phi_{mag} \approx 0.409$ for $M = 100$ to 240 kA/m and it increases to $\phi_{mag} = 0.601$ at $M = 300$ kA/m (see Fig. 4.10a). Additionally, we note an unexpected decrease in ϕ_{mag} at $M = 900$ kA/m in the composite with $\xi = 0.65$ (see Fig. 4.10b). These findings shed light on the influence of particulate composite's geometry on the pattern formations in the post-buckling regime. In particular, the discrete system of inclusions can only rearrange into certain stable patterns to reduce geometric frustrations – giving rise to jumps in pattern matching coefficients.

We note that the transition region shifts to higher magnetization values with an increase in the spacing ratio. For example, in the composites with $\xi = 0.36$, the region lies approximately between $50 \gtrsim M \lesssim 350$ kA/m, which shifts to $675 \gtrsim M \lesssim 925$ kA/m at $\xi = 0.65$. This shift implies that it is comparatively easier to achieve two-level magnetic buckling patterns in a composite with far-placed inclusions, even when they are magnetically weak. However, when the inclusion are initially closely-placed, the mechanical behavior dominates the formation of the post-buckling patterns.

Next, we analyze the dependence of instability onset on the magnetic strength of inclusions. In Fig. 4.13, we plot the critical strain ε_{cr} for composites with $\xi = 0.36$ (red squares), $\xi = 0.50$ (green circles), and $\xi = 0.65$ (blue triangles) as the functions of magnetization. We observe that the composites develops instability at smaller strain levels (or ε_{cr} decreases) with an increase in magnetization. This destabilizing behavior is caused by the repulsive forces between the adjacent inclusions, leading to earlier onset of instabilities (also observed in experiments, see Fig. 4.1c). We note that,

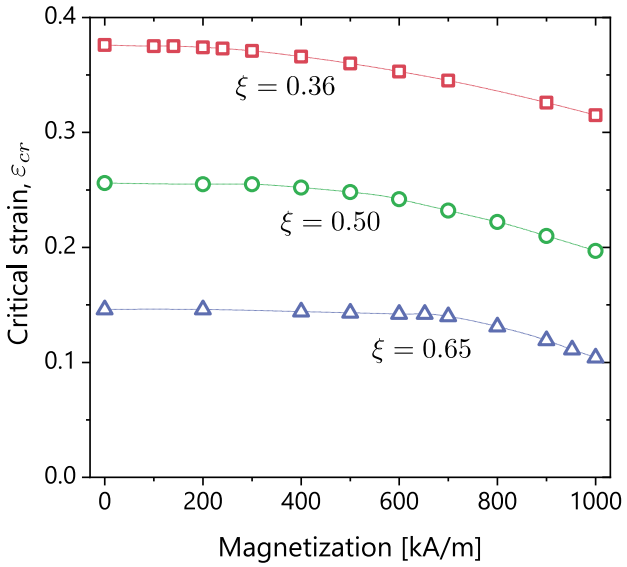

Figure 4.13: Dependence of critical strain ε_{cr} on the magnetization of inclusions.

unlike the sudden transitions observed in the buckling patterns, ε_{cr} shows a gradual and monotonic decrease with an increase in magnetic strength. Moreover, the rate of change in ε_{cr} is higher at larger magnetization values, shedding light on the non-linear relation between the magnetic forces and magnetization.

4.4.3 Programming buckling patterns and encoding information

Hitherto, we have investigated the pattern formations in composites possessing the same magnetic polarity arrangement – the adjacent inclusions repel each other. Next, we examine two distinct arrangements of magnetization orientations. The first polarity pattern is *periodic*, consisting of a repeating set of three inclusions with one negative magnetic polarity followed by two positives. The second one is an arbitrarily-chosen *aperiodic* polarity pattern.

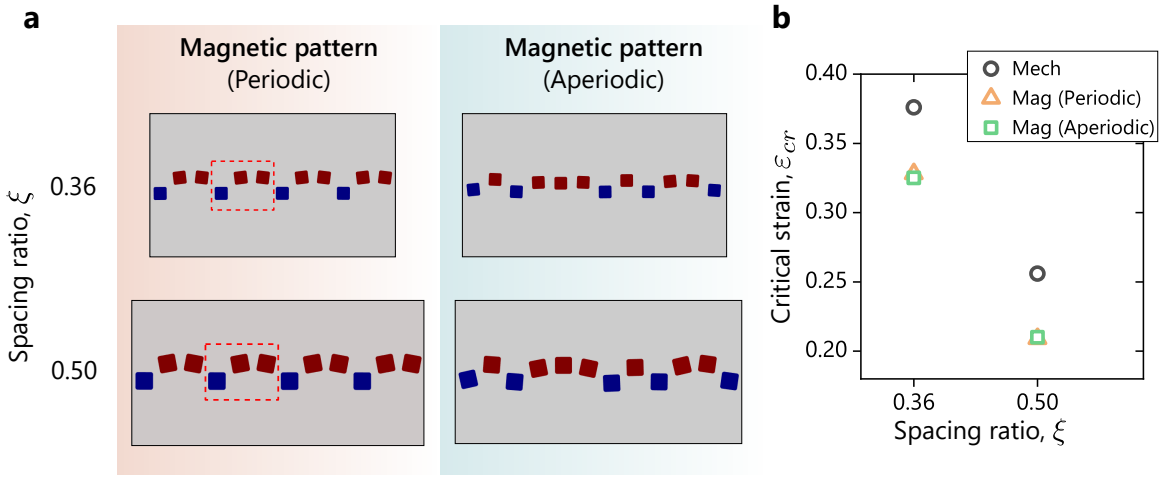

Figure 4.14: **Periodic and aperiodic reconfigurations. a**, Simulation images of particulate composites with spacing ratio $\xi = 0.36$ (top) and $\xi = 0.5$ (bottom). The results are shown for magnetic composites with periodic polarity pattern (left column) and aperiodic polarity pattern (right column) having magnetization $M = 900$ kA/m. **b**, Critical strain values for the composites considered in sub-figure a and their mechanical counterparts.

We consider the inclusions with sufficiently high magnetic strength, i.e., $M = 900$ kA/m, such that the formation of buckling patterns is dictated by the magnetic interactions. Figure 4.14 presents the numerical results for the instability development in these composites.

In magnetic composites with periodic polarity pattern, the magnets with negative polarity are surrounded by the pairs of positively polarized inclusions; hence, they are repelled by these pairs and vice-versa. On the other hand, among the inclusion pair with positive polarity, there is an attraction force. Guided by these magnetic interactions, in the buckling pattern, the negatively polarized magnets shift to form one row. All the positively polarized magnets rearrange in pairs to form the other row. Notably, identical buckling patterns are obtained in both the composites, regardless of their spacing ratios (deformation images are shown in the left column of Fig. 4.14a). Although the periodicity of these magnetic patterns is $N = 3$

(repeating periodic elements are bounded by red-dashed rectangles), the arrangement of inclusions is noticeably different from that in mechanical composite with $\xi = 0.36$ (shown in the left column of Fig. 4.9). In particular, the magnetic pattern is a discrete two-level reconfiguration of inclusions, whereas the mechanical one is inherently a wave-like arrangement. We find that in the case of an aperiodic polarity pattern as well, the instability-induced shift in inclusions is governed by the resulting magnetic interactions. Consequently, the aperiodic buckling pattern emerges in the magnetic composites (Fig. 4.14a, right column), which is otherwise inadmissible in the mechanical composite. Furthermore, for both the magnetic patterns – periodic and aperiodic – the critical strain values are lower than their mechanical counterparts (Fig. 4.14b).

From the analysis thus far, two key features emanate from the magnetic buckling patterns. First, they are strictly guided by the (attraction/repulsion) magnetic forces between the inclusions, which leads to the formation of two-level microstructure patterns with inclusions of identical polarity lying in the same row. Second, these transformations are independent of the initial spacing ratio, ξ. Building upon these features, we can program any desired and deformation-activated microstructural transformations in the composite. In particular, the target two-level pattern can be achieved by encoding the magnetic bit scheme into the design of initially periodic composite. The magnetic bit scheme consists of pattern bits '0' and '1', physically denoting the two opposite orientations of magnets (Fig. 4.15a). The placement of bits in the scheme is planned according to the target microstructure pattern.

To showcase the complexity of achievable shapes, we consider the example of encoding the 'UW' pattern into the composite (Fig. 4.15b). The pattern is dissected into two-levels, such that it can be discretely represented by the arrangement of inclusions. Guided by the required positioning of the inclusions in the post-buckled state, we assign the magnetic pattern bits

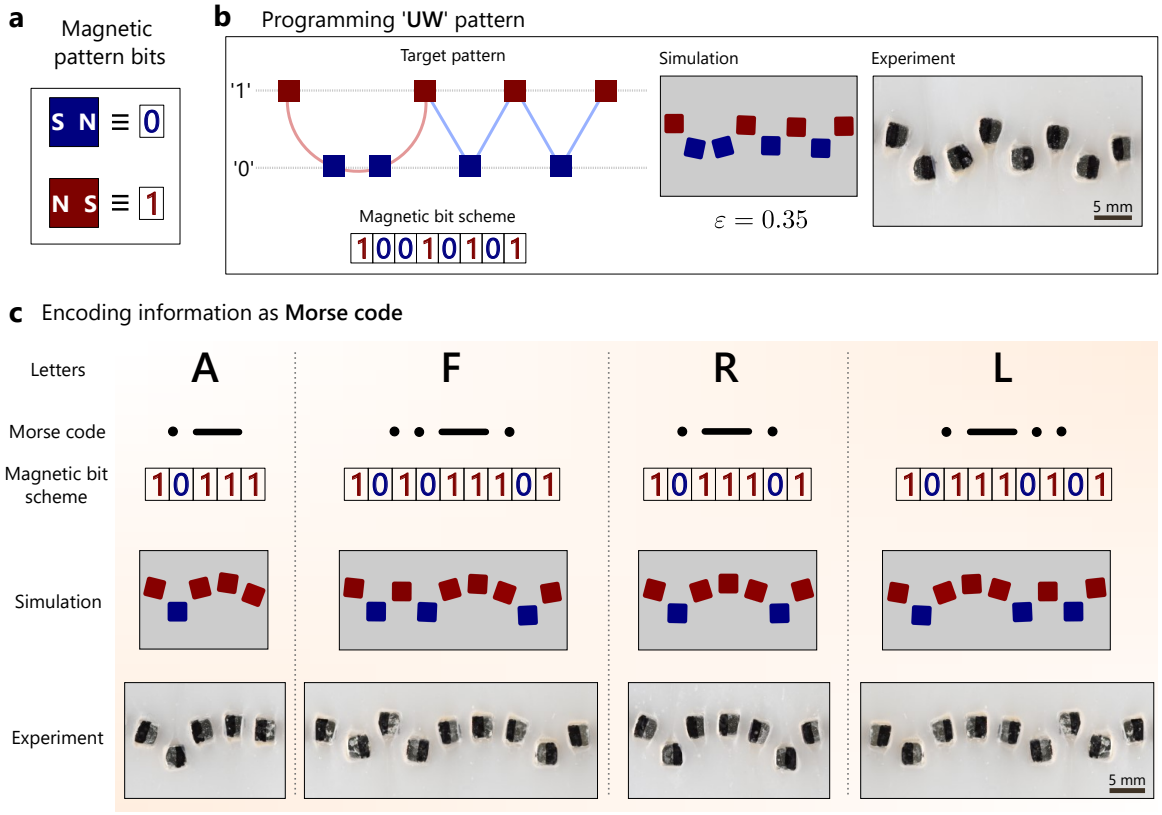

Figure 4.15: **Programming instability patterns and encoding information.** **a**, Physical definition of the magnetic pattern bits that constitutes the magnetic bit scheme. **b**, Programming 'UW' pattern. Discretization of 'UW' pattern into two levels and the analogous bit scheme. The corresponding simulation and experimental images are shown on the right. **c**, Encoding information as Morse code. From top to bottom: the letters, their Morse code, magnetic bit schemes, the simulation results, and the experimental deformation images. The results are shown for the composites with spacing ratio $\xi = 0.5$ subjected to a compressive strain of $\varepsilon = 0.35$.

to each inclusion: zero for bottom row and one for top row. The magnetic bit scheme for the 'UW' pattern is obtained as '10010101'. We assess this scheme in an initially periodic particulate composite with spacing ratio $\xi = 0.5$. In the composite, the magnetic inclusions are embedded with polarity pattern that follows the aforementioned magnetic bit scheme. Under compressive strain greater than the critical value, the inclusions depart from their initial periodic arrangement and indeed reconfigure to form the target 'UW' pattern. The experimental and simulation deformation images are shown at the strain-level $\varepsilon = 0.35$ in Fig. 4.15b.

Finally, we present the encoding of binary information, specifically, Morse code in our architected material, and analyze the consequent instability-induced transformations. Morse code is a method to encode text in the form of dots and dashes. In terms of ON-OFF keying, in a single letter, a dot represents one ON signal, whereas a dash denotes a series of three ON signals. The space in the Morse code is the equivalent of one OFF. To encode Morse code in our composites, we represent ON and OFF signals as '1' and '0', respectively.

As illustrative examples, we encode the Morse code of four letters, 'A', 'F', 'R', and 'L'. The magnetic bit scheme, that is fed into the design of the composite, is directly derived from the Morse code in the binary form (as shown in the 'Bit scheme' row in Fig. 4.15c). Each letter give rise to distinct deformation modes in the post-instability regime. In particular, following the input polarity arrangement, the inclusions rearrange into distinct binary patterns. These patterns are identically revealed by our experiments and finite element simulations (the bottom two rows in Fig. 4.15c show the deformation images at strain $\varepsilon = 0.35$). The stored binary information can be decoded from the relative positioning of the inclusions. Therefore, in the present system, the information can be encoded in the magnetic form and read out via the applied mechanical deformation in the form of buckling patterns.

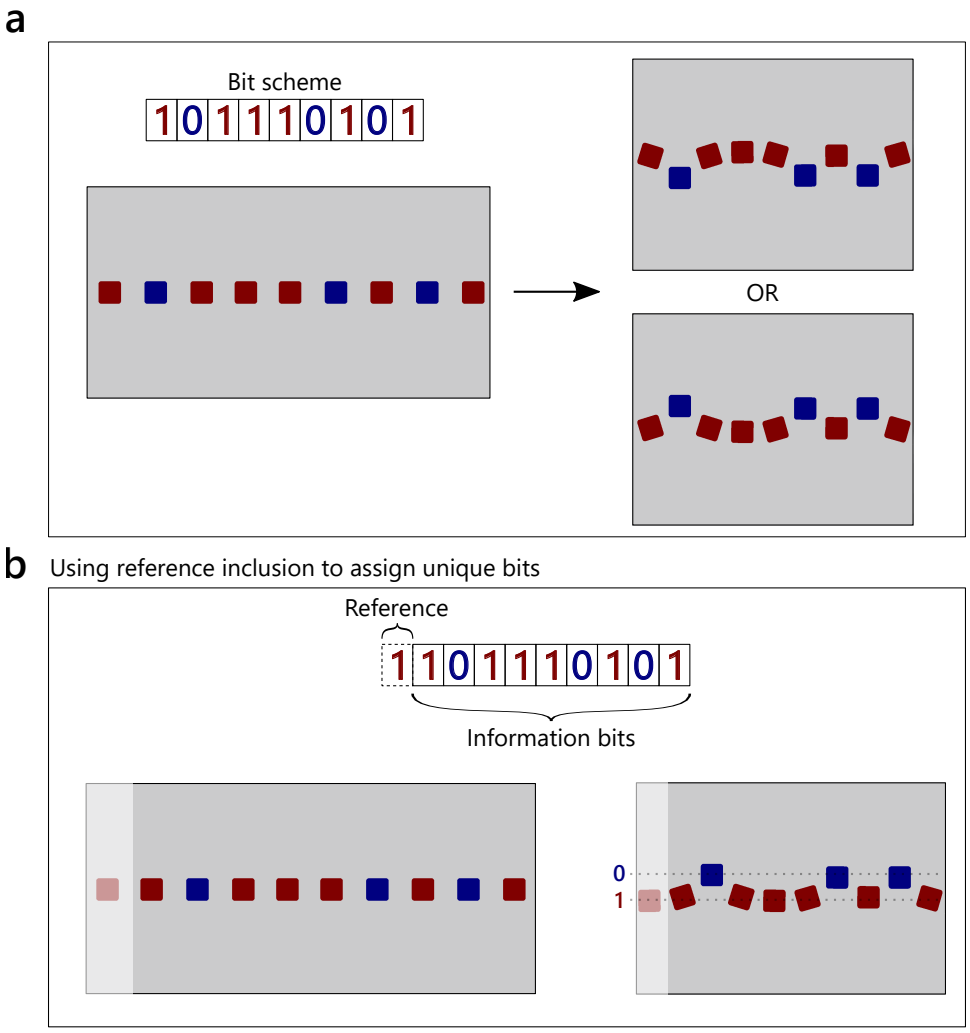

Figure 4.16: **Unique bits assignment. a**, Two possible instability-induced reconfigurations of inclusions for magnetic composite with polarity pattern of Morse code letter 'L'. **b**, Addition of reference inclusion to identify unique information bits from the buckling pattern.

4.4.3.1 Unique bits assignment

The magnetic bit placement scheme for guiding reconfigurations may not always result in the buckling patterns with negative polarity inclusions

constituting the bottom row. In an ideal setting, there is an equal probability that the negative polarity magnets form the top row and the ones with positive polarity form the bottom row. For example, consider encoding the Morse code of letter 'L' into the composite; the corresponding bit scheme is '101110101'. The particulate composite encoded with this scheme, can develop one of the two buckling patterns with equal probability, as shown in Fig. 4.16a. Therefore, bits '0' or '1' cannot be uniquely determined from the position of the inclusion in a buckling pattern.

This issue can be resolved by using an extra inclusion as reference, following the approach similar to setting a ground-level bit in electrical signals. For example, in addition to the inclusions that carry the information, an extra inclusion with positive polarity is added (Fig. 4.16b). Hence, in the buckling pattern, the inclusions aligning in the same row as the reference inclusion carry the '1' information bit, whereas the inclusions forming the other row has '0' bit. By using this method, the information bits can be assigned uniquely based on the reference inclusion's configuration, regardless of the top/bottom position of the inclusions (as shown in Fig. 4.16b).

Finally, we note that the presence of initial geometric or material defects can potentially affect the buckling patterns. The extent of perturbations, however, can be reduced by producing magnetic composites through various additive manufacturing techniques across length scales (Kim et al., 2018; Zhang et al., 2021d; Cao et al., 2021; Wang et al., 2022b; Lantean et al., 2019; Sundaram et al., 2019; Wu et al., 2020; Dong et al., 2020; Lopez-Donaire et al., 2023; Lu et al., 2017). Additionally, employment of these techniques to fabricate the magneto-elastic materials can automate and simplify the manufacturing process. On the other hand, these imperfections can be capitalized to enrich the admissible range of buckling patterns (Liu et al., 2017).

5 MAGNETO-MECHANICAL METAMATERIAL WITH TUNABLE VIBRATION-ISOLATION

5.1 Introduction

Controlling the propagation of mechanical signal through elastic waves is essential for a large variety of applications such as non-invasive material testing, waveguides, and medical imaging. Recently, the acoustic metamaterials have gained significant attention, since they exhibit exotic wave phenomena. Elastic metamaterials (Liu et al., 2000; Mazzotti et al., 2023; Chen et al., 2023a; Peri et al., 2020; Wootton et al., 2019) draw their performance from pecuilar microstructures (De Maio et al., 2023; Aguzzi et al., 2022; Matlack et al., 2018; Turco et al., 2022), giving rise to topological phase transitions, extreme (and negative) effective parameters, and the bandgap (BG) phenomenon. The potential metamaterial applications range from vibration isolation (Elser et al., 2006; Liu et al., 2019; Zhang et al., 2021c, 2018; Kushwaha et al., 1993; Krushynska et al., 2021a; D'Alessandro et al., 2020; Colquitt et al., 2017), switching (Bilal et al., 2017a), waveguiding (Zhu et al., 2014; Wang et al., 2016; Bilal et al., 2017b; Krushynska et al., 2021b; Miniaci and Pal, 2021; Gei et al., 2020) and focusing (Memoli et al., 2017), mode splitting (Chang et al., 2015; Galich and Rudykh, 2015), cloaking (Zhang et al., 2011), negative phase and group velocities (Lee et al., 2010; Fang et al., 2006; Lott et al., 2021), and attaining topological state of matter that enables elastic wave flows immune to backscattering losses (Wang et al., 2015; Foehr et al., 2018; Braverman et al., 2021; Chen et al., 2019; Zhang et al., 2020).

Soft architected materials, in particular, due to their capability to sustatin large elastic (reversible) deformations, open the possibility of manipulating wave propagation through deformation (Slesarenko et al., 2018; Dorfmann

and Ogden, 2010; Galich and Rudykh, 2016; Chang et al., 2015; Galich and Rudykh, 2015; Arora et al., 2021, 2022; Li et al., 2023a; Wang et al., 2021). Deformation of soft materials can influence the wave propagation in two ways: (i) The microstructure of the material will evolve, as it material undergoes large deformation; (ii) the presence of deformation-induced stresses can influence wave propagation. Moreover, soft architected materials can develop sudden structural transformations that are induced by the development of elastic instabilities within the material. Due to the switch in the structure of the material, it also exhibits a change in its acoustic properties (Li et al., 2018b; Wang et al., 2014, 2020; Rudykh and Boyce, 2014; Bertoldi and Boyce, 2008b; Gao et al., 2021; Pranno et al., 2022). However, as also discussed in Chapter 4, the geometry of admissible instability-driven pattern transformations is highly limited in this mechanics-centric design approach and, in general, the patterns are spatially homogeneous and periodic (Kang et al., 2014; Frenzel et al., 2016; Mullin et al., 2007; Triantafyllidis and Maker, 1985; Li et al., 2019a; Jiang et al., 2006; Li et al., 2022, 2021). Here, we address this challenge by attaining non-affine (local) programmability of the amplitude of buckling patterns.

In this work, we propose a design of magneto-mechanical metamaterial that offers tunable frequency filtering. Our strategy make use of the programmed non-uniform deformation in the materials, which is induced by the instability development in a graded architected design and the magnetic interaction between the inclusions. Through our simulations, we show the induction of new bandgaps via applied deformation. Moreover, we uncover the underlying physical mechanisms leading to the transformation in the acoustic behavior of the metamaterial.

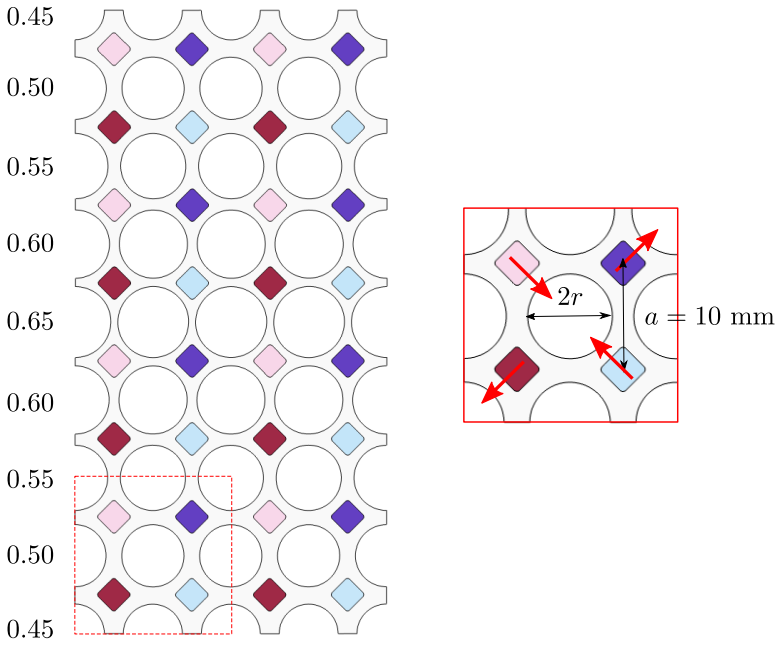

Figure 5.1: Schematic of the magneto-mechanical metamaterial. The volume fraction of voids in a row is written on the left. The red-dashed rectangle marks the unit cell of a particular row; enlarged view of the unit cell shown on the right. The arrows in the enlarged view show the direction of magnetization polarity.

5.2 Metamaterial design

Figure 5.1 shows the schematic of the magneto-mechanical metamaterial. The design consists of circular voids distributed in square arrangement in the soft matrix. The square magnets are also placed in a square arrangement at a distance of $a = 10$ mm between their centers (horizontal and vertical), as shown in Fig. 5.1 enlarged view. The size of the circular voids is defined using their volume fraction $c_v = \pi r^2/a^2$, where a is the distance between the adjacent magnets and r is the radius of the circular voids. In this study, we consider a graded geometry where the size of voids increase from top to center and decreases from center to bottom row. As shown in Fig. 5.1, the

volume fraction of voids increases from $c_v = 0.45$ in the top row to $c_v = 0.65$ in the center row, and gradually decreases to $c_v = 0.45$ in the bottom row.

The magnets are placed at an angle of 45° from the horizontal axis. The side length of square magnets is $d = 3.175$ mm. The magnets have four different orientations of magnetization as shown in the enlarged view in Fig. 5.1 using the red arrows. This polarity arrangement is periodically repeated in the entire specimen.

5.3 Modeling

In our simulations, the soft matrix is modeled as nearly incompressible neo-Hookean hyperelastic material with the strain energy density function given in Eq. (3.4). The matrix material characterized by the initial shear modulus $G_m = 0.1$ MPa and material density $\rho_m = 1090$ kg/m^3. The stiff inclusions are modeled as a rigid material with the material density of $\rho_i = 6250$ kg/m^3.

The soft matrix is considered to be magnetically inactive and does not have any remnant magnetization. The magnetic inclusions are modeled as hard-magnetic materials with residual magnetic flux density defined in terms of the magnetization $M = 900$ kA/m (same as B422, K&J magnetics, used in Chapter 4).

5.3.1 Static compression study

The metamaterial is subjected to in-plane deformation, with compression along the vertical direction. In the simulations, the macroscopic mechanical loading is implemented by applying periodic boundary conditions. The applied macroscopic deformation gradient is

$$\bar{\mathbf{F}} = \bar{F}_{11}\mathbf{e}_1 \otimes \mathbf{e}_1 + (1-\varepsilon)\mathbf{e}_2 \otimes \mathbf{e}_2 + \mathbf{e}_3 \otimes \mathbf{e}_3 \tag{5.1}$$

where ε is the compressive strain and $\bar{F}_{11}$ is evaluated using the traction-free left and right boundaries. To avoid rigid body motions, the displacement of the bottom-left point is constrained. We assume that there are no surface and free currents within our system and the specimen is subjected to quasi-static mechanical compression. The resulting governing equations Eq. (1.1) and (1.11) are evaluated by means of finite element code COMSOL Multiphysics 6.0.

To capture the post-buckling behavior, we consider slightly perturbed shape of voids. In particular, we impose the imperfection by using elliptic voids with very small aspect ratio 1.001:1, instead of circular voids. It was verified that the geometrical imperfection do not affect the predicted critical strain values or the instability-induced patterns.

5.3.2 Vibration study

In this study, we investigate the propagation of pressure waves traveling from top to bottom in the magneto-mechanical metamaterial. We perform the frequency domain analysis on the finitely deformed state (obtained from the static compression study, Sec. 5.3.1) to evluate the transmittance spectrum. To perform the analysis, we apply periodic boundary conditions on the right and left boundaries. On the pre-deformed metamaterial, a harmonic perturbation is imposed on the top boundary with an amplitude A_{in}. The induced harmonic response at the bottom boundary is captured, and the transmittance spectrum is computed as the ratio between the output and input displacements, defined as $20 \log_{10} ||A_{out}(\omega)/A_{in}||$, where ω is the frequency.

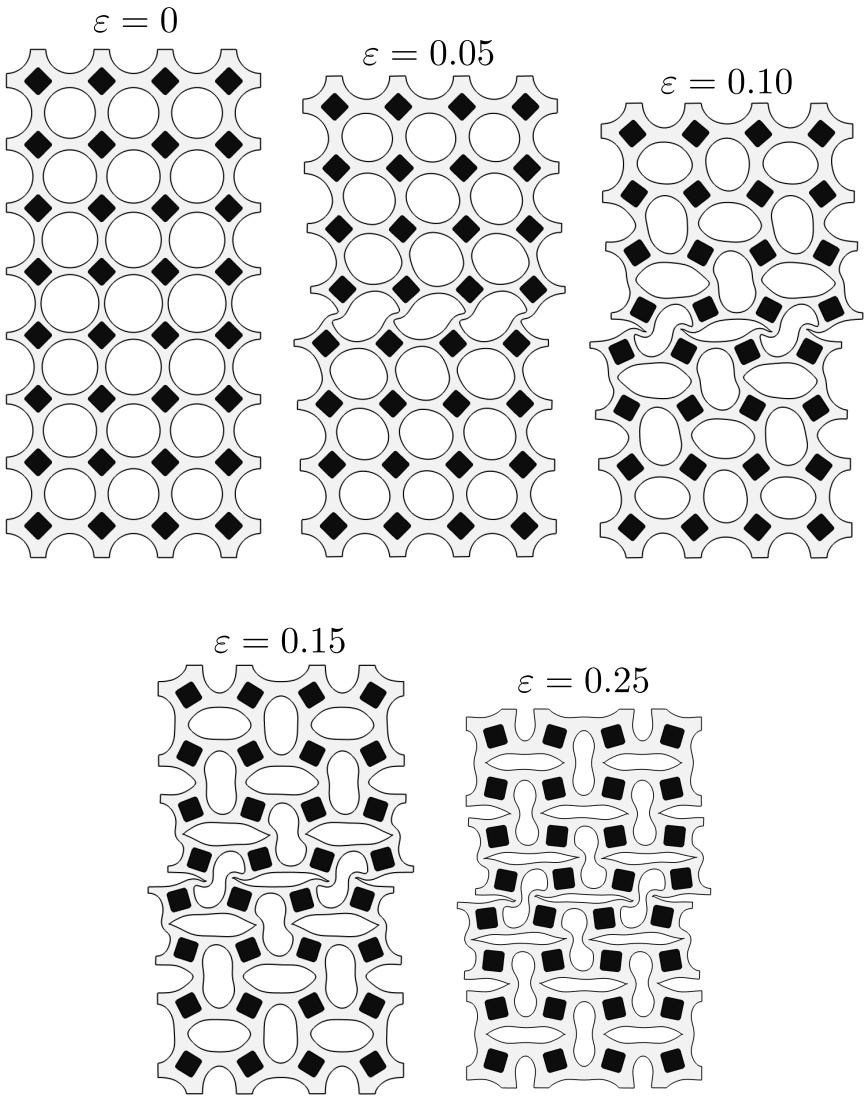

Figure 5.2: Simulation images showing the evolution of mechanical metamaterial's structure with compression.

5.4 Results

5.4.1 Static behavior and instability development

We start with analyzing the response of the *purely-mechanical* metamaterial. In particular, we consider the architected material shown in Fig. 5.1 with

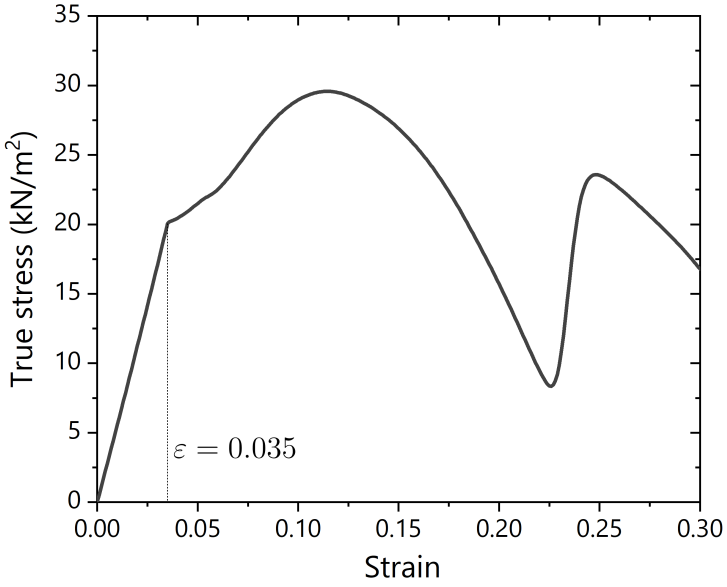

Figure 5.3: True stress vs applied strain for the mechanical metamaterial.

non-magnetic rigid inclusions. Figure 5.2 shows the evolution of the metamaterial's structure with increase in compressive strain. The rigid inclusions are shown in black color, whereas the matrix is of gray color.

We observe that at strain $\varepsilon = 0.05$, the voids in the central row with maximum volume fraction of $c_v = 0.65$ departs from their initial circular shape. At this deformation level, however, the change in the shape of other voids with $c_v \leq 0.60$ is relatively insignificant. This is the primary instability-mode that develops in the central row, because of which the material architecture is divided into two-halves: upper half and bottom half. These two halves appear to be sliding horizontally with respect to each other, with the increase in deformation (compare the deformation image at $\varepsilon = 0.05$ and $\varepsilon = 0.10$ in Fig. 5.2).

At strain level, $\varepsilon = 0.10$, we find that the voids in the top and bottom halves also develop the secondary instability-mode. In particular, they develop the well-known transformation of voids from circular to elliptical shapes

with alternating orientations; the similar shape morphing is also observed in soft matrix having identical circular voids with square arrangement (Mullin et al., 2007; Bertoldi et al., 2008). With the increase in compressive strain further, the voids collapse and their effective area decreases. This leads to a significant shrinkage in the size of the architected material and it exhibit auxetic behavior. The occurence of auxetic behavior in the post-instability regime has also been reported in other soft architected materials (Bertoldi et al., 2010; Li et al., 2018b).

Figure 5.3 shows the true stress (kN/m^2) at the top boundary as the function of applied strain for the mechanical metamaterial. At smaller strain levels, we find that the stress is a linear function of the strain ε. However, for strain levels $\varepsilon > 0.035$, stress-strain curve has a highly non-linear relation. Interestingly, this shift in the stress-strain relation is marked by the development of primary instability. In particular, the buckling of the voids in the central row with $c_v = 0.65$ occurs at $\varepsilon = 0.035$.

Next, we investigate how the structure of the magneto-mechanical metamaterial evolves under compression. Figure 5.4 shows the change in microstructure at different strain levels. In particular, we observe in our simulations that the center row of voids collapse at the strain $\varepsilon = 0.064$. On further compression, the row just under the center row collapses at $\varepsilon = 0.124$. We observe the next collapse of voids in the row just above the center row at $\varepsilon = 0.161$. In other words, first the row with volume fraction $c_v = 0.65$ collapses, followed by the $c_v = 0.60$ rows. This collapse is a form of deformation localization, which occurs post-instability in the row with larger voids. The localization is further accentuated by the attractive forces between the magnetic inclusions.

We note that the magneto-mechanical metamaterial has only one instability pattern, i.e., voids transform from circular to elliptical shapes with alternating orientations. However, the extent of buckling is more concentrated in the voids with larger radius. This buckling pattern is significantly

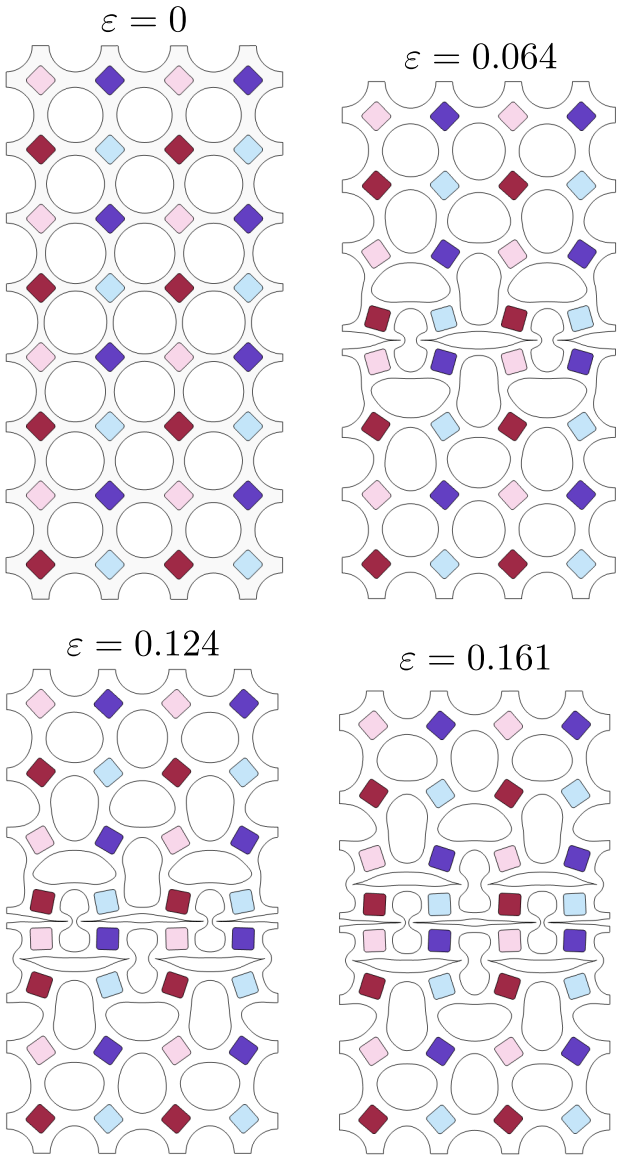

Figure 5.4: Simulation images showing the evolution of magneto-mechanical metamaterial's structure with compression.

distinct from that in purely mechanical case, where there were two modes of instability development (compare the last images in Fig. 5.2 and 5.4). Moreover, we note that the collapse of voids is comparatively more localized in the the magneto-mechanical case.

To further understand this localized deformation, in Fig. 5.5 we plot the compressive true stress as the function of applied strain (red solid curve). The gray-dotted curve for mechanical case is added for comparison. At smaller strain levels (¡1%), the slope of the stress-strain curve is almost identical for both the material systems. However, on further compression, magneto-mechanical system shows a very distinct stress response. Near strain $\varepsilon = 0.064$, when the first collapse takes place, we observe a sharp drop in the force value. The force required at this strain level is negative and slope is zero, which highlights that the metamaterial shows *bistable* behavior. This drop in the force and stabilization at this deformation level is because of the attraction forces between the magnets, which balances the strain energy induced in the matrix. We see similar valleys in the force curve at the second ($\varepsilon = 0.124$) and third collapse ($\varepsilon = 0.161$). Moreover, the maximum stress value is significantly lower as compared to the mechanical case, which is also because of the attraction between the magnets that favors the compression of the material.

5.4.2 Dynamic behavior and strain-tunable transmittance

Next, we study the propagation of elastic waves in the magneto-mechanical metamaterial. Figure 5.6 shows the transmittance spectra, defined as $20 \log_{10} ||A_{out}(\omega)/A_{in}||$, for pressure waves traveling from top to bottom boundary (as described in Sec. 5.3.2). The results are presented for undeformed state, $\varepsilon = 0$ (a), and deformed states at strains: $\varepsilon = 0.064$ (b), $\varepsilon = 0.124$ (c), and $\varepsilon = 0.161$ (d).

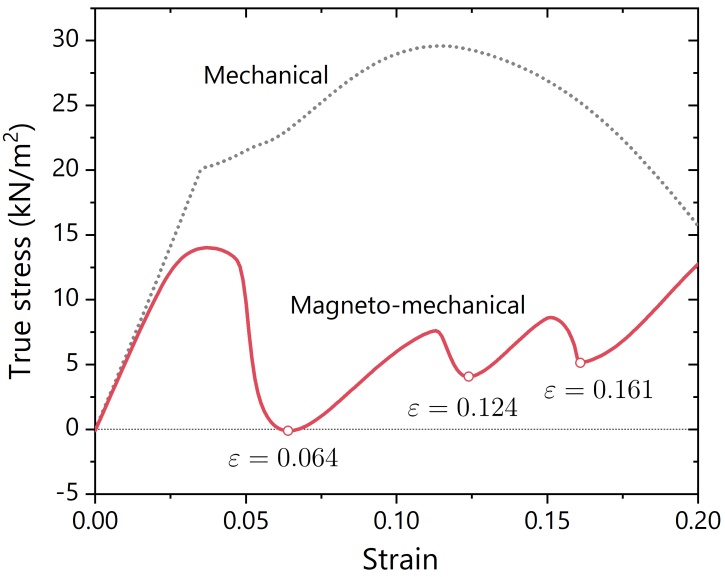

Figure 5.5: True stress vs applied strain for the mechanical metamaterial (gray-dotted curve) and magneto-mechanical metamaterial (red solid curve).

In the undeformed state $\varepsilon = 0$, we observe that the metamaterial has positive transmittance for the almost all the frequency values in the considered range – 1 to 300 Hz (see Fig. 5.6a). This shows that the metamaterial allows the wave of most of the frequencies to pass through. At compression level $\varepsilon = 0.064$, where the center row of void collapses, we observe that the transmittance curve shift below the zero line for a range of frequency at smaller values (approximately 14 to 70 Hz, see Fig. 5.6b).

We find that in the metamaterial with two collapsed rows, at $\varepsilon = 0.124$, the transmittance curve further shifts down giving rise to multiple bandgaps, including the frequency ranges: 14 to 45 Hz, 50 to 130 Hz, 156 to 215 Hz, and 234 to 289 Hz (see Fig. 5.6c). Further, with the third collapse at $\varepsilon = 0.161$, the metamaterial exhibit a highly lossy response, not only at smaller frequencies but also at higher values (see Fig. 5.6d). Note that this drastic change in the acoustic behavior of the metamaterial is achieved only through applied deformation (compare Fig. 5.6a and d). Therefore, it

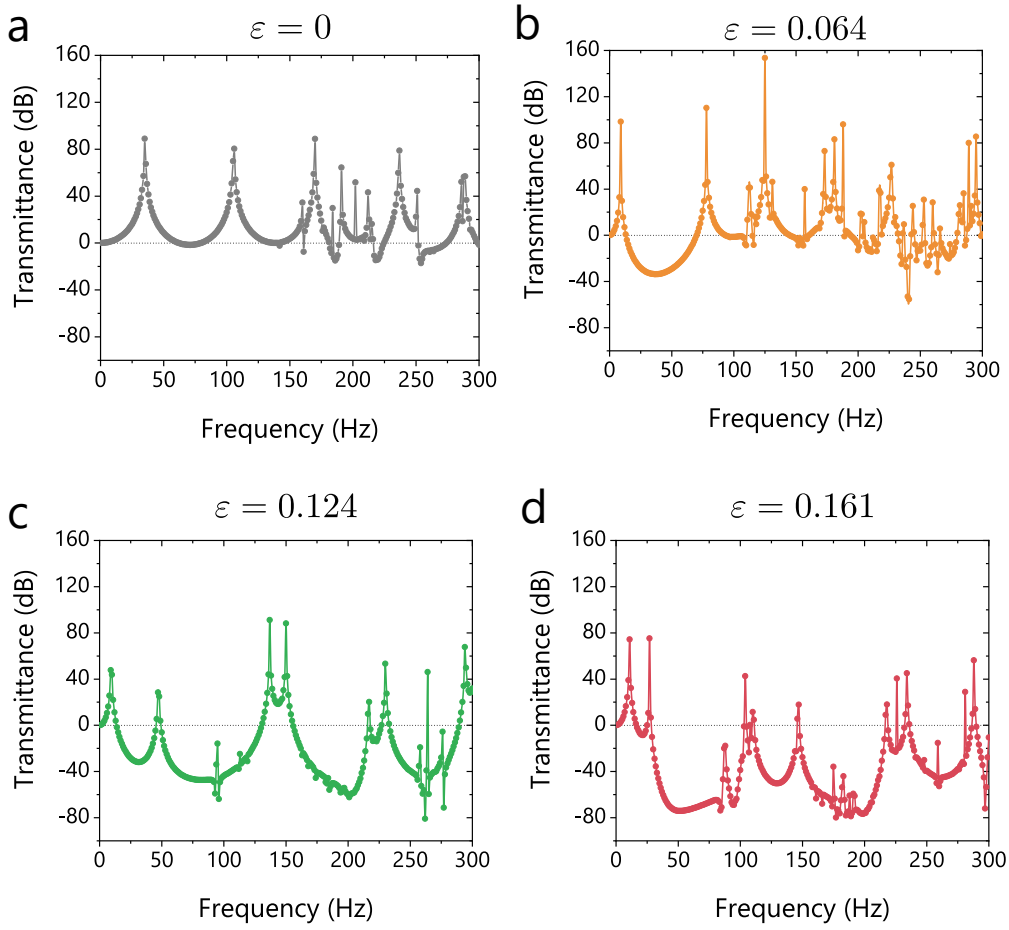

Figure 5.6: Transmittance spectra at strain levels: **a.** $\varepsilon = 0$, **b.** $\varepsilon = 0.064$, **c.** $\varepsilon = 0.124$, and **d.** $\varepsilon = 0.161$.

can be reversed by reinstating the initial microstructure by changing the compression level.

To investigate the mechanism leading to the formation of bandgaps, we study the eigenmodes at strain $\varepsilon = 0.161$. Figure 5.7 shows the eigenmodes at low-range and high-range frequencies, namely, $f = 40$ Hz and $f = 250$ Hz. Note that at both these frequencies there is a negative transmission. The color on the eigenmodes shows the vertical displacement as per the color

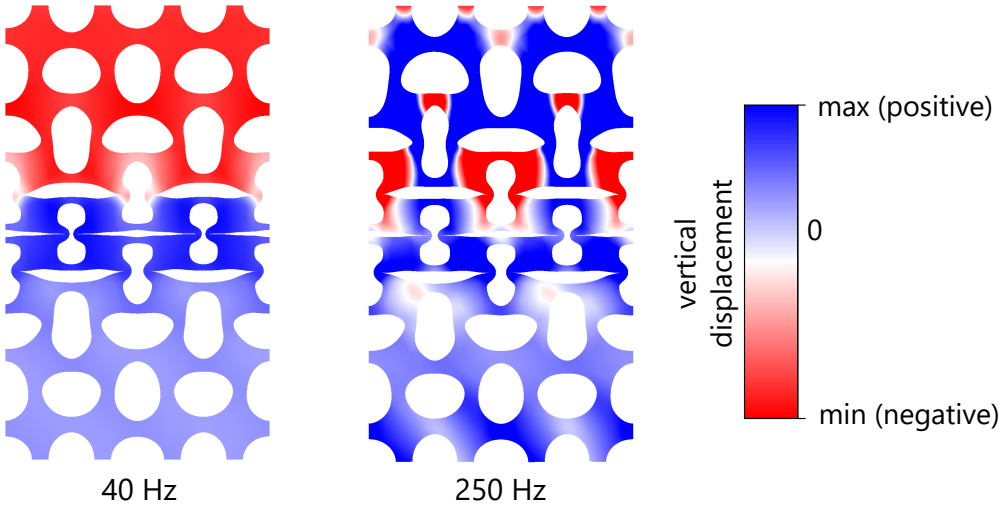

Figure 5.7: Eigenmodes at frequencies $f = 40$ Hz and $f = 250$ Hz at strain $\varepsilon = 0.161$. The color on the eigenmodes shows the vertical displacement as per the color bar on the right.

bar on the right.

From the color distribution in the eigenmode at $f = 40$ Hz, we can identify three distinct regions. First, the top region which is red in color. Second, the center region with collapsed voids with dark blue color. Third region is the bottom region colored in the light shade of blue corresponding to almost zero displacement. This shows that the first region act as a single rigid body and it moves down towards the applied perturbation at the top boundary. There is almost no deformation inside the region. The second region in the center moves up, opposite to the applied harmonic perturbation. We observe that the deformation in the eigenmode is highly localized in the beams connecting the two regions. The distribution of displacement field observed here highlights the presence of *local resonator*. Note that this resonator is formed because of the macro-structural changes due to the applied compression. The interaction of this local resonator with the elastic waves gives rise to the low-frequency bandgap.

At $f = 250$ Hz, we observe that the displacement field is locally distributed according the microstructure in the upper-half of the metamaterial. Therefore, the existence of bandgap at this frequency can be potentially because of *Bragg scattering* at higher values of frequency. In the lower-half, the displacement is close to zero (similar to 40 Hz eigenmode).

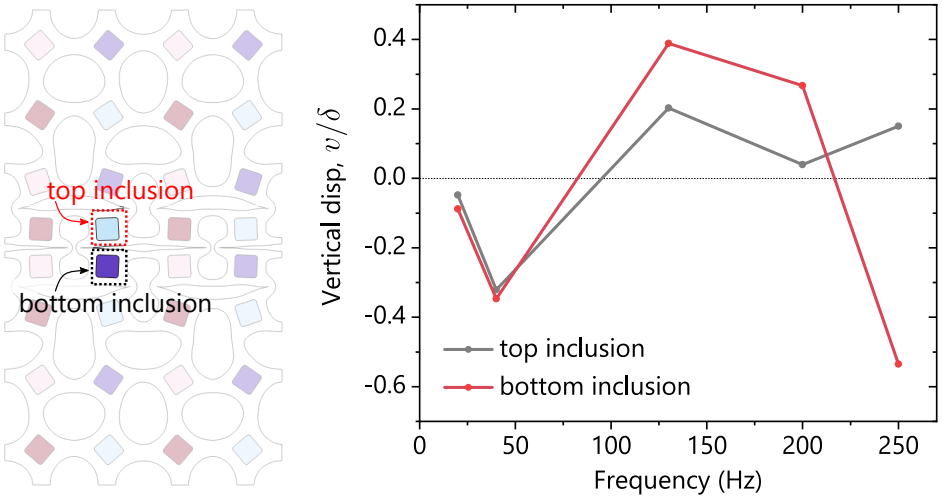

Figure 5.8: Vertical displacement of the two magnetic inclusions in the eigenmodes of various frequencies at strain $\varepsilon = 0.161$.

To further probe into the mechanism, in the eigenmodes at $\varepsilon = 0.161$, we analyze the vertical displacement of two magnetic inclusions in the collapsed region. The frequencies considered here lie in the bandgap regions. The two magnetic inclusions under consideration are shown in the Fig. 5.8. These inclusions have a collapsed void between them. The rationale behind this analysis is: If there is no relative displacement between the inclusions, then it shows the occurrence of resonance, where the whole collapsed region oscillates as a single body. However, if there is relative displacement, then that represents the open-close oscillation of the voids in the collapsed region. This correspond to the Bragg scattering phenomenon, also seen in periodic architecture with square distribution of voids.

We observe that at smaller frequency values, both the inclusions move towards the same direction with almost same amplitude, opposite to the applied harmonic perturbation. This confirms the local resonant behavior. However, at higher frequencies ($\geq$130 Hz), we find that the displacement of these inclusions differs. Interestingly, at $f = 250$ Hz, the inclusions move in opposite directions, highlighting the Bragg scattering phenomenon. In the intermediate range of frequency, we anticipate that the waves does not transmit potentially because of the combination of both the mechanisms.

6 CONCLUSION

6.1 Summary

This thesis has presented the fundamental study of the instability phenomenon occurring at different length scales in a variety of soft architected materials, including fiber and layered composites, matrix-voids material systems, and particulate composites. Moreover, it illustrates the potential of these materials to become the material-platform for novel applications.

First, in Chapter 2, we have investigated the microscopic and long-wave instabilities in a class of non-Gaussian hyperelastic fiber composites with Gent phases. We derived an analytical expression to predict the onset of the long-wave instabilities. By employing Bloch-Floquet analysis superimposed on finite deformations, we detect the critical parameters of elastic instabilities. Our results indicate that the critical strains and the associated wavelengths corresponding to the onset of instabilities are significantly affected by the locking parameters of the phases. We show that the stiffening effect (stemming from the accurate non-Gaussian based models) together with instability phenomenon lead to the widening of admissible pool of tunable microstructures.

Then, we have experimentally and numerically investigated the instability development and associated buckling patterns in 3D FCs with rectangular in-plane arrangement of fibers. We have provided a buckling configuration map in the design-space of geometric parameters (fiber volume fraction and in-plane periodicity aspect ratio). Pre-determined by the microstructure parameters, the fibers buckle towards (i) the first principal direction along which the fibers are closer to each other, or (ii) the second principal direction, or (iii) towards a non-principal direction. Furthermore, we find that the characteristics of the buckling plane map is governed by the shear modulus contrast between the phases of FCs.

In Chapter 3, we have investigated the buckling behavior of the composite system consisting of a magnetoactive layer embedded into an inactive elastomeric matrix. The composite is subjected to compressive strains in the presence of a high magnetic field. Our experimental results show that the critical buckling strain is highly tunable by the applied magnetic field. In particular, the composite buckles significantly earlier when the field is applied, leading to well-developed controllable wavy patterns in the post-buckling regime. To elucidate the mechanisms associated with the magneto-mechanical instability, we investigated the stability using numerical analysis. The numerical model is verified against the experimental results, showing its capability to predict the onset of the magneto-mechanical instability and the post-buckling behavior of the MRE. Collectively, the study demonstrates MRE instability tuning in a laminate form factor and outlines the strategy and benefits of harnessing two field physics for controlling bifurcations.

In Chapter 4, we presented a diverse range of instability-induced pattern transformations in a material system consisting of rigid magnetic inclusions periodically distributed in a soft matrix. Moreover, we proposed a strategy to effectively program the positioning of inclusions in the post-buckling state. By analyzing the influence of inclusions' magnetic strength on the instability development, we revealed the presence of three distinct regimes. First regime is characterized by weak magnetic interaction among the inclusions, resulting in the development of wavy buckling patterns, akin to mechanical composites. Interestingly, when the magnetic and mechanical interactions have a comparable command, the inclusions can rearrange into a periodic, quasi-periodic, or aperiodic pattern, depending on the initial spacing between them. Finally, in the magnetically-dominated regime, because of the nonlinear magnetic interaction between the inclusions, they rearrange into highly discrete binary (two-level) pattern. It not only allow us to program the deformation-activated microstructural transformation, but also embed

binary information into the material, as demonstrated through the example of Morse code.

Finally, in Chapter 5, we have proposed the design of a magneto-mechanical metamaterial with strain-tunable bandgaps. The strategy utilizes the structural transformations induced by the instability development and magnetic interactions. Through our simulation, we have shown the induction of new bandgaps via applied deformation. We also identify the underlying physical mechanism leading to the rise of bandgaps. In particular, we find that in the low-frequency range, the no-pass zone is created by the local resonance. On the other hand, at high frequency values, the wave propagation is inhibited by Bragg scattering.

6.2 Future outlook

The projects presented in this thesis offers insights into the non-linear response of soft architected materials, with a special emphasis on instability phenomenon. The results provide motivation and groundwork for the future theoretical and experimental investigations. Moreover, the various instability-induced microstructure transformations reported in this thesis offer promising strategies to design next generation materials. Some of the prospective research directions are discussed below.

Soft composites with strain-stiffening phases: The influence of strain-stiffening behavior is not only limited to instability development in soft composites. Such highly non-linear behavior of soft phases significantly also affect the composite's dynamic response, when subjected to finite deformations. For example, in another study (Arora et al., 2022), we have reported the observation of deformation-induced negative group velocity (NGV) state. These NGV states are achieved in stable composites through tailored stiffening behavior of their non-Gaussian soft phases. Similar roton-like dispersion behavior has been realized in other designs of metmaterials

(Chen et al., 2023b; Wang et al., 2022a; Iglesias Martínez et al., 2021). However, deformation-induced roton-like dispersion observed in our system are yet to be realized in experiments. In practice, the extent of matrix stiffening may be regulated through, for example, varying the level of crosslink density (Treloar, 1975). For instance, the crosslink density can be controlled by the light intensity during the polymerization process of a 3D printed soft polymer (Xiang et al., 2020c; Wu et al., 2018). Furthermore, designing matrix phase using the combination of polymer networks and stiff-inclusions can provide better control on its stiffening behavior (van Oosten et al., 2019; Shivers et al., 2020).

Tunable buckling plane orientation in fiber composites: The switch in the buckling plane direction reported in Chapter 2 are observed with the change in the geometry and/or the material properties of the 3D fiber composite. In other words, single buckling orientation is achieved in an individual specimen. To achieve multiple buckling orientations in a single specimen, the viscoelastic behavior of the phases can be utilized. In particular, by applying different strain-rates for compression, the effective shear modulus contrast between the phases can be actively controlled, resulting in different buckling directions. The role of viscoelastic response of soft phases in microstructural buckling had been studied for 2D soft composites (Slesarenko and Rudykh, 2016; Xiang et al., 2023). The results presented here can be further utilized in designing systems that exploits the targeted buckling plane; for instance, an acoustic metamaterial that can filter waves based on their polarization. Moreover, tunable fiber buckling orientation can induce soft shear response in different directions and can be used to design mechanically non-reciprocal materials (Wang et al., 2023).

Magnetic-field controlled buckling: The experimental and numerical results presented in Chapter 3 showed that the deformation-level, at which the instability occurs, changes with the magnitude of applied magnetic field. However, for the specimen considered in the study, we do not observe a

change in the buckling wavelength. Therefore, a more rigorous investigation is required to further understand the role of various magnetic field-induced stress-components within the composite that dictate the instability development. Furthermore, in order to expedite the detection of instability initiation, there arises a need for a computationally efficient technique, in contrast to the post-buckling analysis employed in the current investigation. For instance, the numerical implementation of the Bloch-Floquet analysis performed on this two-physics problem (Pathak et al., 2022) can be employed for the detection of instabilities.* Finally, it should be noted that the present study provides a proof-of-concept for the remotely-controlled instability behavior of a relatively simple composite design, i.e., a laminate. This strategy can be implemented to achieve transformations and tunable behaviors in even richer structural designs.

Magnetically-programmed instability patterns: The study in the Chapter 4 presents a novel strategy to program desired deformation fields within the soft architected material. In particular, the relative up/down shifting of neighboring inclusions is analogous to local rotational deformation fields. These local clockwise/anti-clockwise rotational fields are obtained because of the local interactions of the magnets. This approach can be readily implemented into the designs of other material-based systems. The strategy presented here opens the door to a broad range of applications in which the local shape-tunability of the architecture is instrumental. The pre-programmed shape morphing, for example, can be used to incorporate complex actuation, sensing, and control capabilities into the soft robots (Pal et al., 2021). Moreover, in soft particulate composites, the positioning of inclusions can be used to control the surface texture (Guttag and Boyce, 2015), thereby tuning their drag, friction, and wettability. Lastly, we envision the design of a re-programmable architected material in which the magnetic polarity of the inclusions can be reoriented through an external magnetic

*Work underway

field. From the fundamental viewpoint, the transition region, where a plethora of distinct buckling patterns are observed, opens a new avenue of research. In particular, further investigation is required to understand the interplay between the mechanical and magnetic interactions with the consideration of energy landscapes.* In addition, the non-linear and time-dependent response of soft matrix (e.g., the viscoelasticity) can further enrich the magneto-mechanical coupling and the admissible range of instability-induced pattern transformations.

Strain-tunable vibration absorber: The study reported in Chapter 5 pertains to small amplitude vibrations. In order to encompass a wide array of potential applications, it becomes necessary to analyze the material's response when subjected to vibrations of greater amplitudes. Moreover, an experimental investigation is required to validate the phenomena observed in the numerical simulations.* Furthermore, for an accurate representation of the experiments, the viscoelastic response of the soft matrix should be incorporated in the modelling, which is, however, not considered in the present study. Finally, it should be noted that the band-gap induced because of the local resonance within the architected material is inversely related to the lumped mass formed because of the void collapse. Hence, the material can be fabricated to actively switch from full to no transmission at a particular frequency range, catering to the requirements of a specific application.

*Work underway

REFERENCES

Aboudi, J., and R. Gilat. 2023. Bifurcation buckling and the effect of imperfections on the microbuckling of soft materials with periodic microstructure by the finite strain hfgmc micromechanics. *International Journal of Solids and Structures* 270:112227.

Aboudi, J., and K. Y. Volokh. 2020. Modeling deformation and failure of viscoelastic composites at finite strains. *Mechanics of Soft Materials* 2: 1–19.

Abu-Qbeitah, S., M. Jabareen, and K. Y. Volokh. 2022. Dynamic versus quasi-static analysis of crack propagation in soft materials. *Journal of Applied Mechanics* 89(12):121008.

Abu-Qbeitah, S., M. Jabareen, and K. Y. Volokh. 2023. Quasi-static crack propagation in soft materials using the material-sink theory. *International Journal of Mechanical Sciences* 248:108160.

Agoras, M., O. Lopez-Pamies, and P. Ponte Castañeda. 2009. Onset of macroscopic instabilities in fiber-reinforced elastomers at finite strain. *J. Mech. Phys. Solids* 57:1828–1850.

Aguzzi, G., C. Kanellopoulos, R. Wiltshaw, R. V. Craster, E. N. Chatzi, and A. Colombi. 2022. Octet lattice-based plate for elastic wave control. *Scientific reports* 12(1):1088.

Alam, Z., S. Padmanabhan, and A. K. Sharma. 2023. Magnetically tunable longitudinal wave band gaps in hard-magnetic soft laminates. *International Journal of Mechanical Sciences* 249:108262.

Alijani, A., O. Barrera, and S. P. Bordas. 2021. Circumferential crack modeling of thin cylindrical shells in modal deformation. *European Journal of Mechanics-A/Solids* 90:104360.

Amjadi, M., K.-U. Kyung, I. Park, and M. Sitti. 2016. Stretchable, skin-mountable, and wearable strain sensors and their potential applications: a review. *Advanced Functional Materials* 26(11):1678–1698.

Ansari, Q. M., M. Rouhi, G. Zucco, and P. M. Weaver. 2023. Effect of potting support design on compression buckling of composite cylindrical shells. *Engineering Structures* 285:116086.

Arora, N., A. Batan, J. Li, V. Slesarenko, and S. Rudykh. 2019. On the influence of inhomogeneous interphase layers on instabilities in hyperelastic composites. *Materials* 12(5):763.

Arora, N., Y. Xiang, and S. Rudykh. 2021. Multiscale analysis of elastic waves in soft materials: From molecular chain networks to fiber composites. *International Journal of Mechanical Sciences* 200:106433.

Arora, N., Q. Yao, and S. Rudykh. 2022. Deformation activated negative group velocity state in soft laminates. *Extreme Mechanics Letters* 51: 101592.

Babaee, S., N. Viard, P. Wang, N. X. Fang, and K. Bertoldi. 2016. Harnessing Deformation to Switch On and Off the Propagation of Sound. *Adv. Mater.* 28(8):1631–1635.

Bacquet, C. L., H. Al Ba'ba'a, M. J. Frazier, M. Nouh, and M. I. Hussein. 2018. Metadamping: dissipation emergence in elastic metamaterials. *Advances in applied mechanics* 51:115–164.

Bastola, A. K., and M. Hossain. 2020. A review on magneto-mechanical characterizations of magnetorheological elastomers. *Composites Part B: Engineering* 108348.

Bastola, A. K., and M. Hossain. 2021. The shape–morphing performance of magnetoactive soft materials. *Materials & Design* 211:110172.

Behl, M., and A. Lendlein. 2007. Actively moving polymers. *Soft Matter* 3(1):58–67.

Bertoldi, K., and M. C. Boyce. 2008a. Mechanically triggered transformations of phononic band gaps in periodic elastomeric structures. *Phys. Rev. B* 77(5):052105.

Bertoldi, K., and M. C. Boyce. 2008b. Wave propagation and instabilities in monolithic and periodically structured elastomeric materials undergoing large deformations. *Phys. Rev. B* 78:184107.

Bertoldi, K., M. C. Boyce, S. Deschanel, S. Prange, and T. Mullin. 2008. Mechanics of deformation-triggered pattern transformations and superelastic behavior in periodic elastomeric structures. *J. Mech. Phys. Solids* 56 (8):2642–2668.

Bertoldi, K., and M. Gei. 2011. Instabilities in multilayered soft dielectrics. *J. Mech. Phys. Solids* 59:18–42.

Bertoldi, K., P. M. Reis, S. Willshaw, and T. Mullin. 2010. Negative poisson's ratio behavior induced by an elastic instability. *Advanced materials* 22(3):361–366.

Bertoldi, K., V. Vitelli, J. Christensen, and M. Van Hecke. 2017. Flexible mechanical metamaterials. *Nature Reviews Materials* 2(11):1–11.

Bilal, O. R., A. Foehr, and C. Daraio. 2017a. Bistable metamaterial for switching and cascading elastic vibrations. *Proceedings of the National Academy of Sciences* 114(18):4603–4606.

Bilal, O. R., A. Foehr, and C. Daraio. 2017b. Reprogrammable phononic metasurfaces. *Advanced materials* 29(39):1700628.

Bobbert, F., S. Janbaz, and A. Zadpoor. 2018. Towards deployable metaimplants. *Journal of Materials Chemistry B* 6(21):3449–3455.

Braverman, L., C. Scheibner, B. VanSaders, and V. Vitelli. 2021. Topological defects in solids with odd elasticity. *Physical Review Letters* 127(26): 268001.

Brown, W. F. 1966. *Magnetoelastic interactions*, vol. 9. Springer.

Bruno, D., F. Greco, P. Lonetti, P. N. Blasi, and G. Sgambitterra. 2010. An investigation on microscopic and macroscopic stability phenomena of composite solids with periodic microstructure. *Int. J. Solids Struct.* 47(20): 2806–2824.

Budiansky, B. 1974. Theory of buckling and post-buckling behavior of elastic structures. *Advances in applied mechanics* 14:1–65.

Cao, X., S. Xuan, S. Sun, Z. Xu, J. Li, and X. Gong. 2021. 3d printing magnetic actuators for biomimetic applications. *ACS applied materials & interfaces* 13(25):30127–30136.

Castañeda, P. P., and E. Galipeau. 2011. Homogenization-based constitutive models for magnetorheological elastomers at finite strain. *Journal of the Mechanics and Physics of Solids* 59(2):194–215.

Chang, Z., H.-Y. Guo, B. Li, and X.-Q. Feng. 2015. Disentangling longitudinal and shear elastic waves by neo-hookean soft devices. *Applied Physics Letters* 106(16):161903.

Chen, L., X. L. Gong, and W. H. Li. 2007. Microstructures and viscoelastic properties of anisotropic magnetorheological elastomers. *Smart Mater. Struct.* 16:2645 – 2650.

Chen, L., R. Cheng, S. Li, H. Lian, C. Zheng, and S. P. Bordas. 2022. A sample-efficient deep learning method for multivariate uncertainty qualification of acoustic–vibration interaction problems. *Computer Methods in Applied Mechanics and Engineering* 393:114784.

Chen, L., Y. Zhang, H. Lian, E. Atroshchenko, C. Ding, and S. P. Bordas. 2020. Seamless integration of computer-aided geometric modeling and acoustic simulation: Isogeometric boundary element methods based on catmull-clark subdivision surfaces. *Advances in Engineering Software* 149: 102879.

Chen, T., O. R. Bilal, K. Shea, and C. Daraio. 2018. Harnessing bistability for directional propulsion of soft, untethered robots. *Proceedings of the National Academy of Sciences* 115(22):5698–5702.

Chen, Y., M. A. Abouelatta, K. Wang, M. Kadic, and M. Wegener. 2023a. Nonlocal cable-network metamaterials. *Advanced Materials* 35(15):2209988.

Chen, Y., X. Liu, and G. Hu. 2019. Topological phase transition in mechanical honeycomb lattice. *Journal of the Mechanics and Physics of Solids* 122:54–68.

Chen, Y., J. L. Schneider, M. F. Groß, K. Wang, S. Kalt, P. Scott, M. Kadic, and M. Wegener. 2023b. Observation of chirality-induced roton-like dispersion in a 3d micropolar elastic metamaterial. *Advanced Functional Materials* 2302699.

Cho, H., J. C. Weaver, E. Pöselt, P. J. in't Veld, M. C. Boyce, and G. C. Rutledge. 2016. Engineering the mechanics of heterogeneous soft crystals. *Advanced Functional Materials* 26(38):6938–6949.

Chortos, A., J. Liu, and Z. Bao. 2016. Pursuing prosthetic electronic skin. *Nature materials* 15(9):937–950.

Christensen, R. M. 1979. *Mechanics of composite materials*. New-York: Wiley Interscience.

Ciambella, J., and P. Nardinocchi. 2019. Magneto-induced remodelling of fibre-reinforced elastomers. *International Journal of Non-Linear Mechanics* 117:103230.

Ciambella, J., D. C. Stanier, and S. S. Rahatekar. 2017. Magnetic alignment of short carbon fibres in curing composites. *Composites Part B* 109:129–137.

Ciambella, J., A. Favata, and G. Tomassetti. 2018. A nonlinear theory for fibre-reinforced magneto-elastic rods. *Proceedings of the Royal Society A: Mathematical, Physical and Engineering Sciences* 474(2209):20170703.

Ciambella, J., and G. Tomassetti. 2020. A form-finding strategy for magneto-elastic actuators. *International Journal of Non-Linear Mechanics* 119:103297.

Cohen, T., and D. Durban. 2013. Plastic instabilities in porous cylinders under remote triaxial loading. *European Journal of Mechanics-A/Solids* 37:193–199.

Coleman, B. D., and W. Noll. 1974. The thermodynamics of elastic materials with heat conduction and viscosity. In *The foundations of mechanics and thermodynamics*, 145–156. Springer.

Colquitt, D., A. Colombi, R. Craster, P. Roux, and S. Guenneau. 2017. Seismic metasurfaces: Sub-wavelength resonators and rayleigh wave interaction. *Journal of the Mechanics and Physics of Solids* 99:379–393.

Danas, K., and N. Triantafyllidis. 2014. Instability of a magnetoelastic layer resting on a non-magnetic substrate. *J. Mech. Phys. Solids* 69:67–83.

De Maio, U., F. Greco, R. Luciano, G. Sgambitterra, and A. Pranno. 2023. Microstructural design for elastic wave attenuation in 3d printed nacre-like bioinspired metamaterials lightened with hollow platelets. *Mechanics Research Communications* 128:104045.

Dehghani, H., I. Noll, R. Penta, A. Menzel, and J. Merodio. 2020. The role of microscale solid matrix compressibility on the mechanical behaviour of poroelastic materials. *European Journal of Mechanics-A/Solids* 83:103996.

Ding, C., K. K. Tamma, X. Cui, Y. Ding, G. Li, and S. P. Bordas. 2020. An nth high order perturbation-based stochastic isogeometric method and implementation for quantifying geometric uncertainty in shell structures. *Advances in Engineering Software* 148:102866.

Ding, C., K. K. Tamma, H. Lian, Y. Ding, T. J. Dodwell, and S. Bordas. 2021. Uncertainty quantification of spatially uncorrelated loads with a reduced-order stochastic isogeometric method. *Computational Mechanics* 67(5):1255–1271.

Dong, Y., S. Wang, Y. Ke, L. Ding, X. Zeng, S. Magdassi, and Y. Long. 2020. 4d printed hydrogels: fabrication, materials, and applications. *Advanced Materials Technologies* 5(6):2000034.

Dorfmann, A., and R. W. Ogden. 2004. Nonlinear magnetoelastic deformations. *Q. J. Mech. Appl. Math.* 57:599–622.

Dorfmann, A., and R. W. Ogden. 2010. Electroelastic waves in a finitely deformed electroactive material. *IMA J. Appl. Math.* 75(4):604–636.

Dortdivanlioglu, B., and C. Linder. 2019. Diffusion-driven swelling-induced instabilities of hydrogels. *Journal of the Mechanics and Physics of Solids* 125:38–52.

D'Alessandro, L., A. O. Krushynska, R. Ardito, N. M. Pugno, and A. Corigliano. 2020. A design strategy to match the band gap of periodic and aperiodic metamaterials. *Scientific reports* 10(1):16403.

El Helou, C., P. R. Buskohl, C. E. Tabor, and R. L. Harne. 2021. Digital logic gates in soft, conductive mechanical metamaterials. *Nature communications* 12(1):1–8.

Elser, D., U. Andersen, A. Korn, O. Glöckl, S. Lorenz, C. Marquardt, and G. Leuchs. 2006. Reduction of guided acoustic wave brillouin scattering in photonic crystal fibers. *Physical review letters* 97(13):133901.

Emery, D., and Y. Fu. 2021. Post-bifurcation behaviour of elasto-capillary necking and bulging in soft tubes. *Proceedings of the Royal Society A* 477(2254):20210311.

Emuna, N., and N. Cohen. 2020. Circumferential instabilities in radially incompatible tubes. *Mechanics of Materials* 147:103458.

Erb, R. M., R. Libanori, N. Rothfuchs, and A. R. Studart. 2012. Composites reinforced in three dimensions by using low magnetic fields. *Science* 335(6065):199–204.

Erb, R. M., J. S. Sander, R. Grisch, and A. R. Studart. 2013. Self-shaping composites with programmable bioinspired microstructures. *Nature communications* 4(1):1–8.

Euler, L. 1759. Sur la force des colonnes. *Memoires de l'Academie des Sciences de Berlin* 252–282.

Euler, L. 1780a. De altitudine columnarum sub proprio pondere corruentium. *Acta Academiae Scientiarum Imperialis Petropolitanae* 163–193.

Euler, L. 1780b. Determinatio onerum, quae columnae gestare valent. *Acta Academiae Scientiarum Imperialis Petropolitanae* 121–145.

Fang, N., D. Xi, J. Xu, M. Ambati, W. Srituravanich, C. Sun, and X. Zhang. 2006. Ultrasonic metamaterials with negative modulus. *Nat. Mater.* 5(6): 452–456.

Farshad, M., and M. Le Roux. 2004. A new active noise abatement barrier system. *Polymer Testing* 23:855–860.

Florijn, B., C. Coulais, and M. van Hecke. 2016. Programmable mechanical metamaterials: the role of geometry. *Soft matter* 12(42):8736–8743.

Flory, P. J., and J. Rehner Jr. 1943. Statistical mechanics of cross-linked polymer networks i. rubberlike elasticity. *The journal of chemical physics* 11(11):512–520.

Foehr, A., O. R. Bilal, S. D. Huber, and C. Daraio. 2018. Spiral-based phononic plates: From wave beaming to topological insulators. *Physical review letters* 120(20):205501.

Fontenele, F. F., N. Andarawis-Puri, M. Agoras, and N. Bouklas. 2022. Fiber plasticity and loss of ellipticity in soft composites under non-monotonic loading. *International Journal of Solids and Structures* 249: 111628.

Frenzel, T., C. Findeisen, M. Kadic, P. Gumbsch, and M. Wegener. 2016. Tailored buckling microlattices as reusable light-weight shock absorbers. *Advanced Materials* 28(28):5865–5870.

Frenzel, T., M. Kadic, and M. Wegener. 2017. Three-dimensional mechanical metamaterials with a twist. *Science* 358(6366):1072–1074.

Frey, M., G. Biffi, M. Adobes-Vidal, M. Zirkelbach, Y. Wang, K. Tu, A. M. Hirt, K. Masania, I. Burgert, and T. Keplinger. 2019. Tunable wood by reversible interlocking and bioinspired mechanical gradients. *Advanced science* 6(10):1802190.

Fu, H., K. Nan, W. Bai, W. Huang, K. Bai, L. Lu, C. Zhou, Y. Liu, F. Liu, J. Wang, et al. 2018. Morphable 3d mesostructures and microelectronic devices by multistable buckling mechanics. *Nature materials* 17(3):268–276.

Fu, Y., L. Jin, and A. Goriely. 2021. Necking, beading, and bulging in soft elastic cylinders. *Journal of the Mechanics and Physics of Solids* 147: 104250.

Galich, P. I., and S. Rudykh. 2015. Comment on "Disentangling longitudinal and shear elastic waves by neo-Hookean soft devices" [Appl. Phys. Lett. 106, 161903 (2015)]. *Appl. Phys. Lett.* 107:056101.

Galich, P. I., and S. Rudykh. 2016. Manipulating pressure and shear elastic waves in dielectric elastomers via external electric stimuli. *Int. J. Solids Struct.* 91:18–25.

Galich, P. I., V. Slesarenko, J. Li, and S. Rudykh. 2018. Elastic instabilities and shear waves in hyperelastic composites with various periodic fiber arrangements. *International Journal of Engineering Science* 130:51–61.

Gao, C., V. Slesarenko, M. C. Boyce, S. Rudykh, and Y. Li. 2018. Instability-induced pattern transformation in soft metamaterial with hexagonal networks for tunable wave propagation. *Scientific Reports* 8(1):11834.

Gao, N., S. Qu, J. Li, J. Wang, and W. Chen. 2021. Harnessing post-buckling deformation to tune sound absorption in soft helmholtz absorbers. *International Journal of Mechanical Sciences* 208:106695.

Garcia-Gonzalez, D., and M. Hossain. 2020. A microstructural-based approach to model magneto-viscoelastic materials at finite strains. *International Journal of Solids and Structures* 208:119–132.

Gei, M., Z. Chen, F. Bosi, and L. Morini. 2020. Phononic canonical quasicrystalline waveguides. *Applied Physics Letters* 116(24).

Gent, A. N. 1996. A new constitutive relation for rubber. *Rubber Chem. Technol.* 69:59–61.

Geryak, R., and V. V. Tsukruk. 2014. Reconfigurable and actuating structures from soft materials. *Soft matter* 10(9):1246–1263.

Geymonat, G., S. Müller, and N. Triantafyllidis. 1993. Homogenization of nonlinearly elastic materials, microscopic bifurcation and macroscopic loss of rank-one convexity. *Arch. Rational. Mech. Anal.* 122:231–290.

Ginder, J. M., W. F. Schlotter, and M. E. Nichols. 2001. Magnetorheological elastomers in tunable vibration absorbers. *Proc. SPIE* 4331:103.

Ginder, J., S. Clark, W. Schlotter, and M. Nichols. 2002. Magnetostrictive phenomena in magnetorheological elastomers. *International Journal of Modern Physics B* 16(17n18):2412–2418.

Gong, X., Y. Fan, S. Xuan, Y. Xu, and C. Peng. 2012. Control of the damping properties of magnetorheological elastomers by using polycaprolactone as a temperature-controlling component. *Industrial & engineering chemistry research* 51(18):6395–6403.

Gorodkin, S., R. James, and W. Kordonski. 2009. Magnetic properties of carbonyl iron particles in magnetorheological fluids. In *Journal of physics: Conference series*, vol. 149, 012051. IOP Publishing.

Goshkoderia, A., and S. Rudykh. 2017. Stability of magnetoactive composites with periodic microstructures undergoing finite strains in the presence of a magnetic field. *Composites Part B* 128:19–29.

Goshkoderia, A., N. Arora, V. Slesarenko, J. Li, V. Chen, A. Juhl, P. Buskohl, and S. Rudykh. 2020a. Tunable permittivity in dielectric elastomer composites under finite strains: Periodicity, randomness, and instabilities. *International Journal of Mechanical Sciences* 186:105880.

Goshkoderia, A., V. Chen, J. Li, A. Juhl, P. Buskohl, and S. Rudykh. 2020b. Instability-induced pattern formations in soft magnetoactive composites. *Physical Review Letters* 124(15):158002.

Greco, F., L. Leonetti, P. Lonetti, R. Luciano, and A. Pranno. 2020. A multiscale analysis of instability-induced failure mechanisms in fiber-reinforced

composite structures via alternative modeling approaches. *Composite Structures* 112529.

Greco, F., and R. Luciano. 2011. A theoretical and numerical stability analysis for composite micro-structures by using homogenization theory. *Composites Part B: Engineering* 42(3):382–401.

Guttag, M., and M. C. Boyce. 2015. Locally and dynamically controllable surface topography through the use of particle-enhanced soft composites. *Advanced Functional Materials* 25(24):3641–3647.

Hauseux, P., J. S. Hale, and S. P. Bordas. 2017. Accelerating monte carlo estimation with derivatives of high-level finite element models. *Computer Methods in Applied Mechanics and Engineering* 318:917–936.

Hauseux, P., J. S. Hale, S. Cotin, and S. P. Bordas. 2018. Quantifying the uncertainty in a hyperelastic soft tissue model with stochastic parameters. *Applied Mathematical Modelling* 62:86–102.

He, Z., H. Zhang, R. Xiao, and S. Qu. 2023. Mechanical behaviors of soft elastomers filled with low melting alloys. *Acta Mechanica Solida Sinica* 36(2):221–229.

Ho, T. Y. K., A. Nirmal, M. R. Kulkarni, D. Accoto, and N. Mathews. 2022. Soft actuator materials for electrically driven haptic interfaces. *Advanced Intelligent Systems* 4(2):2100061.

Hu, W., G. Z. Lum, M. Mastrangeli, and M. Sitti. 2018. Small-scale soft-bodied robot with multimodal locomotion. *Nature* 554(7690):81–85.

Hu, X., H. Zhu, S. Chen, H. Yu, and S. Qu. 2022. Magnetomechanical behavior of soft magnetoactive membranes. *International Journal of Solids and Structures* 234:111310.

Huang, C., Z. Wang, D. Quinn, S. Suresh, and K. J. Hsia. 2018. Differential growth and shape formation in plant organs. *Proceedings of the National Academy of Sciences* 115(49):12359–12364.

Humphrey, J. D. 2002. *Cardiovascular solid mechanics: cells, tissues, and organs*. New York: Springer-Verlag.

Hussein, M. I. 2019. *Advances in crystals and elastic metamaterials, part 2*. Academic Press.

Iglesias Martínez, J. A., M. F. Groß, Y. Chen, T. Frenzel, V. Laude, M. Kadic, and M. Wegener. 2021. Experimental observation of roton-like dispersion relations in metamaterials. *Science advances* 7(49):eabm2189.

Iooss, G., and D. D. Joseph. 2012. *Elementary stability and bifurcation theory*. Springer Science & Business Media.

Itskov, M., and V. N. Khiêm. 2016. A polyconvex anisotropic free energy function for electro-and magneto-rheological elastomers. *Math. Mech. Solids* 21:1126–1137.

Ivaneyko, D., V. Toshchevikov, M. Saphiannikova, and G. Heinrich. 2014. Mechanical properties of magneto-sensitive elastomers: unification of the continuum-mechanics and microscopic theoretical approaches. *Soft Matter* 10(13):2213–2225.

Jansari, C., J. Videla, S. Natarajan, S. P. Bordas, and E. Atroshchenko. 2022. Adaptive enriched geometry independent field approximation for 2d time-harmonic acoustics. *Computers & Structures* 263:106728.

Javili, A., G. Chatzigeorgiou, and P. Steinmann. 2013. Computational homogenization in magneto-mechanics. *Int. J. Solids Struct.* 50(25-26): 4197–4216.

Jiang, C., S. Singamaneni, E. Merrick, and V. V. Tsukruk. 2006. Complex buckling instability patterns of nanomembranes with encapsulated gold nanoparticle arrays. *Nano letters* 6(10):2254–2259.

Jiang, Y., L. M. Korpas, and J. R. Raney. 2019. Bifurcation-based embodied logic and autonomous actuation. *Nature communications* 10(1):1–10.

Kadapa, C., and M. Hossain. 2022. A unified numerical approach for soft to hard magneto-viscoelastically coupled polymers. *Mechanics of Materials* 166:104207.

Kamperman, M., and A. Synytska. 2012. Switchable adhesion by chemical functionality and topography. *Journal of Materials Chemistry* 22(37): 19390–19401.

Kang, S. H., S. Shan, A. Košmrlj, W. L. Noorduin, S. Shian, J. C. Weaver, D. R. Clarke, and K. Bertoldi. 2014. Complex ordered patterns in mechanical instability induced geometrically frustrated triangular cellular structures. *Physical review letters* 112(9):098701.

Kankanala, S. V., and N. Triantafyllidis. 2008. Magnetoelastic buckling of a rectangular block in plane strain. *J. Mech. Phys. Solids* 56:1147–1169.

Karami Mohammadi, N., P. I. Galich, A. O. Krushynska, and S. Rudykh. 2019. Soft magnetoactive laminates: large deformations, transverse elastic waves and band gaps tunability by a magnetic field. *Journal of Applied Mechanics* 86(11).

Kareklas, K., D. Nettle, and T. V. Smulders. 2013. Water-induced finger wrinkles improve handling of wet objects. *Biology letters* 9(2):20120999.

Keip, M.-A., and M. Rambausek. 2017. Computational and analytical investigations of shape effects in the experimental characterization of magnetorheological elastomers. *International Journal of Solids and Structures* 121:1–20.

Khanouki, M. A., R. Sedaghati, and M. Hemmatian. 2019. Experimental characterization and microscale modeling of isotropic and anisotropic magnetorheological elastomers. *Composites Part B: Engineering* 176:107311.

Kim, Y., H. Yuk, R. Zhao, S. A. Chester, and X. Zhao. 2018. Printing ferromagnetic domains for untethered fast-transforming soft materials. *Nature* 558:274–279.

Kim, Y., and X. Zhao. 2022. Magnetic soft materials and robots. *Chemical reviews* 122(5):5317–5364.

Kirchhoff, G. 1859. Ueber das gleichgewicht und die bewegung eines unendlich dünnen elastischen stabes.

Kochmann, D. M., and K. Bertoldi. 2017. Exploiting microstructural instabilities in solids and structures: from metamaterials to structural transitions. *Applied mechanics reviews* 69(5):050801.

Kovetz, A. 2000. *Electromagnetic theory*, vol. 975. Oxford University Press Oxford.

Krishnan, D., and H. Johnson. 2009. Optical properties of two-dimensional polymer photonic crystals after deformation-induced pattern transformations. *J. Mech. Phys. Solids* 57(9):1500–1513.

Krushynska, A. O., A. S. Gliozzi, A. Fina, D. Krushinsky, D. Battegazzore, M. A. Badillo-Ávila, M. Acuautla, S. Stassi, C. Noè, N. M. Pugno, et al. 2021a. Dissipative dynamics of polymer phononic materials. *Advanced Functional Materials* 31(30):2103424.

Krushynska, A. O., N. Anerao, M. B. Ävila, M. Stokroos, and M. Acuautla. 2021b. Arbitrary-curved waveguiding and broadband attenuation in additively manufactured lattice phononic media. *Materials & design* 205: 109714.

Kuang, X., J. Wu, K. Chen, Z. Zhao, Z. Ding, F. Hu, D. Fang, and H. J. Qi. 2019. Grayscale digital light processing 3d printing for highly functionally graded materials. *Sci. adv.* 5(5):5790.

Kuang, X., S. Wu, Q. Ze, L. Yue, Y. Jin, S. M. Montgomery, F. Yang, H. J. Qi, and R. Zhao. 2021. Magnetic dynamic polymers for modular assembling and reconfigurable morphing architectures. *Advanced materials* 33(30):2102113.

Kushwaha, M., P. Halevi, L. Dobrzynski, and B. Djafari-Rouhani. 1993. Acoustic band structure of periodic elastic composites. *Phys. Rev. Lett.* 71(13):2022–2025.

Lagrange, J.-L. 1770. Sur la figure des colonnes. *Miscellanea Taurinensia* 5:123–166.

Lanotte, L., G. Ausanio, C. Hison, V. Iannotti, and C. Luponio. 2003. The potentiality of composite elastic magnets as novel materials for sensors and actuators. *Sensors and Actuators A: Physical* 106(1-3):56–60.

Lantean, S., G. Barrera, C. F. Pirri, P. Tiberto, M. Sangermano, I. Roppolo, and G. Rizza. 2019. 3d printing of magnetoresponsive polymeric materials with tunable mechanical and magnetic properties by digital light processing. *Advanced Materials Technologies* 4(11):1900505.

Lee, S. H., C. M. Park, Y. M. Seo, Z. G. Wang, and C. K. Kim. 2010. Composite Acoustic Medium with Simultaneously Negative Density and Modulus. *Phys. Rev. Lett.* 104(5):054301.

Leipholz, H. 2013. *Stability theory: an introduction to the stability of dynamic systems and rigid bodies*. Springer-Verlag.

Li, C., H. Yang, Z. Suo, and J. Tang. 2020. Fatigue-resistant elastomers. *Journal of the Mechanics and Physics of Solids* 134:103751.

Li, J., V. Slesarenko, P. I. Galich, and S. Rudykh. 2018a. Instabilities and pattern formations in 3d-printed deformable fiber composites. *Composites Part B: Engineering* 148:114–122.

Li, J., V. Slesarenko, and S. Rudykh. 2018b. Auxetic multiphase soft composite material design through instabilities with application for acoustic metamaterials. *Soft Matter* 14(30):6171–6180.

Li, J., N. Arora, and S. Rudykh. 2021. Elastic instabilities, microstructure transformations, and pattern formations in soft materials. *Current Opinion in Solid State and Materials Science* 25(2):100898.

Li, J., N. Gao, R. Bao, and W. Chen. 2023a. Tunable static and dynamic responses of soft porous phononic crystals. In *Mechanics of high-contrast elastic solids: Contributions from euromech colloquium 626*, 133–154. Springer.

Li, J., T. D. Pallicity, V. Slesarenko, A. Goshkoderia, and S. Rudykh. 2019a. Domain formations and pattern transitions via instabilities in soft heterogeneous materials. *Advanced Materials* 31(14):1807309.

Li, J., V. Slesarenko, and S. Rudykh. 2022. Emergence of instability-driven domains in soft stratified materials. *npj Computational Materials* 8(1):1–6.

Li, J., H. Varner, and T. Cohen. 2023b. Periodic necking of misfit hyperelastic filaments embedded in a soft matrix. *Journal of the Mechanics and Physics of Solids* 172:105171.

Li, J., Y. Wang, W. Chen, Y.-S. Wang, and R. Bao. 2019b. Harnessing inclusions to tune post-buckling deformation and bandgaps of soft porous periodic structures. *Journal of Sound and Vibration* 459:114848.

Li, R., and L. Sun. 2014. Dynamic viscoelastic modeling of magnetorheological elastomers. *Acta Mechanica* 225:1347–1359.

Li, Y., N. Kaynia, S. Rudykh, and M. C. Boyce. 2013. Wrinkling of interfacial layers in stratified composites. *Adv. Eng. Mater.* 15(10):921–926.

Lin, S., T. Cohen, T. Zhang, H. Yuk, R. Abeyaratne, and X. Zhao. 2016. Fringe instability in constrained soft elastic layers. *Soft matter* 12(43): 8899–8906.

Liu, H., Q. Zhang, K. Zhang, G. Hu, and H. Duan. 2019. Designing 3d digital metamaterial for elastic waves: from elastic wave polarizer to vibration control. *Advanced Science* 6(16):1900401.

Liu, L., P. Kamm, F. García-Moreno, J. Banhart, and D. Pasini. 2017. Elastic and failure response of imperfect three-dimensional metallic lattices: the role of geometric defects induced by selective laser melting. *Journal of the Mechanics and Physics of Solids* 107:160–184.

Liu, Z., X. Zhang, Y. Mao, Y. Zhu, Z. Yang, C. T. Chan, and P. Sheng. 2000. Locally resonant sonic materials. *science* 289(5485):1734–1736.

Lopez-Donaire, M. L., G. de Aranda-Izuzquiza, S. Garzon-Hernandez, J. Crespo-Miguel, M. Fernandez-de la Torre, D. Velasco, and D. Garcia-Gonzalez. 2023. Computationally guided diw technology to enable robust printing of inks with evolving rheological properties. *Advanced Materials Technologies* 8(3):2201707.

Lott, M., P. Roux, M. Rupin, D. Colquitt, and A. Colombi. 2021. Negative index metamaterial through multi-wave interactions: numerical proof of the concept of low-frequency lamb-wave multiplexing. *Scientific Reports* 11(1):561.

Love, A. 1893. Ha treatise on the mathematical theory of. *Elasticity* 2:327.

Lu, L., P. Guo, and Y. Pan. 2017. Magnetic-field-assisted projection stereolithography for three-dimensional printing of smart structures. *Journal of Manufacturing Science and Engineering* 139(7).

Lucarini, S., M. Hossain, and D. Garcia-Gonzalez. 2022. Recent advances in hard-magnetic soft composites: Synthesis, characterisation, computational modelling, and applications. *Composite Structures* 279:114800.

Makarova, L. A., Y. A. Alekhina, T. S. Rusakova, and N. S. Perov. 2016. Tunable properties of magnetoactive elastomers for biomedical applications. *Physics procedia* 82:38–45.

Matlack, K. H., M. Serra-Garcia, A. Palermo, S. D. Huber, and C. Daraio. 2018. Designing perturbative metamaterials from discrete models. *Nature materials* 17(4):323–328.

Mazzotti, M., A. Foehr, O. R. Bilal, A. Bergamini, F. Bosia, C. Daraio, N. M. Pugno, and M. Miniaci. 2023. Bio-inspired non self-similar hierarchical elastic metamaterials. *International Journal of Mechanical Sciences* 241: 107915.

Memoli, G., M. Caleap, M. Asakawa, D. R. Sahoo, B. W. Drinkwater, and S. Subramanian. 2017. Metamaterial bricks and quantization of meta-surfaces. *Nature communications* 8(1):14608.

Meng, L., X. Yang, E. Salcedo, D.-C. Baek, J. E. Ryu, Z. Lu, and J. Zhang. 2020. A combined modeling and experimental study of tensile properties of additively manufactured polymeric composite materials. *Journal of Materials Engineering and Performance* 29:2597–2604.

Merodio, J., and R. W. Ogden. 2002. Material instabilities in fiber-reinforced nonlinearly elastic solids under plane deformation. *Archives of Mechanics (IPPT)* 54:525–552.

Merodio, J., and T. J. Pence. 2001. Kink surfaces in a directionally reinforced neo-hookean material under plane deformation: I. mechanical equilibrium. *J. of Elasticity* V62(2):119–144.

Michel, J.-C., O. Lopez-Pamies, P. P. Castañeda, and N. Triantafyllidis. 2010. Microscopic and macroscopic instabilities in finitely strained fiber-reinforced elastomers. *Journal of the Mechanics and Physics of Solids* 58(11):1776–1803.

Miniaci, M., and R. Pal. 2021. Design of topological elastic waveguides. *Journal of Applied Physics* 130(14).

Montgomery, S. M., S. Wu, X. Kuang, C. D. Armstrong, C. Zemelka, Q. Ze, R. Zhang, R. Zhao, and H. J. Qi. 2021. Magneto-mechanical metamaterials with widely tunable mechanical properties and acoustic bandgaps. *Advanced Functional Materials* 31(3):2005319.

Moon, F., and Y.-H. Pao. 1968. Magnetoelastic buckling of a thin plate.

Moreno-Mateos, M. A., K. Danas, and D. Garcia-Gonzalez. 2023a. Influence of magnetic boundary conditions on the quantitative modelling of magnetorheological elastomers. *Mechanics of Materials* 104742.

Moreno-Mateos, M. A., M. Hossain, P. Steinmann, and D. Garcia-Gonzalez. 2022a. Hybrid magnetorheological elastomers enable versatile soft actuators. *npj Computational Materials* 8(1):162.

Moreno-Mateos, M. A., M. Hossain, P. Steinmann, and D. Garcia-Gonzalez. 2023b. Hard magnetics in ultra-soft magnetorheological elastomers enhance fracture toughness and delay crack propagation. *Journal of the Mechanics and Physics of Solids* 173:105232.

Moreno-Mateos, M. A., M. L. Lopez-Donaire, M. Hossain, and D. Garcia-Gonzalez. 2022b. Effects of soft and hard magnetic particles on the mechanical performance of ultra-soft magnetorheological elastomers. *Smart Materials and Structures* 31(6):065018.

Morillas, J. R., and J. de Vicente. 2020. Magnetorheology: a review. *Soft Matter* 16(42):9614–9642.

Mullin, T., S. Deschanel, K. Bertoldi, and M. C. Boyce. 2007. Pattern transformation triggered by deformation. *Phys. Rev. Lett.* 99 (8):84301.

Nam, T. H., I. Petríková, and B. Marvalová. 2020. Experimental characterization and viscoelastic modeling of isotropic and anisotropic magnetorheological elastomers. *Polymer Testing* 81:106272.

Narayanan, P., R. Pramanik, and A. Arockiarajan. 2023. Micromechanics-based constitutive modeling of hard-magnetic soft materials. *Mechanics of Materials* 104722.

Nestorovic, M. D., and N. Triantafyllidis. 2004. Onset of failure in finitely strained layered composites subjected to combined normal and shear loading. *J. Mech. Phys. Solids* 52:941–974.

Nguyen, Q. S. 2000. *Stability and nonlinear solid mechanics*. Wiley.

Nguyen, Y. T., T. J. Pence, and I. S. Wichman. 2019. Crack formation during solid pyrolysis: evolution, pattern formation and statistical behaviour. *Proceedings of the Royal Society A* 475(2229):20190211.

Ogden, R. W. 1997. *Non-linear elastic deformations*. New York: Dover Publications.

O'Neill, M. R., D. Sessions, N. Arora, V. W. Chen, A. Juhl, G. H. Huff, S. Rudykh, R. F. Shepherd, and P. R. Buskohl. 2022. Dielectric elastomer architectures with strain-tunable permittivity. *Advanced Materials Technologies* 7(11):2200296.

Ongaro, F., E. Barbieri, and N. Pugno. 2016a. The in-plane elastic properties of hierarchical composite cellular materials: synergy of hierarchy, material heterogeneity and cell topologies at different levels. *Mechanics of Materials* 103:135–147.

Ongaro, F., P. De Falco, E. Barbieri, and N. Pugno. 2016b. Mechanics of filled cellular materials. *Mechanics of Materials* 97:26–47.

van Oosten, A. S., X. Chen, L. Chin, K. Cruz, A. E. Patteson, K. Pogoda, V. B. Shenoy, and P. A. Janmey. 2019. Emergence of tissue-like mechanics from fibrous networks confined by close-packed cells. *Nature* 573(7772): 96–101.

Ortigosa, R., and A. J. Gil. 2016. A new framework for large strain electromechanics based on convex multi-variable strain energies: Conservation laws and hyperbolicity and extension to electro-magnetomechanics. *Computer Methods in Applied Mechanics and Engineering*.

Ostoja-Starzewski, M., S. Kale, P. Karimi, A. Malyarenko, B. Raghavan, S. I. Ranganathan, and J. Zhang. 2016. Scaling to rve in random media. *Advances in Applied Mechanics* 49:111–211.

Otténio, M., M. Destrade, and R. Ogden. 2008. Incremental magnetoelastic deformations, with application to surface instability. *J. Elasticity* 90:19–42.

Pal, A., V. Restrepo, D. Goswami, and R. V. Martinez. 2021. Exploiting mechanical instabilities in soft robotics: Control, sensing, and actuation. *Advanced Materials* 33(19):2006939.

Pal, A., and M. Sitti. 2023. Programmable mechanical devices through magnetically tunable bistable elements. *Proceedings of the National Academy of Sciences* 120(15):e2212489120.

Palagi, S., A. G. Mark, S. Y. Reigh, K. Melde, T. Qiu, H. Zeng, C. Parmeggiani, D. Martella, A. Sanchez-Castillo, N. Kapernaum, et al. 2016. Structured light enables biomimetic swimming and versatile locomotion of photoresponsive soft microrobots. *Nature materials* 15(6):647–653.

Pathak, P., N. Arora, and S. Rudykh. 2022. Magnetoelastic instabilities in soft laminates with ferromagnetic hyperelastic phases. *International Journal of Mechanical Sciences* 213:106862.

Pence, T. J., and J. Song. 1991. Buckling instabilities in a thick elastic three-ply composite plate under thrust. *International journal of solids and structures* 27(14):1809–1828.

Peri, V., Z.-D. Song, M. Serra-Garcia, P. Engeler, R. Queiroz, X. Huang, W. Deng, Z. Liu, B. A. Bernevig, and S. D. Huber. 2020. Experimental characterization of fragile topology in an acoustic metamaterial. *Science* 367(6479):797–800.

Pranno, A., F. Greco, L. Leonetti, P. Lonetti, R. Luciano, and U. De Maio. 2022. Band gap tuning through microscopic instabilities of compressively loaded lightened nacre-like composite metamaterials. *Composite Structures* 282:115032.

Psarra, E., L. Bodelot, and K. Danas. 2017. Two-field surface pattern control via marginally stable magnetorheological elastomers. *Soft Matter* 13(37):6576–6584.

Psarra, E., L. Bodelot, and K. Danas. 2019. Wrinkling to crinkling transitions and curvature localization in a magnetoelastic film bonded to a non-magnetic substrate. *Journal of the Mechanics and Physics of Solids* 133:103734.

Qiu, G., and T. Pence. 1997. Loss of ellipticity in plane deformation of a simple directionally reinforced incompressible nonlinearly elastic solid. *J. of Elasticity* 49:31–63.

Reddy, N. H., and P. Saxena. 2018. Instabilities in the axisymmetric magnetoelastic deformation of a cylindrical membrane. *International Journal of Solids and Structures* 136:203–219.

Rosen, B. W. 1965. Mechanics of composite strengthening. In *Fibre composite materials*, 37–75. Ohio: Am. Soc. Metals.

Rudykh, S., and K. Bertoldi. 2013. Stability of anisotropic magnetorheological elastomers in finite deformations: a micromechanical approach. *J. Mech. Phys. Solids* 61:949–967.

Rudykh, S., K. Bhattacharya, and G. deBotton. 2014. Multiscale instabilities in soft heterogeneous dielectric elastomers. *Proc. R. Soc. A* 470: 20130618.

Rudykh, S., and M. Boyce. 2014. Transforming wave propagation in layered media via instability-induced interfacial wrinkling. *Phys. Rev. Lett.* 112: 034301.

Rudykh, S., and G. deBotton. 2011. Stability of anisotropic electroactive polymers with application to layered media. *Z. Angew. Math. Phys.* 62: 1131–1142.

Rudykh, S., and G. deBotton. 2012. Instabilities of hyperelastic fiber composites: micromechanical versus numerical analyses. *J. Elasticity* 106: 123–147.

Russ, J., V. Slesarenko, S. Rudykh, and H. Waisman. 2020. Rupture of 3d-printed hyperelastic composites: Experiments and phase field fracture modeling. *Journal of the Mechanics and Physics of Solids* 140:103941.

Saheb, D. N., and J. P. Jog. 1999. Natural fiber polymer composites: A review. *Adv. Polym. Technol.* 18(4):351–363.

Saxena, P., M. Hossain, and P. Steinmann. 2013. A theory of finite deformation magneto-viscoelasticity. *International Journal of Solids and Structures* 50(24):3886–3897.

Saxena, P., N. H. Reddy, and S. P. Pradhan. 2019. Magnetoelastic deformation of a circular membrane: wrinkling and limit point instabilities. *International Journal of Non-Linear Mechanics* 116:250–261.

Schwartz, J., and A. Boydston. 2019. Multimaterial actinic spatial control 3d and 4d printing. *Nat. Commun.* 10(1):1–10.

Shan, S., S. H. Kang, P. Wang, C. Qu, S. Shian, E. R. Chen, and K. Bertoldi. 2014. Harnessing multiple folding mechanisms in soft periodic structures for tunable control of elastic waves. *Adv. Funct. Mater.* 24:4935–4942.

Shen, R., H. Waisman, and L. Guo. 2019. Fracture of viscoelastic solids modeled with a modified phase field method. *Computer Methods in Applied Mechanics and Engineering* 346:862–890.

Shepherd, R. F., F. Ilievski, W. Choi, S. A. Morin, A. A. Stokes, A. D. Mazzeo, X. Chen, M. Wang, and G. M. Whitesides. 2011. Multigait soft robot. *Proceedings of the national academy of sciences* 108(51):20400–20403.

Shim, J., S. Shan, A. Košmrlj, S. H. Kang, E. R. Chen, J. C. Weaver, and K. Bertoldi. 2013. Harnessing instabilities for design of soft reconfigurable auxetic/chiral materials. *Soft Matter* 9(34):8198–8202.

Shivers, J. L., J. Feng, A. S. van Oosten, H. Levine, P. A. Janmey, and F. C. MacKintosh. 2020. Compression stiffening of fibrous networks with stiff inclusions. *Proceedings of the National Academy of Sciences* 117(35): 21037–21044.

Sim, J., S. Wu, J. Dai, and R. R. Zhao. 2023. Magneto-mechanical bilayer metamaterial with global area-preserving density tunability for acoustic wave regulation. *Advanced Materials* 2303541.

Slesarenko, V., P. I. Galich, J. Li, N. X. Fang, and S. Rudykh. 2018. Foreshadowing elastic instabilities by negative group velocity in soft composites. *Applied Physics Letters* 113(3):031901.

Slesarenko, V., N. Kazarinov, and S. Rudykh. 2017a. Distinct failure modes in bio-inspired 3d-printed staggered composites under non-aligned loadings. *Smart Mater. Struct.* 26(3):035053.

Slesarenko, V., and S. Rudykh. 2016. Harnessing viscoelasticity and instabilities for tuning wavy patterns in soft layered composites. *Soft Matter* 12:3677–3682.

Slesarenko, V., and S. Rudykh. 2017. Microscopic and macroscopic instabilities in hyperelastic fiber composites. *J. Mech. Phys. Solids* 99:471–482.

Slesarenko, V., and S. Rudykh. 2018. Towards mechanical characterization of soft digital materials for multimaterial 3d-printing. *Int. J. Eng. Science* 123:62–72.

Slesarenko, V., K. Volokh, J. Aboudi, and S. Rudykh. 2017b. Understanding the strength of bioinspired soft composites. *Int. J. Mech. Sci.* 131:171–178.

Southwell, R. V. 1914. V. on the general theory of elastic stability. *Philosophical Transactions of the Royal Society of London. Series A, Containing Papers of a Mathematical or Physical Character* 213(497-508):187–244.

Stanier, D. C., J. Ciambella, and S. S. Rahatekar. 2016. Fabrication and characterisation of short fibre reinforced elastomer composites for bending and twisting magnetic actuation. *Composites Part A* 91:168–176.

Sundaram, S., M. Skouras, D. S. Kim, L. van den Heuvel, and W. Matusik. 2019. Topology optimization and 3d printing of multimaterial magnetic actuators and displays. *Science advances* 5(7):eaaw1160.

Tang, S.-Y., X. Zhang, S. Sun, D. Yuan, Q. Zhao, S. Yan, L. Deng, G. Yun, J. Zhang, S. Zhang, et al. 2018. Versatile microfluidic platforms enabled by novel magnetorheological elastomer microactuators. *Advanced Functional Materials* 28(8):1705484.

Thompson, J. M. T., and G. W. Hunt. 1973. A general theory of elastic stability. *(No Title)*.

Tian, T. F., W. H. Li, and Y. M. Deng. 2011. Sensing capabilities of graphite based mr elastomers. *Smart Mater. Struct.* 20:025022.

Tiersten, H. 1964. Coupled magnetomechanical equations for magnetically saturated insulators. *J. Math. Phys.* 5(9):1298–1318.

Timoshenko, S. P., and J. M. Gere. 2009. *Theory of elastic stability*. Courier Corporation.

Treloar, L. R. G. 1975. *The physics of rubber elasticity*. Clarendon Press, Oxford.

Treloar, L. 1943. The elasticity of a network of long-chain molecules. i. *Transactions of the Faraday Society* 39:36–41.

Triantafyllidis, N., and B. N. Maker. 1985. On the comparison between microscopic and macroscopic instability mechanisms in a class of fiber-reinforced composites. *J. Appl. Mech., Trans. ASME* 52:794–800.

Triantafyllidis, N., M. D. Nestorovic, and M. W. Schraad. 2006. Failure surfaces for finitely strained two-phase periodic solids under general in-plane loading. *J. Appl. Mech., Trans. ASME* 73(3):505–515.

Turco, E., E. Barchiesi, A. Ciallella, and F. dell'Isola. 2022. Nonlinear waves in pantographic beams induced by transverse impulses. *Wave Motion* 115:103064.

Volokh, K. 2017. Loss of ellipticity in elasticity with energy limiters. *European Journal of Mechanics-A/Solids* 63:36–42.

Walter, B. L., J.-P. Pelteret, J. Kaschta, D. W. Schubert, and P. Steinmann. 2017. Preparation of magnetorheological elastomers and their slip-free characterization by means of parallel-plate rotational rheometry. *Smart Materials and Structures* 26(8):085004.

Wang, K., Y. Chen, M. Kadic, C. Wang, and M. Wegener. 2022a. Nonlocal interaction engineering of 2d roton-like dispersion relations in acoustic and mechanical metamaterials. *Communications Materials* 3(1):35.

Wang, M. C., and E. Guth. 1952. Statistical theory of networks of non-gaussian flexible chains. *The Journal of Chemical Physics* 20(7):1144–1157.

Wang, P., F. Casadei, S. Shan, J. C. Weaver, and K. Bertoldi. 2014. Harnessing Buckling to Design Tunable Locally Resonant Acoustic Metamaterials. *Phys. Rev. Lett.* 113(1):014301.

Wang, P., L. Lu, and K. Bertoldi. 2015. Topological phononic crystals with one-way elastic edge waves. *Physical review letters* 115(10):104302.

Wang, Q., X. Dong, L. Li, and J. Ou. 2018. Mechanical modeling for magnetorheological elastomer isolators based on constitutive equations and electromagnetic analysis. *Smart Materials and Structures* 27(6):065017.

Wang, X., Z. Li, S. Wang, K. Sano, Z. Sun, Z. Shao, A. Takeishi, S. Matsubara, D. Okumura, N. Sakai, et al. 2023. Mechanical nonreciprocity in a uniform composite material. *Science* 380(6641):192–198.

Wang, Y.-F., Y.-Z. Wang, B. Wu, W. Chen, and Y.-S. Wang. 2020. Tunable and active phononic crystals and metamaterials. *Applied Mechanics Reviews* 72(4):040801.

Wang, Y., J. Li, Y. Fu, R. Bao, W. Chen, and Y.-S. Wang. 2021. Tunable guided waves in a soft phononic crystal with a line defect. *APL Materials* 9(5).

Wang, Z., C. Xiang, X. Yao, P. Le Floch, J. Mendez, and Z. Suo. 2019. Stretchable materials of high toughness and low hysteresis. *Proceedings of the National Academy of Sciences* 116(13):5967–5972.

Wang, Z., Y. Wu, D. Wu, D. Sun, and L. Lin. 2022b. Soft magnetic composites for highly deformable actuators by four-dimensional electrohydrodynamic printing. *Composites Part B: Engineering* 231:109596.

Wang, Z., Q. Zhang, K. Zhang, and G. Hu. 2016. Tunable digital metamaterial for broadband vibration isolation at low frequency. *Advanced materials* 28(44):9857–9861.

Wang, Z., L. Jing, K. Yao, Y. Yang, B. Zheng, C. M. Soukoulis, H. Chen, and Y. Liu. 2017. Origami-based reconfigurable metamaterials for tunable chirality. *Advanced materials* 29(27):1700412.

Wilder-Smith, E. P. 2004. Water immersion wrinkling: physiology and use as an indicator of sympathetic function. *Clinical Autonomic Research* 14: 125–131.

Wootton, P., J. Kaplunov, and D. Colquitt. 2019. An asymptotic hyperbolic–elliptic model for flexural-seismic metasurfaces. *Proceedings of the Royal Society A* 475(2227):20190079.

Wu, J., Z. Zhao, C. M. Hamel, X. Mu, X. Kuang, Z. Guo, and H. J. Qi. 2018. Evolution of material properties during free radical photopolymerization. *Journal of the Mechanics and Physics of Solids* 112:25–49.

Wu, S., J. Eichenberger, J. Dai, Y. Chang, N. Ghalichechian, and R. R. Zhao. 2022. Magnetically actuated reconfigurable metamaterials as conformal electromagnetic filters. *Advanced Intelligent Systems* 4(9):2200106.

Wu, S., C. M. Hamel, Q. Ze, F. Yang, H. J. Qi, and R. Zhao. 2020. Evolutionary algorithm-guided voxel-encoding printing of functional hard-magnetic soft active materials. *Advanced Intelligent Systems* 2(8):2000060.

Xia, G., Y. Su, and W. Chen. 2021. Instability of compressible soft electroactive plates. *International Journal of Engineering Science* 162: 103474.

Xia, X., C. M. Spadaccini, and J. R. Greer. 2022. Responsive materials architected in space and time. *Nature Reviews Materials* 7(9):683–701.

Xiang, C., Z. Wang, C. Yang, X. Yao, Y. Wang, and Z. Suo. 2020a. Stretchable and fatigue-resistant materials. *Materials Today* 34:7–16.

Xiang, Y., D. Chen, N. Arora, Q. Yao, and S. Rudykh. 2023. Towards understanding the role of viscoelasticity in microstructural buckling in soft particulate composites. *Composites Part B: Engineering* 110850.

Xiang, Y., C. Schilling, N. Arora, A. Boydston, and S. Rudykh. 2020b. Mechanical characterization and constitutive modeling of visco-hyperelasticity of photocured polymers. *Additive Manufacturing* 101511.

Xiang, Y., C. Schilling, N. Arora, A. Boydston, and S. Rudykh. 2020c. Mechanical characterization and constitutive modeling of visco-hyperelasticity of photocured polymers. *Additive Manufacturing* 101511.

Xiang, Y., D. Zhong, S. Rudykh, H. Zhou, S. Qu, and W. Yang. 2020d. A review of physically based and thermodynamically based constitutive models for soft materials. *Journal of Applied Mechanics* 87(11).

Yang, J., X. Gong, H. Deng, L. Qin, and S. Xuan. 2012. Investigation on the mechanism of damping behavior of magnetorheological elastomers. *Smart materials and structures* 21(12):125015.

Yarali, E., M. Baniasadi, A. Zolfagharian, M. Chavoshi, F. Arefi, M. Hossain, A. Bastola, M. Ansari, A. Foyouzat, A. Dabbagh, et al. 2022. Magneto-/electro-responsive polymers toward manufacturing, characterization, and biomedical/soft robotic applications. *Applied Materials Today* 26:101306.

Yasuda, H., P. R. Buskohl, A. Gillman, T. D. Murphey, S. Stepney, R. A. Vaia, and J. R. Raney. 2021. Mechanical computing. *Nature* 598(7879): 39–48.

Yim, S., and M. Sitti. 2011. Design and rolling locomotion of a magnetically actuated soft capsule endoscope. *IEEE Transactions on Robotics* 28(1): 183–194.

Yu, K., N. X. Fang, G. Huang, and Q. Wang. Magnetoactive acoustic metamaterials. *Advanced Materials* 30(21):1706348.

Yu, P., S. P. A. Bordas, and P. Kerfriden. 2022. Adaptive isogeometric analysis for transient dynamics: Space–time refinement based on hierarchical a-posteriori error estimations. *Computer Methods in Applied Mechanics and Engineering* 394:114774.

Ze, Q., S. Wu, J. Dai, S. Leanza, G. Ikeda, P. C. Yang, G. Iaccarino, and R. R. Zhao. 2022. Spinning-enabled wireless amphibious origami millirobot. *Nature communications* 13(1):3118.

Zeng, W., L. Shu, Q. Li, S. Chen, F. Wang, and X.-M. Tao. 2014. Fiber-based wearable electronics: a review of materials, fabrication, devices, and applications. *Advanced materials* 26(31):5310–5336.

Zhang, G., T. Yin, G. Nian, and Z. Suo. 2021a. Fatigue-resistant polyurethane elastomer composites. *Extreme Mechanics Letters* 101434.

Zhang, M., H. Shahsavan, Y. Guo, A. Pena-Francesch, Y. Zhang, and M. Sitti. 2021b. Liquid-crystal-elastomer-actuated reconfigurable microscale kirigami metastructures. *Advanced Materials* 33(25):2008605.

Zhang, Q., Y. Chen, K. Zhang, and G. Hu. 2020. Dirac degeneracy and elastic topological valley modes induced by local resonant states. *Physical Review B* 101(1):014101.

Zhang, Q., A. V. Cherkasov, N. Arora, G. Hu, and S. Rudykh. 2023. Magnetic field-induced asymmetric mechanical metamaterials. *Extreme Mechanics Letters* 59:101957.

Zhang, Q., D. Guo, and G. Hu. 2021c. Tailored mechanical metamaterials with programmable quasi-zero-stiffness features for full-band vibration isolation. *Advanced Functional Materials* 31(33):2101428.

Zhang, Q., and S. Rudykh. 2022. Magneto-deformation and transverse elastic waves in hard-magnetic soft laminates. *Mechanics of Materials* 169: 104325.

Zhang, Q., K. Zhang, and G. Hu. 2018. Tunable fluid-solid metamaterials for manipulation of elastic wave propagation in broad frequency range. *Applied Physics Letters* 112(22).

Zhang, S., C. Xia, and N. Fang. 2011. Broadband acoustic cloak for ultrasound waves. *Phys. Rev. Lett.* 106(2):024301.

Zhang, Y., Q. Wang, S. Yi, Z. Lin, C. Wang, Z. Chen, and L. Jiang. 2021d. 4d printing of magnetoactive soft materials for on-demand magnetic actuation transformation. *ACS Applied Materials & Interfaces* 13(3): 4174–4184.

Zhang, Y., M. Velay-Lizancos, D. Restrepo, N. D. Mankame, and P. D. Zavattieri. 2021e. Architected material analogs for shape memory alloys. *Matter* 4(6):1990–2012.

Zhou, L.-Y., J. Fu, and Y. He. 2020. A review of 3d printing technologies for soft polymer materials. *Adv. Funct. Mater.* 30(28):2000187.

Zhu, J., M. Dexheimer, and H. Cheng. 2017. Reconfigurable systems for multifunctional electronics. *npj Flexible Electronics* 1(1):1–13.

Zhu, R., X. Liu, G. Hu, C. Sun, and G. Huang. 2014. Negative refraction of elastic waves at the deep-subwavelength scale in a single-phase metamaterial. *Nature communications* 5(1):5510.

Ziegler, H. 2013. *Principles of structural stability*, vol. 35. Birkhäuser.